

THE UNIVERSITY OF HULL

**THE APPLICATION OF THE SOFT IMPRESSION
TECHNIQUE TO EVALUATE FLOW STRESS, CREEP
AND FRICTIONAL DEFORMATION OF
POLYCRYSTALLINE DIAMOND AND CUBIC BORON
NITRIDE**

being a thesis submitted for the degree of

DOCTOR OF PHILOSOPHY

in the University of Hull

by

Ali Al-Watban, MSc (Warwick University, U.K.)

September, 1996

**PAGE
NUMBERS
CUT OFF**

Summary

Metal shaping processes are clear examples of engineering applications where a hard material is worn by a softer one - i.e. the tool and workpiece respectively. The soft impressor technique, introduced by Brookes and Green (1973), has proved valuable in measuring the relevant mechanical properties of tool materials - e.g. the measurement of the flow stress of diamond single crystals at temperatures up to 1500°C (Brookes, 1992). In this work, the technique has been extended further in order to form a basis for the comparison and evaluation of ultra-hard materials. Three main aspects of the performance of these tool materials have been covered: the effect of temperature on flow stress; cumulative deformation under point loading conditions; wear due to repeated traversals (fatigue).

In the first part, the technique has been extended to determine the flow stress of polycrystalline diamond and cubic boron nitride as a function of temperature and a mathematical model has been proposed to estimate the flow stress in isotropic polycrystalline materials. This model was first analysed by Love (1928) and was used as the basis on which to identify the threshold pressure above which dislocation movement is initiated in diamond single crystals (Brookes *et al* (1990)). The applicability of this model for polycrystals was verified by correlating the yield strength of polycrystalline copper, measured in tension, with the determination of minimum contact mean pressure to plastically deform the same material. According to the model, the first evidence of plastic deformation should be observed at the contact periphery and this has been verified in this work. Consequently, using this approach, the effect of temperature on the flow stress of polycrystalline diamond (Syndax) and polycrystalline cubic boron nitride (Amorite) has been established and it is shown that there are three distinct regimes. In regime I, the deformation is brittle and fracture occurs above a given mean pressure; in regime II dislocations are mobile and the flow stress decreases sharply as the temperature rises; and in regime III the flow stress is independent of the temperature.

In the earlier work, the brittle - ductile transition temperature (BDT) has been identified as that temperature where regime I ends and II begins. Above the

BDT, time dependent plastic flow has been observed, in all of these materials, leading to a measurable increase in the size of the impression. However, this particular type of cumulative deformation, described as impression creep, is shown to be different to conventional creep as measured under uniaxial stress conditions.

Finally, the room temperature friction and deformation of various polycrystalline diamond based specimens, i.e. aggregates with a binder phase of cobalt (Syndite) or silicon carbide (Syndax), a polycrystalline coating produced by a chemical vapour deposition processes (CVDite) and cubic boron nitride (Amorite) were studied when softer metallic and ceramic sliders were used. As a result of increasing the number of traversals, significant wear of the CVDite diamond coating by softer metallic sliders (aluminium and mild steel) was observed. This could be attributed to the high level of residual stresses in the diamond layer which is thought to be due to the difference in the thermal expansion coefficients of the coatings and their substrates. Burton *et al* (1995) reported a strain of 0.3% on the surface of the diamond coating and hence the tensile stress on the upper side of the coating will be equivalent to about 3.0 GPa. This value is comparable to the theoretical cleavage strength of diamond. It is suggested an additional tensile stress, due to the sliding friction, could have caused cleavage of individual diamond crystals. The resultant wear debris then becoming embedded in the metallic slider. These embedded diamond particles in the tip of the slider could be responsible for the increased friction and wear.

Acknowledgements

I am indebted to my supervisor Professor Chris Brookes for the advice, encouragement and support he has given me throughout the course of this work.

I am also grateful to Dr. Jill Brookes, Dr. Robert Wallis and Dr Clive Waddington for their advice and support in the preparation of this thesis.

I would like to thank all my colleagues in the EDM department, with special thanks to Mr Garry Robinson for his contribution in the photography and Mr Les Houghton for his assistance with equipment.

Finally I would like to express my deepest gratitude to all members of my family especially my father Soleman Al-Watban, my wife Lateefah Al-Romeeh and my children Suliaman Al-Watban, Abrar Al-Watban and Mohammed Al-Watban, for their suffering, unending patience and unique support over the past years.

TABLE OF CONTENTS

Chapter 1 Review of Ultra-hard Materials and their Properties

1.1	Introduction	1
	Ultra hard materials	1
1.2	Cubic boron nitride (cBN)	3
	1.2.1 Introduction	3
	1.2.2 Crystal structures of boron nitride	3
	1.2.3 Manufacturing cubic boron nitride	6
	Single crystal synthesis	6
	Polycrystalline cBN production	7
	1.2.4 The structure and properties the polycrystalline cBN (Amorite)	8
	1.2.5 Industrial applications of cBN	11
1.3	Diamond	13
	1.3.1 Introduction	13
	1.3.2 Crystal structure and physical properties of diamond	14
	1.3.3 Polycrystalline Diamond	16
	1.3.4 Polycrystalline diamond synthesis	16
	Syndite	18
	Syndax	19
	1.3.5 The microstructure of Syndite and Syndax	20
	1.3.6 Industrial applications of diamond	22
	1.3.7 Thermal stability of PCD	24
1.4	Diamond coating	25
	1.4.1 Introduction	25
	1.4.2 Deposition and characterisation of diamond coating	26
	1.4.3 Physical properties of CVD diamond	29
	1.4.4 The applications of CVD diamond	30
1.5	Measurement of specific mechanical properties of ultra-hard materials	32

1.5.1 Fracture of ultra-hard materials	32
Cleavage	32
Hertzian fracture	32
1.5.2 Plasticity of ultra-hard materials	34
Plastic flow	34
Indentation hardness of ultra-hard materials	35
1.5.3 Friction and wear of diamond	38
Friction of diamond on diamond in air	38
Friction of diamond in a vacuum	39
The mechanism of friction	39
Wear	40
1.5.4 Some relevant mechanical properties of PCD and cBN	42

Chapter 2 Apparatus and Experimental Procedures

2.1 The high temperature apparatus	44
2.2 Calibrating and recording the frictional force	45
2.3 Temperature measurement	46
2.4 Preparation of specimen, impressors and sliders	46
Specimens	46
Impressors	47
2.5 Sliding friction and wear experiments at room temperature	48
2.6 Measurement of the volume of impressions	50

Chapter 3 The effect of Temperature on the Flow Stress of Ultra-hard Materials

3.1 Introduction	53
Indentation plasticity	54
Single crystals	57
3.2 Soft impression technique	59
3.2.1 Modelling of the soft impression technique	62
The Roberts model for $\{111\}\langle 110\rangle$ slip systems	63

3.3 Determining the CRSS of MgO and diamond	64
3.4 The application of the soft impression technique to measure the minimum contact mean pressure to plastically deform polycrystalline materials	68
3.4.1 Evaluation of the minimum contact mean pressure to plastically deform polycrystalline copper	69
3.4.2 Modelling of the maximum shear stress(S_{max})	72
On the surface when $Z=0$	75
On the axis when $\rho=0$	77
3.4.3 Evaluation of minimum contact mean pressure to deform ultra-hard materials (Syndax and Amborite)	81
Experimental procedure and results	81
Syndax	82
Cubic boron nitride (Amborite)	83
3.5 Discussion	84
3.6. Conclusions	89

Chapter 4 Impression Creep

4.1 Introduction	91
4.2 Review of indentation creep	95
4.3 Creep deformation in ceramics and hard materials	100
Single phase materials	104
Class I composites	104
Class II composites	104
Class III composites	105
4.4 High temperature impression creep tests of Syndax and Amborite	105
4.4.1 Experimental procedure	105
4.4.2 Experimental results	107
Cubic boron nitride (Amborite)	107
Syndite	108
Activation energies	109
4.4.3 Discussion	110
4.4.4 Summary and conclusions	113

Chapter 5 The Friction and Wear due to Softer Sliders on CBN, PCD and Diamond

5.1 Introduction	115
5.2 Friction and wear of polycrystalline ultra-hard materials	116
5.3 Experimental procedure	120
Effective and apparent mean pressure	121
5.4 Results	123
5.4.1 Friction of softer sliders - single traversal	123
Single crystal and CVDite	123
Polycrystalline diamond and CVDite	124
Cubic boron nitride (cBN)	125
5.4.2 Friction and wear of PCD due to multiple traversals	126
Friction and wear of CVDite	126
Syndax	128
Syndite	129
5.5 Discussion	132
5.6 Conclusion	140

Chapter 6 Summary, Conclusions and Suggestions for Further Research

6.1 Summary	143
6.1.1 Flow stress	143
6.1.2 Impression creep	144
6.1.3 Frictional deformation	145
6.2 Suggestion for further research	146

References

Chapter 1 Review of ultra-hard materials and their properties

1.1 Introduction

A new generation of cutting tools, based on ultra-hard materials, has been developed over the past two decades and the market share is currently dominated by cutting tools manufactured from either diamond or from boron nitride. Compacted diamond or boron nitride grit, consolidated at elevated temperatures and pressures, forms a high density, high strength, hard tool insert. However, an evaluation of the mechanical properties of ultra-hard materials has always presented a challenge to scientists. Frequently, measurements of hardness have provided the basis for the assessment of several other mechanical and physical properties, particularly where samples with limited size or restricted geometry are available. The main objective of this project was to assess the suitability of the 'new' method of deformation of hard materials by softer point contact to measure the flow stress; creep; friction and wear properties of these ultra-hard polycrystalline materials (i.e. principally those properties of importance in metal cutting application).

◆ Ultra hard materials

Ultra-hard polycrystalline materials are manufactured by subjecting randomly oriented, and carefully graded single crystal particles of diamond or cubic boron nitride to high temperature and pressure in the presence of metallic or ceramic

materials. Under these conditions the composite mass of particles develops into a continuous, dense, polycrystalline structure with a binder phase. The secondary growth between particles, which takes place during the sintering process, depends on the binder material - the highest secondary growth takes place in a diamond based composite (Syndite) where a metallic binder of cobalt is used. Although the single crystal forms of diamond and cubic boron nitride are the hardest materials known i.e. 108 and 45 GPa respectively, their application for single point metal cutting is hindered by their brittle behaviour and small size. However, both materials are widely used as grits for grinding operations.

The manufactured polycrystalline form is so effective that, if a single crystal particle fractures, the fracture path is stopped by the boundary between particles. This enhances the toughness of the material.

The term *ultra-hard* polycrystalline materials is given to polycrystalline diamond and polycrystalline cubic boron nitride due to their extreme hardness value by comparison with the hardness values of other hard materials. Currently, ultra-hard polycrystalline materials are produced by De Beers (South Africa and Ireland), General Electric (USA), Sumitomo (Japan) and some factories in the former USSR countries. In this work all the materials were supplied by De Beers and the company trade names of the products such as Amborite (cubic boron nitride) Syndax, Syndite (polycrystalline diamond) and CVDite (diamond coated silicon carbide) are used throughout the thesis.

This chapter contains a review of the structure, method of production and microstructure, and the general mechanical properties of those materials.

1.2 Cubic boron nitride (cBN)

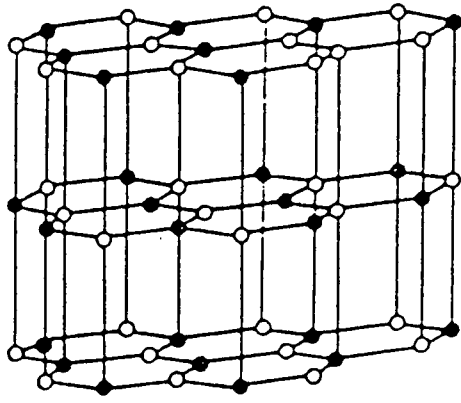
1.2.1 Introduction

Cubic boron nitride is one of the hardest materials known to man. It is second only to diamond in hardness. Diamond exists naturally but cubic boron nitride is a synthetic material. Both cubic boron nitride (cBN) and diamond are widely used for metal shaping processes - e.g. cutting and grinding. However, cubic boron nitride has a particular advantage over diamond in that it is more stable thermally and chemically and hence suitable for machining ferrous materials.

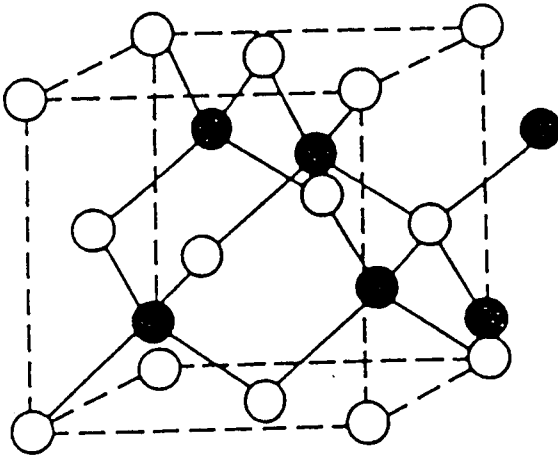
Single crystals of cubic boron nitride are of very small size and therefore their use is limited to grinding operations. However, micron-size particles, subjected to high pressure and high temperature in the presence of a binding material, form a compact polycrystalline material. This material is hard and tough, with a high thermal conductivity and shock resistance and is suitable for application at high temperature - e.g. as high speed cutting tools.

1.2.2 Crystal structures of boron nitride

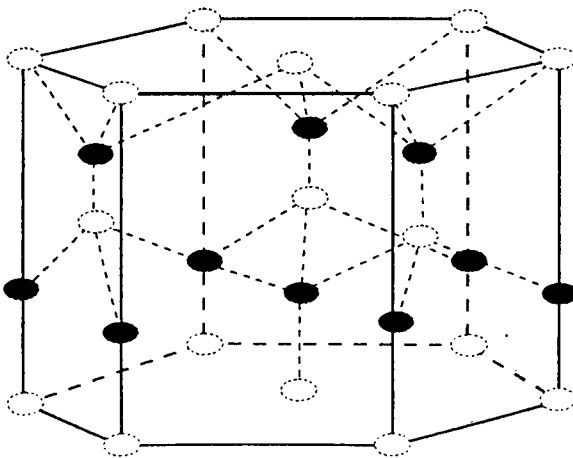
Boron and nitrogen are the two elements which form boron nitride compounds of which a number of polymorphs exist. Hexagonal boron nitride (hBN) has the same structure as graphite, with boron and nitrogen atoms arranged alternately, as shown in Figure 1.1a. The chemical bonds between boron and nitrogen within the layer are strong and covalent (sp^2). On the other hand, the chemical bonds



(a)



(b)



(c)

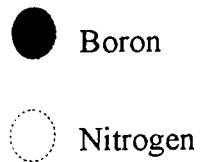


Figure 1.1: (a) The hexagonal graphitic form of boron nitride (hBN)
 (b) The cubic form of boron nitride - Zincblende (cBN)
 (c) The hexagonal form of boron nitride - Wurtzite (wBN)

between the atoms in adjacent layers are weak (van der Waals type). The stacking arrangement of the atoms results in a slippery, friable compound which is very useful as a lubricating agent.

There are two common forms of boron nitride which can be derived from the hexagonal form. The first form of boron nitride is cubic, obtained by breaking and changing the nature of the chemical bonds of the hexagonal form - Figure 1.1b. The crystal structure of cubic boron nitride (cBN) is of the zinc-blende type with 1.57\AA atomic distance (B-N) and 3.45 gm/cm^3 density (Table 1.1). In this diamond-like cubic structure, the bonds between boron and nitrogen are predominantly covalent, being tetrahedrally co-ordinated, (sp^3), but some ionic bonding is known to be present. The boron nitride cubic crystal structure is often described as two interpenetrating face-centred cubic sub-lattices, one consisting entirely of boron atoms and the other consisting of nitrogen atoms. This arrangement results in (111) planes consisting entirely of boron atoms with nitrogen atoms on adjacent (111) planes. The slip systems of cubic boron nitride are $\{111\} \langle 110 \rangle$ and the weak bonding (cleavage plane) is along the six $\{011\}$ planes (DeVries, 1972). It is materials based on this polymorph which are included in this work.

The second common form of boron nitride is wurtzite. Wurtzite boron nitride (wBN) is obtained when the interplanar spacing of hBN is reduced by compression at high pressure and deformation of the hexagons leads to a hybridisation change from sp^2 to sp^3 . Each (001) planar layer of the lattice splits into two planes, one layer containing boron atoms and the other nitrogen atoms Figure 1.1 (c).

In addition to the two common polymorphs, there are some other less common forms, such as turbostratic BN (tBN), rhombohedral BN (rBN) (Laurence *et al* 1991). The last two structures of boron nitride (BN) show hexagonal ring layers of the boron and nitrogen system, similar to that in (hBN) but with a different stacking arrangement between the layers.

Table 1.1 Physical properties of cBN and diamond

Property	Cubic boron nitride	Diamond
Crystal structure	Zincblende	Diamond cubic
Lattice constant	3.615 Å	3.57 Å
Ion distance (Å)	1.57	1.54
Density (gm/cm ³)	3.45	3.515
Index of refraction	2.117 Å	2.147 Å
Melting point (K)	3500	4000
Poisson's ratio	0.1	0.07
Young's modulus (GPa)	730	1141
Bulk modulus (GPa)	290	442
Shear modulus (GPa)	332	553
Slip system	{111} <1 $\bar{1}$ 0>	{111} <1 $\bar{1}$ 0>
Cleavage plane	{011}	{111}
Knoop hardness (GPa)	30-45	56-108

1.2.3 Manufacturing cubic boron nitride

◆ Single crystal synthesis

The similarity between graphite and the hexagonal form of boron nitride encouraged earlier scientists to try to produce the cubic form of boron nitride in an attempt to produce a 'harder than diamond' material. In 1957 Wentorf declared that the hard cubic form could be prepared from mixtures containing boron and nitrogen. In his process, cubic boron nitride was formed in a metal capsule heated by resistance heaters while subjected to high pressure. A detailed account of the design of similar apparatus is given by Hall (1961). The pressure and temperature employed to achieve that transformation were 8.6 GPa and 1800°C respectively and the particular pressure and temperature necessary depended upon the catalyst. The catalysts used were alkali metals, alkaline-earth metals and antimony, tin and lead (Wentorf 1961). The cubic boron nitride formed with these metallic catalysts tended to be black in colour. However, the use of magnesium, calcium or lithium nitrides resulted in the production of white clear crystals. Normally, the higher the atomic weight of the catalyst, the higher the pressure is needed to carry out the transformation (Wentorf 1961) and the effectiveness of any catalyst is greatly reduced by the presence of water or boric oxide. The conversion of hexagonal boron nitride to cubic boron nitride is the main method used in industrial production.

The direct conversion of pure hexagonal boron nitride to cubic boron nitride was reported by Bundy and Wentorf (1963) using a specific belt apparatus designed

to reach a pressure of 18 GPa. However, the size of the resulting crystallites of both forms was quite small (1 μm and less).

After a few years (Wakatsuki *et al*, 1972) reported a direct transformation process at a much lower pressure (\cong 6GPa) than that used previously by Bundy and Wentorf (1963). These workers proved that the transformation condition can be lowered by careful selection of the starting material (hBN) and optimum results were obtained with pure hBN with a small particle size.

In addition to conversion with the aid of a catalyst and the direct conversion method, there are other methods which can be used, such as crystal growth under a static high pressure. This method involves the transport of BN, with the help of a solvent, from a hot zone containing hBN, to a cold region where one or more cBN seeds have been placed. However, the time required for the crystal growth is much longer than that used for the synthesis described previously and it is reported that days may elapse before the completion of the process. (Laurence *et al*, 1991).

A dynamic high pressure process was reported by Sawaoka and Akashi (1984). This method involves multiple-shock compression of the boron nitride powder to be transformed into cBN.

◆ Polycrystalline cBN production

The synthesis of a tough, coherent, high strength and chemically stable cBN compact was first reported by Wentorf and co-workers (1966). The fundamental reason for undertaking the production and development of PCBN compact tools

was to obtain a cutting tool with superior strength, abrasion resistance and chemical stability (Hibbs Jr. and Wentorf (1974)).

The production of cBN crystals is the first stage in the process of producing dense compact polycrystalline cubic boron nitride (PCBN) cutting tools. The second stage is to mix the cBN crystals with a binding material, press the mixture together and subject it to a high pressure and temperature comparable to those at which they were originally synthesised - that is a temperature between 1500° and 2000°C and a pressure between 5 and 8 GPa. The binding materials were chosen from the group consisting of tungsten, nickel, beryllium, rhenium, titanium, zirconium, aluminium, chromium, cobalt, molybdenum, manganese and copper (Agarwala *et al* 1986).

1.2.4 The structure and properties of the polycrystalline cBN (Amorite)

The sintering process of cBN compact materials occurs at very high temperatures, and ultra high pressure is necessary in order to maintain the stability of the cBN. The sintering process is resisted by the limited plasticity of cBN, which prevents the achievement of the applied pressure over whole grain surfaces (Pullum and Lewis, 1990). In the early stages of the sintering process, substantial plastic deformation of the cBN particles occurs at the areas of direct contact during the high pressure synthesis process. The pressure is a maximum on the grains with direct contact but is below the average pressure on the surfaces of the grains at some distance away from the contact areas. Those surfaces at low pressure are thermodynamically unstable and the high

temperature of sintering causes reconversion of cBN→hBN (Walmsley and Lang, 1987). However, this transformation is inhibited by infiltration of the binding material between the grains.

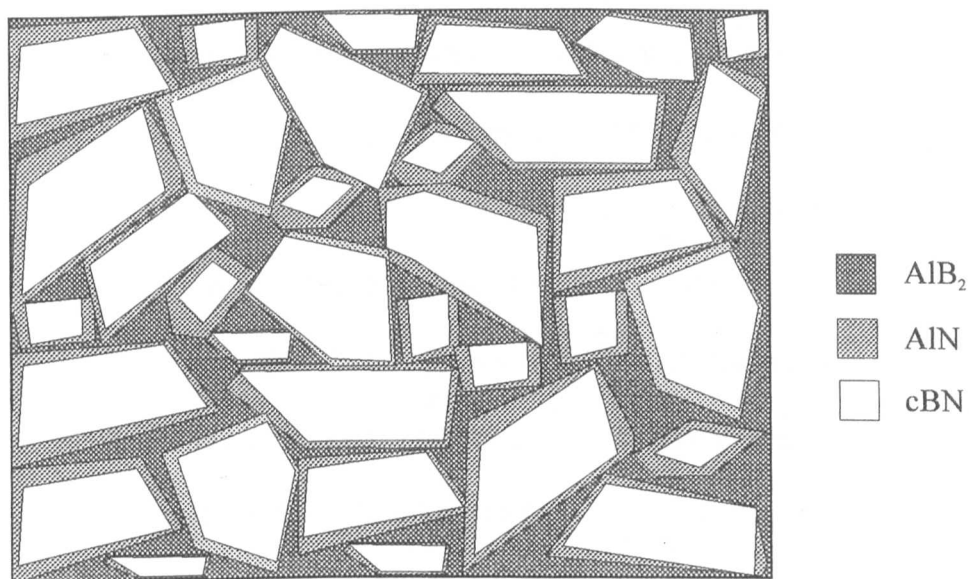
In this work, the cubic boron nitride compact used was Amborite (a De Beers PCBN product). In this material the aluminium binder melts and reacts with the hBN. The resulting cBN compact consists of a mixture of cBN, aluminium nitride (AlN) and aluminium diboride (AlB₂). The AlN covers the whole cBN particles, forming a rind around the grains and the AlB₂ occupies the channels between the cBN grains forming a rigid network. Under the sintering conditions, AlB₂ penetrates the spaces between the cBN grains leaving no voids or cavities (Walmsley and Lang, 1987). A typical microstructure and a schematic representation is shown in Figure 1.2.

A significant finding of Walmsley and Lang (1987) was that there is no free aluminium in the compact and this contributes to the inactive feature of the material. The AlN content is about 10wt% and the binder (AlB₂) content is 16wt%. Plastic deformation and fragmentation of the cBN particles were observed. Amborite behaves as a composite ceramic material since the regrowth which occurs during the sintering was reported to be very little (Tomlinson and Wedlake (1982)), however the low level of regrowth has been compensated by the greater contact areas between the cBN and the two intergranular phases, AlN and AlB₂.

The room temperature Knoop hardness and melting point of the three constituents of Amborite, AlN, AlB₂ and cBN are listed in Table 1.2.



(a)



(b)

Figure 1.2 : (a) SEM micrograph of the polycrystalline cBN (Amorite)
(b) Schematic illustration of the polycrystalline cBN (Amorite)

Table 1.2 The physical properties of the Amborite components

Compound	Knoop hardness (Hk ₁₀₀ GPa)	Melting point (K)
AIB ₂	9.6	1928
AlN	12	3273
cBN	30-45	3500

Pullum and Lewis (1990) analysed a cBN composite with silicon and nickel as binding materials and showed similar plastic deformation and fragmentation of the cBN particles as was shown in Amborite by Walmsley and Lang (1987). In this case less contact areas between the grains of cBN were observed. However, they reported that there was no evidence of a chemical reaction between cBN grains and either the nickel or silicon. The only reaction found to have taken place was between nickel and silicon, forming an intergranular phase (Ni₃Si₂).

All the TEM studies of cBN composites (Walmsley and Lang (1987); Britun and Pilyankevich (1990); Pullum and Lewis (1990)) agreed that the degree of plastic deformation ranged from a small number of slip lines to fully deformed particles. There was also fragmentation of particles into small pieces due to the high pressure. Furthermore, two types of deformation bands were reported in all the TEM analysis, i.e. slip bands and microtwin lamellae.

Hence, Amborite has been shown to be a composite material consisting of highly deformed cBN particles coated with AlN in a continuous matrix of AIB₂.

1.2.5 Industrial applications of cBN

CBN crystals are comparable in hardness with diamond and are much harder than the traditional abrasive materials such as Al_2O_3 , SiC and boron carbide (B_4C). Thus the grinding performance with cBN wheels is remarkably improved over the weaker known abrasives (Al_2O_3 , SiC) when grinding cast irons and high speed steels. Furthermore, it is well established that diamond materials have a great tendency to form carbides when machining ferrous materials (Trent, 1977), whereas cubic boron nitride is highly resistant to chemical attack when machining those materials.

The variety of polycrystalline products which can be made using hard particle cBN crystals as a base is immense. Change in the grain size, change in solvent/catalyst used, degree of sintering, particle size distribution all have certain effects on the mechanical, physical and thermal properties of the final product (Heath, 1986). Therefore it is possible to optimise the properties of a suitable material for a particular application.

The ceramic secondary phase in Amborite imparts high thermo-chemical stability and the solid format ensures a high degree of mechanical strength. Amborite is particularly suited for rough machining operations, without a coolant, where its high hardness and wear resistance, and toughness, can be used to advantage. In the area of the secondary shear zone the workpiece softens as a result of the self-induced, typically in the region of $750^\circ\text{-}1000^\circ\text{C}$, temperature but the high hardness of the Amborite permits excellent edge retention.

PCBN has a much superior thermochemical stability to that of diamond based materials and is particularly recommended for machining hard ferrous materials, where chip softening produced by the high cutting temperature reduces the amount of energy required and promotes chip removal. Here the major consideration is the coefficient of thermal conductivity of PCBN which is influenced by the cBN content - Amborite has a high cBN content with a relatively coarse grain structure.

In addition to Amborite, a new cubic boron nitride based cutting tool material - DBC, was developed by De Beers in the 1980's, primarily for precision finish machining of hardened tool steels. The combination of titanium carbide with cubic boron nitride has resulted in a range of composites DBC (cBN, TiC, Al (N), AlB₂) manufactured using the same ultra-high temperature and pressure technique used to make Amborite and polycrystalline diamond products. Produced in a revolutionary format a DBC layer, approximately 2 mm thick, is brazed on to a substrate in the temperature range 660° to 840°C using an interface of metal. These materials are not thermally sensitive. However a relatively low coefficient of thermal expansion significantly restricts the choice of substrate material - tungsten carbide being the most compatible. DBC50 - (50 : 50, cBN : TiC) has a refined homogenous microstructure, a high level of toughness and wear resistance and is ideally suited to fine machining. It is relatively easy to grind, using conventional diamond wheels, and in most situations a negative rake cutting geometry is preferred. With DBC materials the use of coolant is optimal but, in general, flood coolant improves dimensional

accuracy. However, for heavy stock removal, the coarse grade of Amborite is more suitable.

Another potential application area for cBN is in electronics. CBN is a III-V semi-conductor compound and its wide band gap makes it an excellent insulator. cBN also has high thermal conductivity and is suitable for use as a heat sink for semiconductor lasers and microwave devices.

1.3 Diamond

1.3.1 Introduction

Diamond is well known for its use in jewellery. This is mainly because it has an extremely low absorption of visible light, so that virtually no light is lost in the stone, coupled with a high refractive index (Table 1.1). However other properties namely: the extreme hardness; high thermal conductivity; a high elastic modulus; and relative chemical inertness; have made diamond a very attractive material for industrial and technological application. Unlike cubic boron nitride, which is a man-made material, diamond exists in nature as a single crystal and as polycrystals but can also be synthesised.

In the last four decades, since the announcement of the successful synthesis of diamond by General Electric in 1955, the importance of diamond as a strategic material for heavy industry and technology has increased. A factor which further contributed to the importance of diamond was the introduction of sintered polycrystalline diamond (PCD) in the 1970's.

Polycrystalline diamond (PCD), which is formed by sintering together a mass of selected sizes of diamond single crystals, is almost as strong and hard as the single crystal form. The random orientation of crystals in polycrystalline diamond

gives it an advantage over the single crystal form such that crack propagation is impeded and as a consequence it is tougher.

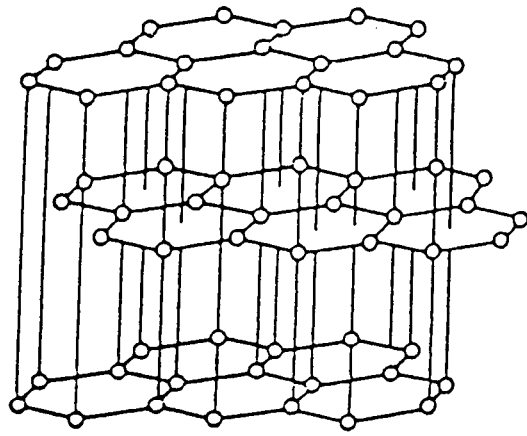
The larger available sizes of both natural and synthetic single crystal diamond gives it a further advantage over cBN and ensures its position as a superior product to cBN for many applications.

1.3.2 Crystal structure and physical properties of diamond

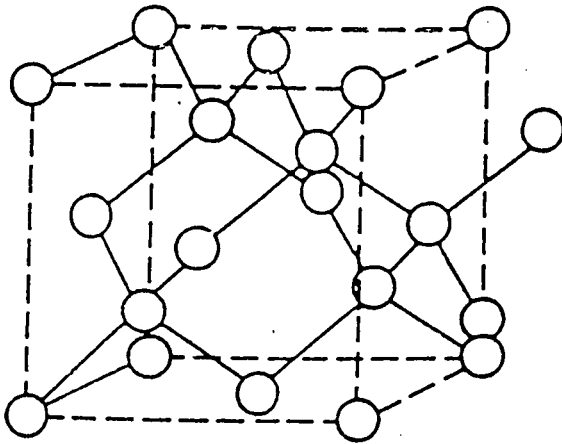
The strength of the bonds between atoms of a solid have a direct effect on the mechanical properties of that solid. Hardness and stiffness of solids are related to a large bonding force. However, for a material to be very hard, the bonds between the atoms must not only be strong, but their geometry must be symmetrical.

The two crystalline forms of carbon (hexagonal and cubic) have very differing physical and mechanical properties. In graphite, the carbon atoms are arranged in hexagonal layers (Figure 1.3a). Within a layer the atoms are packed tightly together, the distance between the atoms is 1.42\AA and the bond is covalent. However, the layers are quite widely spaced, i.e. they are separated by 3.354\AA and rely upon weak van der Waals bonds for structural integrity. Consequently, the layers are easily sheared and account for the use of graphite as a lubricant.

Diamond is composed of the covalently bonded single element carbon and crystallises in the diamond cubic (A4) crystal structure (Figure 1.3b). Covalent bonding is essentially quantum mechanical in nature and the simplest covalent bond is between two atoms joined together to form a molecule. Each carbon



(a)



(b)

Figure 1.3 : (a) The hexagonal form of atoms in graphite
(b) The cubic form of atoms in diamond

atom has a valency of four. The four outer electrons per atom fill the valence band making diamond electrically insulating. The valence band states, when occupied by electrons, give a lower overall energy than the corresponding single atom states. Thus the valence band states are responsible for the strong directional bonding and this imparts rigidity to the structure.

Carbon is the smallest atom in the fourth group of the periodic table of elements, and the relatively small size of the carbon atom has great impact on the exceptional properties of diamond. In diamond, each carbon atom lies at the centre of a regular tetrahedron, formed by equi-distant neighbouring carbon atoms (bond length 1.544Å) positioned at the apices of that tetrahedron.

The unit cell of the crystal is a cube with an atom at each corner, at the centre of each face and at four additional positions in the interior. Again, the diamond cubic structure can be described or interpreted as two interpenetrating face-centred cubic (fcc) cells with a displacement of $a/4[111]$ between lattices but, of course, all the atoms are carbon.

The slip systems of diamond are $\{111\} \langle \bar{1}10 \rangle$, the same as that of cubic boron nitride, and cleavage takes place in diamond on the $\{111\}$ planes.

A comparison of the physical properties of diamond and cBN is shown in Table 1.1.

1.3.3 Polycrystalline diamond

Synthetic polycrystalline diamond materials are aggregates of a selection of fine crystals randomly oriented and compacted together by a binder material. The random orientation of the crystals gives the material its unique resistance to crack propagation. A further advantage of PCD is that it can be manufactured to the required size.

There are several kinds of natural polycrystalline diamond in existence e.g. framesite, carbonado and ballas are the better known forms. However, their use is relatively low because they are quite rare in nature and it is difficult to shape them (Wentorf *et al* 1980). Framesite is the weakest form and ballas is extremely strong. The mechanical properties of these materials are totally dependent on the degree of impurities which exist in them.

Polycrystalline diamond can be produced in a variety of sizes and shapes and is commercially available in many forms. For example, Syndite (metallic-binder) and Syndax (ceramic binder) are registered to De Beers and Compax (metallic binder) is registered to General Electric.

1.3.4 Polycrystalline diamond synthesis

The production of polycrystalline diamond involves two stages. The first stage is the production of the diamond crystals. The second stage is to employ a similar

sintering technology as for single crystal synthesis to compact the diamond into the required shape, with the help of a binder.

Diamond is the metastable cubic form of carbon. The production of diamond is by transformation of the hexagonal form of carbon (graphite) to a cubic form under the appropriate conditions of pressure and temperature, with the help of a suitable catalyst. The pressure employed in the sintering process is 5-7 GPa and the temperature is about 2000°C. The sintering pressure can be decreased considerably with the aid of the right catalyst.

The possibility of polycrystalline diamond production began in the early 1970s when Hall (1970) employed 2500K and 6.5 GPa to produce a strong diamond compact called Carbonado. Katzman and Libby (1971), Wentorf and Rocco (1973) then announced that they had synthesised a promising new material, which was described as a sintered polycrystalline diamond compact, with a cobalt binder. Scanning Electron Microscopy showed that the diamond particles in this material were well distributed in the cobalt matrix and that some secondary diamond grain growth had occurred which had resulted in diamond to diamond bonding.

The strength of the diamond polycrystals is mostly dependent on the strength and extent of the diamond to diamond bonding resulting from the secondary regrowth process, which takes place during the ultra-high pressure and temperature of the sintering operation. Currently, most of the polycrystalline diamond materials available for industrial application are based on either a cobalt or a silicon binder. The introduction of silicon, by De Beers, was an attempt to

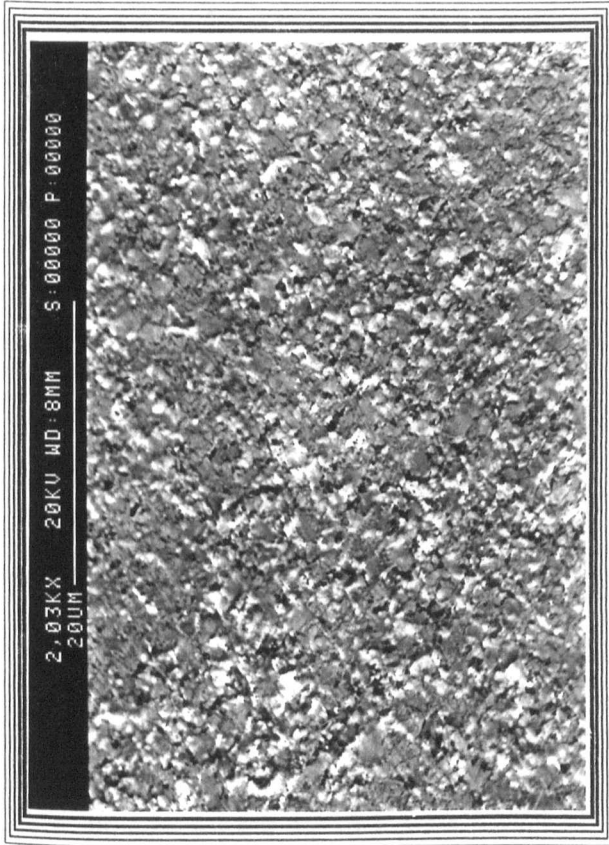
develop a more thermally stable compact tool suitable for rock drilling (Tomlinson *et al* 1985).

◆ **Syndite**

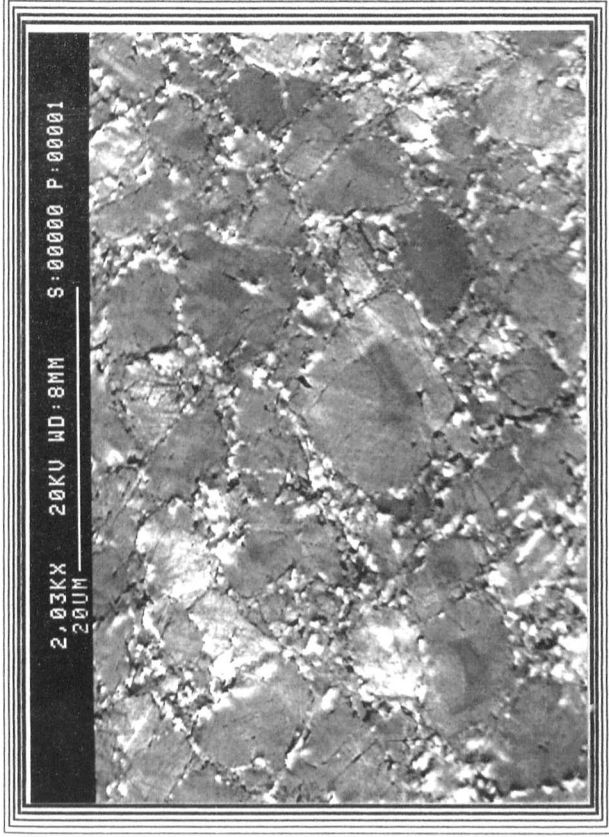
Syndite is a polycrystalline diamond cutting tool material produced by sintering synthetic diamond powder at pressures of about 5-6 GPa and temperatures of 1400-1500°C (Bex and Wilson, 1977). The diamond particle size of the Syndite varied in size ranges from 2 to 25µm (Figures 1.4 a, b and c) and the binder matrix is cobalt at about 8 vol%.

Two methods are commonly used for the production of Syndite (Tomlinson and Wedlake, 1983). In the first method, a mixture of diamond microgrit, cobalt and graphite are placed in a high pressure apparatus and then subjected to high pressure and temperature. Under these conditions, the graphite is dissolved by the molten cobalt and converted to new diamond which eventually acts as a cement to bind the diamond microgrit together. The result is a strong, tough, intergrown diamond compact which can be bonded onto a tool substrate, such as tungsten carbide.

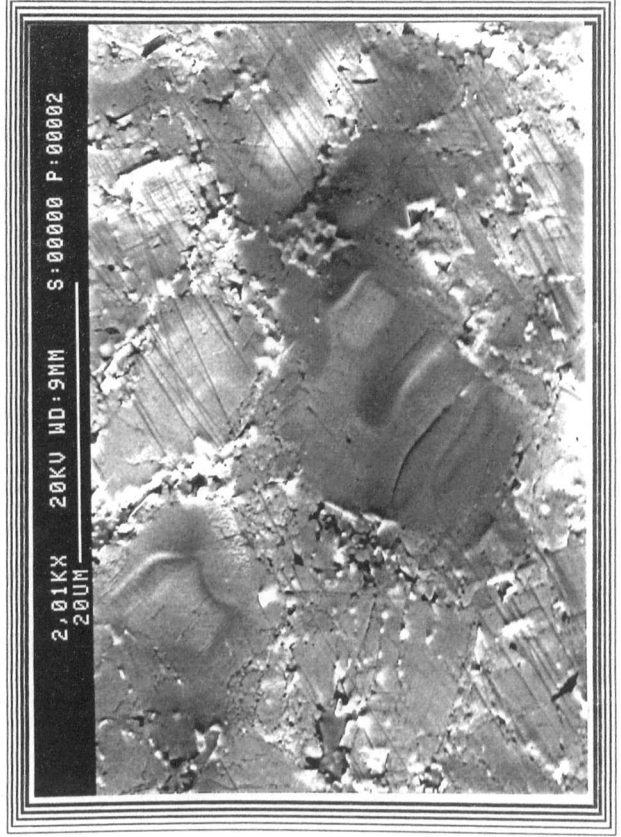
The second method, which is widely used, involves the use of infiltration techniques. In this method carefully selected fine diamond particles are placed in contact with a source of cobalt and subjected to high temperature and pressure. Under extreme high pressure, substantial plastic deformation takes place at the area of contact between the particles. However, away from the contact area the pressure on the diamond surfaces is quite low (Walmsley and Lang, 1988) and, due to the high temperature, these surfaces are converted to graphite. Then the



(a)



(b)



(c)

Figure 1.4 SEM micrographs showing
Syndite with:
(a) 2 micrometer diamond particles
(b) 10 micrometer diamond particles
(c) 25 micrometer diamond particles

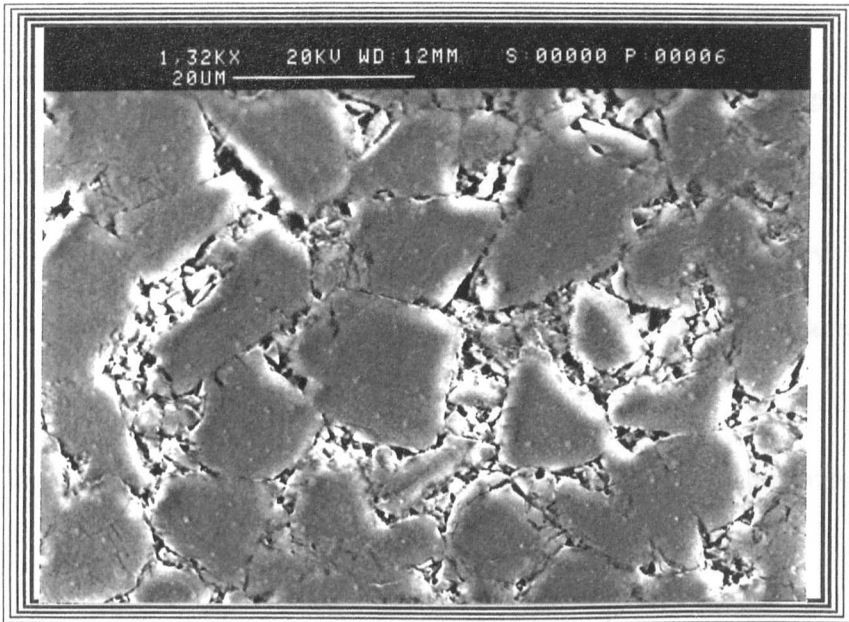
cobalt melts and infiltrates the voids in the compact, dissolving the graphite. In the region of high pressure, the carbon reconverts into a secondary diamond to form a bridge between the primary diamond particles. The infiltration of molten cobalt has a further advantage in that it cleans the diamond surface and takes away any impurities from the sintering region.

Polycrystalline diamond (PCD) was introduced to drilling technology in the mid 1970's and has proved superior to carbides and steel drill bits in many applications. For this purpose De Beers developed another version of polycrystalline diamond product i.e. Syndrill. Syndrill is also PCD with cobalt as the binder. However, Syndite and Syndrill were found to be thermally unstable, degrading at 700°C (Tomlinson *et al* 1985). To minimise this problem, a different binder other than cobalt had to be used and it was found that silicon binder served the purpose. The resultant compact product is Syndax (Tomlinson *et al* 1985).

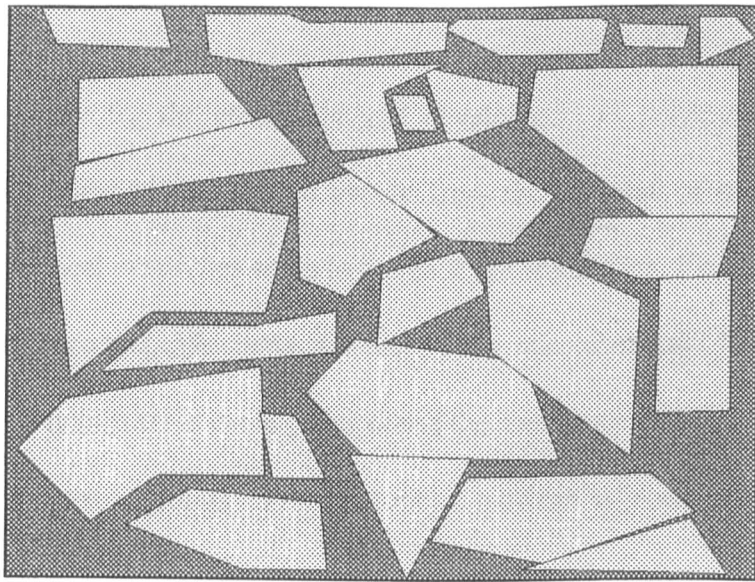
◆ Syndax

The manufacturing process of Syndax has the same roots as Syndite, in terms of high pressure and temperature. The process consists of sintering together densely packed diamond particles, approximately 15 μm in size, with silicon powder as a binder (see the micrograph in Figure 1.5a and the schematic in Figure 1.5b).

During the sintering process, most of the silicon reacts with the graphite to form the hard, abrasive and chemically stable compound, $\beta\text{-SiC}$. The silicon carbide binder weight is 16.5% to 18.9% by volume. The final product is a dense polycrystalline material of high strength which is thermally stable up to 1200°C.



(a)



(b)



Figure 1.5 : (a) SEM micrograph of the polycrystalline diamond (Syndax)
(b) Schematic illustration of the polycrystalline diamond (Syndax)

Tomlinson *et al* (1985) reported that when the silicon carbide was leached out of a Syndax specimen, the original size of the Syndax was maintained, due to the intergrown diamond network. They also demonstrated that, when only the diamond is removed by prolonged exposure to oxidation, there remains a similar honeycomb structure of SiC. The combination of these two interlocking networks, β -SiC and diamond, gives a high degree of toughness to the overall composite material.

1.3.5 The microstructure of Syndite and Syndax

The main driving force for the production and development of polycrystalline diamond and cubic boron nitride was to benefit from the potential of superior mechanical and chemical properties so as to increase the application, life and the effectiveness of the product. The understanding of the microstructural features of these materials is important in order to maximise the mechanical properties.

The pressure developed at points of direct contact between adjacent particles during manufacture of PCD is much greater than the nominal applied pressure used in the sintering process. Consequently these regions are subjected to localised high levels of plasticity. The nature of this deformation has been recorded in Amborite, Syndite and Syndax by the transmission electron microscope (TEM) studies of Walmsley and Lang (1988).

They concluded that, when the temperature rises during production, there is rapid conversion of diamond to graphite at the internal grains away from the high

pressure. The cobalt binder material in Syndite plays an effective role for re-transforming graphite to diamond.

A pronounced feature of the polycrystalline diamond microstructure is the high density of dislocations in diamond grains which were observed by Bex *et al* (1977), Yazo *et al* (1982), Lee *et al* (1984) and Walmsley and Lang (1983). The density of dislocations is highly concentrated in some regions, and it is supposed that it is these regions which have been subjected to high stresses during the sintering process. The grain boundaries are quite irregular and there is no clear orientation relationship between the grains.

Another feature of the PCD microstructure observed by Walmsley and Lang (1983) was the presence of microtwins which could be seen as a set of parallel lines within the grains. Some of the large grains were totally subdivided into smaller grains. In the case of Syndite, of grain sizes 2 and 10 μm , it was found that the grain size of the cobalt matrix material was larger than that of diamond in the compact (Walmsley and Lang, 1988).

In summary, the microstructure of Syndite can be described as a continuous cobalt matrix phase with primary diamond particles bridged by secondary diamond to form a continuous diamond skeletal structure. Consequently, the material is a sufficiently good electrical conductor to enable it to be machined by electro-discharge methods (spark machining) but its mechanical properties are significantly influenced by those of diamond.

In Syndax, however, the β -SiC binder is in the form of a fine grained (less than 1 μm), randomly oriented network (Tomlinson *et al* 1985). As in the case of Amborite, no intergrowth has been observed between the diamond grains, but

the diamond grains are welded together strongly as a result of high pressure and temperature during the sintering process. This has been substantiated by the observation of curved traces of microtwins around the areas of contact between diamond particles (Walmsley and Lang (1988)). A TEM analysis of Syndax by Walmsley and Lang (1988) showed similar severe localised plastic deformation as had been observed in the diamond crystals in Syndite. Deformation microtwin traces were seen within grains, in addition to a high concentration of dislocations. Furthermore, diamond grains were observed to have cracked during the consolidation process.

1.3.6 Industrial applications of diamond

The major traditional uses of industrial diamond are: grinding; polishing; drilling and other material cutting applications. These categories account for the largest amount of the marketed diamond volume. Until the development of synthetic diamond over 30 years ago these areas were dominated by the use of natural mined diamond, but the continued research and development in the field of diamond synthesis processes over the intervening period has seen a steady contraction of this position in favour of synthetic products.

In grinding there are different types of bonds used with diamond wheels: resin; metal; vitrified and electroplated-containing grits, ranging in particle size from about 10 μ m to several hundred microns depending on the application and the surface finish desired.

Although diamond can be used to grind and machine virtually any material, including ferrous alloys, it ultimately becomes a question of economics. The strong chemical affinity between iron and carbon results in relatively high tool wear. For this reason, the recommended abrasive and cutting tool material for ferrous workpieces is (cBN). Nevertheless, both single crystal and polycrystalline diamond are highly involved in the material cutting operations. Single crystals are normally used for fine cutting, and polycrystalline diamond tools are now widely used through industry for turning, boring and drilling operations for non-ferrous metals, superalloys, plastics and wood. An extremely comprehensive range of shapes, binders, sizes and grades of PCD cutting compacts are currently marketed by the manufacturers.

Another large area of PCD application is in drilling and mining. PCD drilling tools can now be found in underground operations for blast hole work, surface drilling, construction, as well as for deep hole mineral exploration. In these industries, engineers are always seeking tools with higher penetration rates and longer lives. PCD products, such as Syndrill, have already become well established in a wide range of drilling environments. However, the need for a tough, wear resistant PCD material of high thermal stability which could be employed in both hard and soft rock drilling, has driven De Beers to develop Syndax which is now widely used in drilling operations.

In addition to the above material removal applications, diamond materials are involved in other applications such as: electronic (as heat sinks and radiation detectors); optical applications (transmissive components and lasers) and surgical blades.

1.3.7 Thermal stability of PCD

The thermal stability of sintered polycrystalline diamond materials is very dependent on the quantity and the type of the catalyst/solvent used during the sintering process and the tendency of the diamond particles to reconvert to the hexagonal form i.e. graphite. The reversion is mostly to be expected at atmospheric pressure and high temperatures. However, the transformation problem can be stopped, or at least slowed down, when the material is in either a high vacuum or surrounded by an inert gas.

In polycrystalline materials the degradation due to graphitisation is not that serious on the surfaces of the hard particles because most of them are not exposed to the atmosphere. However, the binder material, such as cobalt in Syndite, is a solvent for carbon at temperatures less than the melting point of diamond (Bex and Shafto, 1984). Therefore, at low pressures the carbon dissolved in the cobalt is precipitated as graphite at the diamond grain boundaries, in a similar way to the original sintering process. However, during sintering, the pressure is high enough for the carbon to precipitate as diamond instead of graphite. When graphite precipitates in the grain boundaries of the polycrystalline materials, the structural integrity of the intergrown diamond material is undermined and there is a marked reduction in strength and abrasion resistance.

Furthermore, when the PCD compact is used at high temperatures, any difference in thermal expansion coefficient between phases causes additional

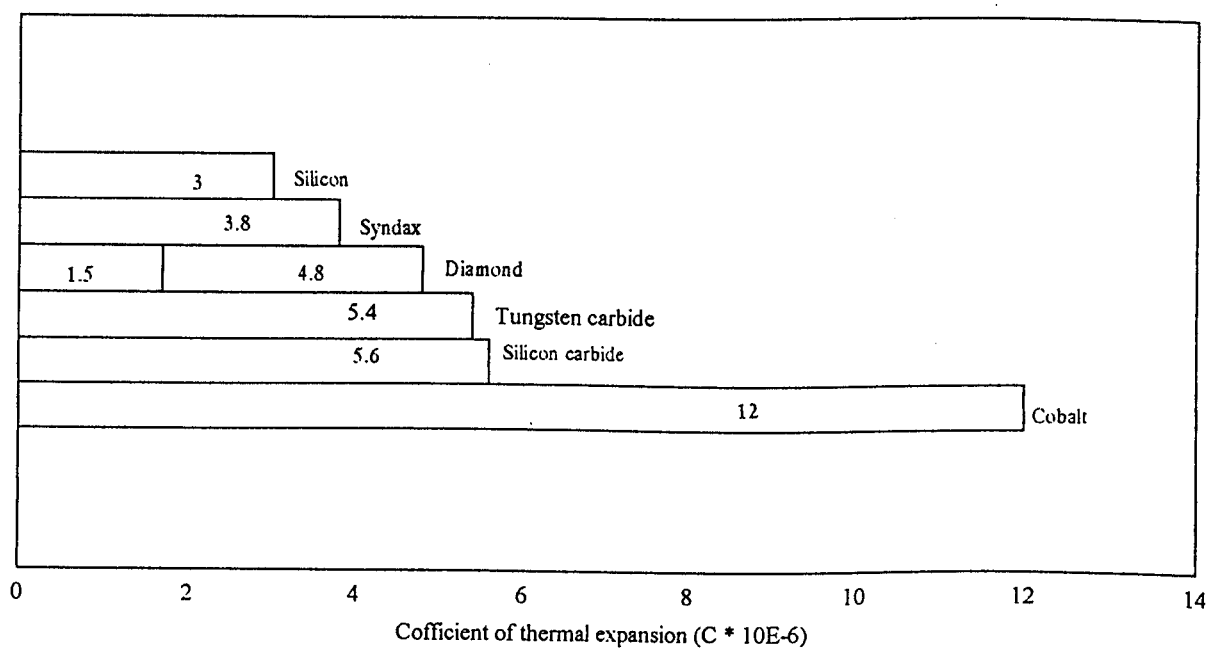


Figure 1.6 Coefficient of thermal expansion for the materials used in the PCD synthesis

problems. In Syndite, the large difference in thermal expansion of diamond and cobalt (Figure 1.6) will increase the internal stresses and hence may initiate cracks in the diamond. (Tomlinson et al, 1985). Also, the thermal expansion of the WC substrate is higher than that of Syndite so, at high temperatures, the thermal stresses at the interface (WC-PCD) are sufficient to cause delamination of the PCD layer from its substrate.

This problem is less severe in the case of Syndax because the coefficient of thermal expansion of silicon carbide and diamond are similar (Figure 1.6). It is found that this material (Syndax) is stable at 1200°C (Tomlinson *et al*, 1985), whereas the graphitisation in Syndite can be observed at temperatures above 700°C (Bex and Shafto, 1984).

1.4 Diamond coating

1.4.1 Introduction

Diamond grown at low pressure is a process which is currently being developed and which will replace high-pressure and high-temperatures diamonds in some applications. The advantages of diamond coating include the use of simpler apparatus, which is subjected to less mechanical wear and tear and the ability of producing different physical forms of diamonds.

Unlike bulk diamond, chemical vapour deposition (CVD) grown coatings can be used as optical coatings, friction-reducing coatings, corrosion-preventing coatings, wear-resistant coatings and semi-conductor layers on less expensive materials. Due to the potential advantages, methods for the synthesis of diamond

coatings have attracted the attention of a number of research groups in many countries in recent years.

One of the most important developments in techniques has been the synthesis of diamond by chemical vapour deposition (CVD) and methods have been developed for nucleating diamond on non-diamond substrates (Spitsyn *et al* 1981; Kamo *et al* 1983). In the last decade, a number of different techniques to grow diamond by CVD process have been developed.

1.4.2 Deposition and characterisation of diamond coating

The growth of pure diamond coatings from the vapour phase on non diamond substrates at practical rates was accomplished with the development of thermal and plasma enhanced CVD methods, in which a hydrocarbon gas (usually methane), mixed in low concentrations with H₂, is energised thermally or in a plasma prior to contact with a heated substrate. True diamond crystals and coatings have been grown, without graphite co-deposition, on a variety of substrates.

The first of these enhanced CVD methods was the chemical transport reaction (CTR) synthesis reported by Deryagin *et al*, 1976. The development of hot filament assisted thermal CVD followed, reported by Matsomoto *et al* 1982. From that date many processes have been developed: electron-assisted thermal CVD (Sawabe and Inuzaka 1985), laser-assisted thermal CVD (Kitahama *et al* 1986); RF-plasma CVD (Matsomoto 1985); microwave-plasma CVD (Kamo *et al* 1983); and remote microwave-plasma CVD (Saito *et al* 1986). Although

these techniques have some differences in their details, they have a number of common features.

- ◆ The structural features of the deposits depend on the growth conditions, most critically on the gas composition (C:H or C:H:O ratio) and the substrate temperature.
- ◆ The substrate temperature affects the CVD diamond growth in a variety of ways. Diamond films were reported to be grown at substrate temperatures between 500°-1200°C. Growth at temperatures above 1200°C was found to lead to graphite, and growth at temperatures less than 500°C, using hydrocarbon hydrogen mixtures, was found to lead to diamond-like carbon (DLC) deposits (Spitsyn *et al* 1981). However the low temperature limit has been extended to temperatures as low as 300°C, using C-H-O containing gas mixtures (Rudder *et al* 1992).
- ◆ The substrate temperature was found to affect the crystal habit of growth. The commonly observed crystal habits include octahedral and multiple twinned particles. Matsomoto *et al* (1982) reported that (111) crystal faces dominate at lower pressure and temperatures, while polyhedral crystals with (111) and (100) faces dominate at higher temperatures and pressures.

For coatings grown at lower methane concentrations, (111) faces were more frequent, with a high density of twin boundaries, whereas (100) faces, which appear as square or rectangular forms, were predominant for the coatings grown at methane concentrations higher than about 1.5%. For the films grown at 5% methane concentration, the crystalline morphology was totally lost (Sato and Kamo 1992).

These authors employed the plasma etching technique to reveal the structural features of the coatings. For the 4% methane coatings, intergrain regions were removed by structural etching, leaving crystal grains with smooth, faceted surfaces and cross-sections of these have shown that they are needle crystals. The smoothness of the surface also suggests that the grains are of better quality compared with grains in the 0.3% and 0.5% methane coatings.

The texture of the coatings deposited at methane concentrations of 0.3-4% is always columnar. For coatings deposited at 0.3-3% methane concentrations, the grain size, defined by the diameter of the columnar grain, is about 0.2-0. μm near the substrate and grows to about 2-3 μm at a distance greater than about 10 μm from the substrate surface. For the 5% coatings a texture similar to a spider's web remained.

Sato and Kamo (1992) studied the Raman effect on diamond coatings. The Raman effect is the shift in the frequency of light scattered from a crystal and is a sensitive indicator of the structural perfection of a diamond crystal. A peak shift of 1-2 cm^{-1} to higher Raman wavenumbers was often observed for the samples prepared at 0.5-2% methane concentrations. No change in the line width or peak shift was observed when the coatings were freed from the substrates by treatment with mixtures of hydrofluoric and nitric acids. Microprobe measurements on the cross-sections showed that the peak shift was larger (by about 1 cm^{-1}) at the substrate side of the coating than at the surface for the coatings. Furthermore, the peak shift observed with the polycrystalline coatings was related to internal stress. The effect of thermal stress as a result of the difference in the thermal expansion coefficients of the coatings and the

substrates, was much smaller for those samples as the peak displacement was only slightly affected by removing the coatings from the substrates. Sato and Kamo noted that the shift was larger at the substrate side of a coating, where the grain size is smaller by an order of magnitude, than at the surface. It seems that a great part of the stress is caused by the grain boundaries, where the defect density is higher.

1.4.3 Physical properties of CVD diamond

The methane concentration has been shown to have an effect on the structural features of CVD diamond which influences the overall physical and mechanical properties of coatings. This was confirmed by Sato and Kamo (1992) when they measured the density of diamond coatings with different methane concentrations. They evaluated the densities of coatings formed at methane concentrations of 0.3 and 0.5% and they found the density to be 99.8 and 99.7% of that of natural diamond (3.515 gcm^{-3}) respectively, i.e. the density decreased gradually with increasing concentration. A sharp decrease to 3.3 gcm^{-3} , or 94% of the value of natural diamonds was observed with coating deposited at 5% methane, where the difference in density is predominantly due to the co-deposition of disordered graphite.

Furthermore, Sato and Kamo (1992) have measured the bulk modulus of different diamond coatings. Their measurements have shown that the highest elastic constant, 90% of that of natural diamond, was observed with the coating formed at methane concentrations of 0.3 and 0.5%. The modulus decreased

gradually for coatings formed at higher methane concentrations up to 4%, and again a sharp decrease was observed with the coating formed at 5% which consisted of fine particles of diamond and disordered graphites. The high modulus values of the coatings prepared at lower methane concentrations indicate that the bonding strength is high.

The thermal conductivity of the coating prepared at 0.1% methane was $\approx 1000 \text{ W m}^{-1} \text{ K}^{-1}$ at 100°C and decreased sharply with increasing methane concentration. This value of $1000 \text{ W m}^{-1} \text{ K}^{-1}$ at 100°C is comparable with that of natural diamond $600\text{-}1000 \text{ W m}^{-1} \text{ K}^{-1}$ (Field 1992).

1.4.4 The applications of CVD diamond

As mentioned previously, the main interest in diamond coatings centres on three different fields of applications: their use as hard protective coatings on tools and other devices; the possibility of constructing semi-conducting electronic devices; and as a valuable development to previous methods of growing diamond under controlled conditions.

Firstly, the coating of cutting tools such as WC and silicon nitrides by diamond is largely welcomed in the industry, in order to combine the high hardness of diamond with the toughness of the substrate. However, there are obstacles slowing the development of this field, such as the problem of obtaining and measuring good adhesion between the coating and the substrates.

Secondly, the interest of using diamond coatings for semi-conductor devices has been derived from the possibility of growing diamond doped with boron so as to

produce semi-conducting diamond. Finally, the development of CVD diamond has provided the opportunity to grow diamond with more precise and controlled properties, e.g. coatings which are grown from methane isotopically enriched to have very low content of isotope ^{13}C . Here the diamond sheet was then powdered and used as starting material to produce single crystals of diamond about 1 ct in size, with a low concentration of ^{13}C (Anthony *et al* 1990). This diamond has a very high thermal conductivity and potential value as a heat sink material.

In this work, the DeBeers version of coated diamond i.e. CVDite was used. CVDite was produced as cutting tool inserts by chemical vapour deposition of diamond onto a silicon carbide substrate.

1.5 Measurement of specific mechanical properties of ultra-hard materials

1.5.1 Fracture of ultra-hard materials

◆ Cleavage

Single crystal materials normally exhibit irregular fracture surfaces, but may also fracture by a regular cleavage along a certain crystallographic planes. In diamond the dominant cleavage plane is the (111), however other cleavage planes have been reported. The explanation for the preference for (111) cleavage is based on the consideration that cleavage is most likely to occur across planes with the lowest fracture surface energy. Calculations based on the bond strength of carbon, and the density of bonds on crystal planes, confirm that the (111) plane has the lowest cleavage energy i.e. 10.6 Jm^{-2} (Field, 1992).

De Vries 1972, has reported that the preferred cleavage plane for cBN single crystals is (011).

◆ Hertzian fracture

The Hertz test is a common method of assessing the strength of brittle materials. It consists of forcing a hard sphere against a flat surface of the specimen to produce a crack just outside the area of contact. The crack propagates downwards and outwards to form a cone extending into the material. Considering the material as isotropic, the stress field is compressive inside the contact area, but tensile outside with the maximum tensile stress at the edges of the contact area (Hertz, 1881). The maximum compressive stress occurs on the surface under the axis of the indenter (sphere) and has the value:

$$P_{\max} = 1.5 P_{\text{mean}}$$

where $P_{\text{mean}} = \frac{P}{\pi a^2}$ (P is the load on the sphere and a is the radius of the contact area).

When the indenter and specimen are of the same material the value of this radius is given by:

$$a^3 = \frac{1.5(1 - \nu^2)PR}{E}$$

where ν is the Poisson's ratio, R the radius of the indenter and E the Young's modulus.

The maximum tensile stress is: $\sigma_m = 0.5 (1 - 2\nu) P_{\text{mean}}$

The anisotropic behaviour of diamond single crystals alters the stress field caused by an indenter and encourages the cone cracks to propagate along the (111) cleavage planes.

An estimate of the fracture surface energy has been made by observing the growth of cone cracks on (001) faces, where the (111) cleavage planes are inclined at about 54° to the surface. Field and Freeman, (1981) obtained a value of $5.50 \pm 0.15 \text{ Jm}^{-2}$ for the fracture surface energy of (111) planes which is comparable with the estimated theoretical value (5.3 Jm^{-2}).

The fracture toughness of single crystal diamond may be evaluated by using the values of the fracture energy measured above. However, for polycrystalline materials (PCD and PCBN) only surface cracks are visible. Therefore, the toughness must be evaluated by methods which measure the stress required to fracture specimens of a particular geometry, or by measuring cracks induced by an indentation test.

The values of the elastic constants and of the strength of PCD materials are somewhat less than those for single crystal diamond, but the fracture toughness of PCD is higher than that of single crystal (Table 1.1). It is this combination of high strength and high toughness which makes PCD outperform single crystal diamond in some applications.

1.5.2 Plasticity of ultra-hard materials

Plastic flow

Early work has shown that plastic flow of diamond occurs at 1800°C. Evans and Wild (1965) mounted small polished plates of type I and II diamond on two tungsten wedges and loaded the upper side of the plate with a third wedge (three-point bending) at 1800°C. They suggested that the transition from brittle fracture to plastic bending for type II occurred at temperatures of about 1600°C and indicated that type I diamonds were more resistant to plastic flow. They explained the difference between the behaviour of the two diamond types as being due to the high levels of impurity atoms or groups of atoms in type I diamond and suggested that dislocations are pinned or their movement restricted by the impurities (Wild *et al* 1967). However, the recent findings of Brookes and his research group (Chapter 3, section 3.3) contradicts this result (Brookes *et al* 1990).

The occurrence of plastic deformation at room temperature in diamond has been a subject of great controversy for many years. Indentation experiments have shown that limited plastic flow at 20°C could occur. Howes and Tolansky

(1955) pressed a diamond ball of radius 0.39 mm onto a flat diamond surface and suggested that the material displaced on either side of the indentation was pushed there by plastic flow during deformation. Further evidence to demonstrate plastic flow during indentations at room temperature was forwarded by Brookes (1970) when he used a Knoop indenter on the {001} diamond face in $\langle 001 \rangle$ and $\langle 110 \rangle$ directions. The indentations on the $\langle 110 \rangle$ direction were consistently much larger. Measurements made with a load of 100gf resulted in indentations with no sign of cracking at the macroscopic level which suggests that, under this load, plastic flow had occurred.

By developing the soft impression technique to study the onset of diamond plasticity at high temperatures, Brookes and his group have shown that type 1b diamond deforms plastically more readily than type 1a and that multiple intersecting slip is observed at much lower temperature i.e. about 1000K. Also, it was shown that, under these conditions, type II diamond has a greater resistance to plastic deformation than the other types of diamond measured. In that the onset of plasticity occurs at about 1300K. Furthermore, the critical resolved shear stress increases in the order type $I_b < I_a < II_a$ at a given temperature.

◆ Indentation hardness of ultra-hard materials

The indentation hardness test is a very useful method for assessing some of the mechanical properties of ultra hard materials and this method is widely used for materials such as diamond and cubic boron nitride. The microhardness test is useful for small samples, with restriction on geometry and can be used as an indicator of the strength of the material. For polycrystalline metallic materials the

mean contact pressure (hardness) is related to the yield stress of the material in simple compression as:

$$P_m = C\sigma_y$$

where C is a constant whose value is about 3 (dependent on the geometry of the indenter) (Tabor 1951).

Hardness measurement of all materials is affected by a number of experimental variables such as anisotropy in single crystalline materials, i.e. the difference in the measured hardness as the orientation of the indenter is changed with respect to the crystallographic plane of the indented surface; the normal load; the dwell time over which the indenter is loaded against the specimen; and the experimental environment (Brookes *et al* (1990)). Table 1.3 shows the Knoop hardness of diamond, cBN and some single crystal cubic materials at room temperature.

Table 1.3 Comparisons of Knoop hardness [in GPa] of hard cubic crystals at room temperature

Crystal	Slip system	Knoop hardness number (GPa)			
		(001) <100>	(001) <110>	(111) <001>	(111) <112>
Diamond type I	{111} <110>	98	83	56	63
Diamond type II	{111} <110>	103	91	76	110
cBN	{111} <110>	43	30	39	41
TiC	{110} <110>	20	28	-	-
MgO	{110} <110>	4.0	7.8	8.5	6.9

Brookes and Lambert (1982) investigated the effect of the above variables on polycrystalline materials, i.e. Amborite and Syndite. They concluded that the indentation hardness of the cubic boron nitride aggregate material Amborite is strongly influenced by the indentation size effect i.e. hardness increases with increasing normal load. The effect of the applied load on Amborite puts it in the same line with other covalent solids, such as diamond and silicon carbide. As shown in Figure 1.7, the hardness of Syndite and Amborite decreases with increase in temperature and the rate softening of the single crystals is greater than that the composite material.

Also, Brookes (1986) has shown that the hardness of cBN aggregate and single crystal cubic boron nitride decreases with the increase of dwell time at high temperature, Figure 1.8. These results were used to provide information on the indentation creep deformation of the material tested. Guillou *et al* (1990) also showed that time dependent deformation occurs in cBN aggregate, even at room temperature under indentation conditions. These authors used a Vickers indenter to measure the change in hardness with dwell time and observed a 15% decrease in hardness over the range 10 to 31,500s. In a separate study, Hooper *et al* (1991) found that the time dependent behaviour of (cBN-TiC (DBC50)) was similar to the Amborite aggregate. In their investigation, Guillou *et al* (1990) showed that the hardness of cBN aggregate (Amborite) on the flank face was lower than that on the rake face and that the rate of creep also differed between the flank and the rake face. They explained this phenomenon by suggesting that a recovery process takes place parallel to the rake face, since this anisotropy was

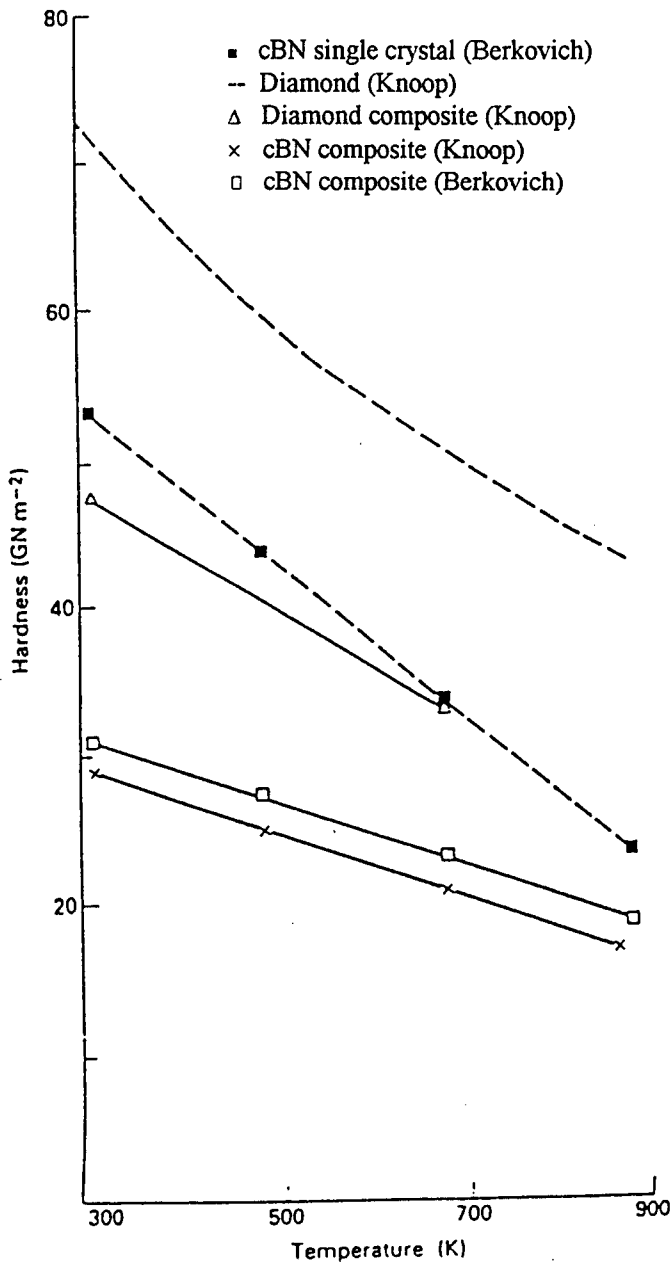


Figure 1.7 The effect of temperature on the hardness of ultrahard materials (Brookes and Lambert, 1982)

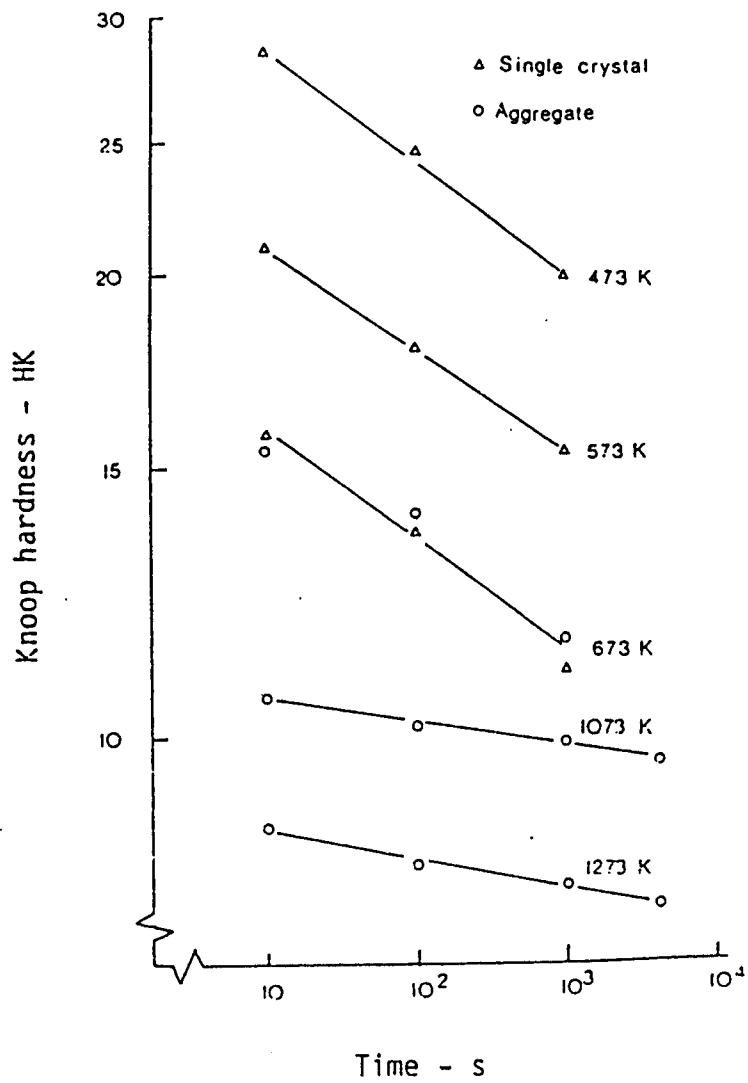


Figure 1.8 The effect of increasing dwell time on the hardness of cubic boron nitride (Brookes, 1986)

not observed by using Knoop indenter which is assumed to be insensitive to recovery effects.

1.5.3 Friction and wear of diamond

◆ Friction of diamond on diamond in air

Most of the studies in this field have been based on the friction of single crystal diamond sliding on single crystal diamond. The coefficient of friction (μ) is usually of the order of 0.05 to 0.1. These values are relatively low compared with other materials, for example unlubricated metals. At low speeds (a few millimeters per second), the frictional values were found to be independent of the speed of sliding (Casey and Wilks, 1973). At higher speeds, it was expected that the coefficient of friction increases due to the generated frictional heat, which results in oxidation of the diamond.

One of the main features of the friction of diamond sliding on diamond is that the value of μ depends on the crystallographic orientation of the polished face with respect to the direction of sliding. Measurements on polished {001} faces by Seal (1958) and many others have shown a marked variation of the coefficient of friction with direction. Generally, the friction measured in the $\langle 110 \rangle$ direction was smaller i.e. $0.06 < \mu < 0.08$, whereas, in the $\langle 100 \rangle$ direction the value of μ was almost double i.e. $(0.1 < \mu < 0.15)$. In the case of diamond sliding on diamond, the addition of a lubricant has little effect on the friction coefficient (Bowden and Tabor, 1965, Casey and Wilks, 1973).

◆ Friction of diamond in a vacuum

Under high vacuum conditions, the friction coefficient of diamond sliding on diamond can reach relatively high values ($\mu \approx 1$) compared with that observed in air ($\mu \approx 0.1$). If the surfaces are contaminated but slide repeatedly over the same track, the initial friction is low and increases gradually until after a few hundred traversals a value of about $\mu=1$ may be reached (Bowden and Hanwell, 1966). If air is then admitted, the friction falls, which suggests that adsorbed films formed by reaction with normal atmosphere act as a form of lubricant and that these films are removed mechanically by the repeated traversals. A similar increase in friction can be obtained by heating the surfaces at about 1000C in the vacuum before sliding occurs.

◆ The mechanism of friction

Friction is a complex process which must result from a variety of mechanisms. A satisfactory explanation of the mechanisms which dominate the activities in the interface is not yet available.

In 1964, Bowden and Tabor suggested that the friction is attributed to the atomic bonding between diamond surfaces. However, the absence of any change in friction with the addition of lubricating oil suggests that adhesion between the diamonds is small, which reduces the validity of the adhesion theory.

Casey and Wilks, (1973) suggested that in air, diamond friction is highly influenced by the surface roughness and that the coefficient of friction depends on the detailed topography of the surfaces, in particular the steepness of the asperities. When a stylus moves over the surface, the energy gain when it climbs

an asperity is not balanced by an equal loss as it descends it. Casey and Wilks (1973) assumed that an irreversible energy loss of about 10% of the stored energy at each encounter is sufficient to account for the magnitude of the friction. However, a loss of 10% by phonon production is large for diamond, which led Tabor (1979) to propose the presence of an adhesive force between the interacting asperities.

Tabor (1979) also suggested that the friction could be caused by microplastic deformation. In support of this suggestion, Brookes *et al* (1987) reported observations of the wear of other hard non-metallic crystals when traversed by softer metal cones. They indicated that, in sliding, plastic deformation occurred at room temperature. Recently, Feng and Field (1991) provided evidence from electron microscopy studies that, in sliding friction, plastic deformation could be involved in frictional deformation at high loads.

◆ Wear

The major shaping process of diamond is by grinding or polishing on a rotating cast iron wheel charged with diamond powder (Wilks and Wilks 1972). Considerable diamond to diamond contact occurs in this process and the rate of removal of material depends on the plane of the diamond being polished and the direction of the abrasion. The soft directions (easy to abrade) correspond to the high friction directions. This dependence is more pronounced in conditions of wear and removal rates may differ by as much as 100:1. Values are dependent on whether loose diamond powder or a wheel with bonded diamond is used.

The amount of diamond abraded is proportional to the number of revolutions of the scaife, and does not depend on its speed (assuming that speed is not high enough to generate sufficient heat to cause graphitization of the diamond). This suggests that the wear mechanism is not thermally activated, as higher speeds normally generate high temperatures.

Tolkowsky (1920) proposed a micro-chipping mechanism to explain the wear anisotropy. His theory predicted that the surface of diamond is not smooth but is covered with steep sided asperities of very small size. Tolkowsky suggested that small octahedral and tetrahedral chips of diamond are removed, formed by the (111) easy cleavage plane. As a result, different faces and directions have different abrasion rates because certain orientations of the cleavage planes encourage cracking, while others hinder it. However, direct evidence in support of this mechanism has not been obtained despite much electron microscopy on worn surfaces (Wilks and Wilks 1991). Furthermore, recent work has lead to the suggestion that the wear mechanism is due to degradation of diamond rather than a strictly mechanical effect (Grillo, 1996)

1.5.4 Some relevant mechanical properties of PCD and cBN

The mechanical properties of polycrystalline diamond and cubic boron nitride differ according to the source of the products. As stated previously PCD and cBN represent a range of products produced by different sintering techniques, catalyst/solvents, grain size and the volume fraction of the hard particles to the binders. Some of the important mechanical and physical properties of polycrystalline diamond, cubic boron nitride, WC and ceramics typical of cutting tool materials, are summarised in Table 1.4. In this table, Syndax, cBN and Syndite are presented as examples of ultra-hard cutting tool materials.

The fracture toughness of polycrystalline diamond and cBN (a measure of the resistance to crack propagation in a given material) is much higher than that of diamond single crystals and is almost equal to that of tungsten carbide. The high value of toughness has been achieved by the random orientation of the diamond particles which prevents the passage of a crack front from one grain to another.

Gigl (1979) and Roberts (1979) have determined the Young's modulus of PCD (with cobalt binder) as 780 GPa. This value is similar to that of Lammer (1988), who determined many mechanical properties for De Beers products and compared them with other ceramic materials (Table 1.4).

Roberts (1979) measured the Poisson's ratio (ν) of PCD materials in compression tests and obtained a value of about 0.22. However, a value of 0.07 was obtained for similar material by Lammer (1988). This value is similar to that reported by Field (1983) and it is in good agreement with the measurement of

Gigl (1979). Furthermore, this value compares directly to that of diamond single crystals. This is explained by the nature of PCD structure (see previous sections). The bulk and shear moduli of diamond are derived from calculations using a Poisson's ratio of 0.07 and Young's modulus of 1141 GPa.

Table 1.4. Mechanical properties of polycrystalline diamond and cBN compared with other ceramic tool materials.¹²³

	Al ₂ O ₃	WC (K10)	Syndite 10µm	Syndite 25µm	Syndax	Amborite	Diamond
Density (g.cm ⁻³)	3.91	14.7	4.12	3.86	3.43	3.42	3.52
Compressive strength(GPa)	4	4.5	7.6	7.61	4.74	2.73	8.68
Fracture toughness (MPa.m ^{0.5})	2.33	10.8	8.81	8.89	6.89	10	3.4
Knoop hardness (GPa)	16	13	50	50	50	32	57-104
Young's modulus (GPa)	340	620	776	810	925	680	1141
Shear modulus (GPa)	154	256	363	379	426	279	533
Bulk modulus (GPa)	243	375	301	314	372	405	442
Poisson's ratio	0.24	0.22	0.07	0.07	0.086	0.22	0.07
Coefficient of thermal expansion(10 ⁻⁶ k ⁻¹)	8.5	5.4	4.2	4.6	3.8	4.9	1.5-4.8

¹ Tomlinson *et al* (1985)

² Lammer (1988)

³ R Heath (1986)

Chapter 2 Apparatus and experimental procedures

2.1 The high temperature apparatus

All the impression and sliding friction measurements were carried out using the high temperature apparatus which is shown in Figure 2.1. A radio frequency (R.F) generator (38Kw, 450khz) was used to supply power to a water cooled copper coil inside a vacuum chamber. This vacuum chamber is evacuated by rotary and diffusion pumps to achieve a typical working vacuum of 10^{-5} mbar. The vacuum in the chamber allowed the working temperature to be increased minimising the extent of oxidation and graphitisation of diamond. Other atmospheric media such as inert gases could be introduced through a special inlet valve designed for this purpose but this facility was not used in this project. The specimen was held by a graphite susceptor placed in a movable water cooled hearth and within the coil. The graphite susceptor was directly heated by the induced e.m.f. which produced controllable and reproducible experimental temperatures in the range 700° - 1800° C.

In this apparatus, the normal load was generally 100N. This was developed due to the difference in pressure outside the chamber (atmosphere) and inside it (10^{-5} mbar) and the weight of the crosshead. This load was monitored by placing a load cell in the top of the susceptor and allowing the load to be applied through a flat impressor. To increase the load, weights were added to the load support beams on the turret. On the other hand, the turret weight could be counterbalanced with extra weights on a pulley system in order to decrease the load.

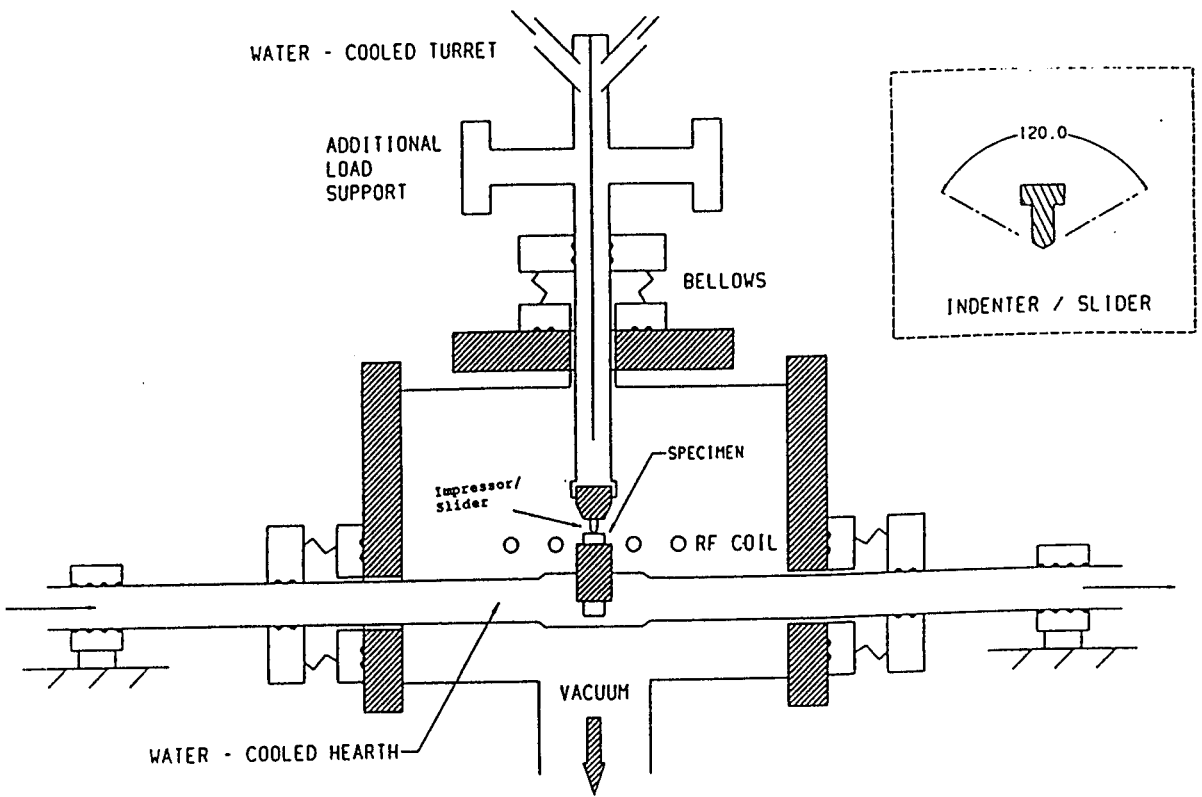


Figure 2.1 Schematic of high-temperature apparatus

For high temperature experiments the impressor/slider was fixed in a pyrophyllite holder in a water cooled turret above the specimen surface. Pyrophyllite was used because of its insulation properties and high melting point. For experiments at room temperature, a stainless steel holder was used.

A flexible bellows attached to both sides of the chamber maintained the vacuum whilst allowing the hearth to be moved in the x direction (left and right). A servo motor with variable speed was used to drive the hearth through the flexible bellows. The distance through which the specimen was moved was limited by the inside diameter of the induction coil and the diameter of the susceptor i.e. about 50mm. Also, the hearth could be moved back and forth manually (y direction), which enabled a series of sliding tracks and impressions to be performed whilst keeping the other experimental conditions constant.

2.2 Calibrating and recording the frictional force

The friction force developed between the slider and the specimen by moving the sample under the slider, was measured using a calibrated load cell mounted at the end of the hearth (Figure 2.2) The movement of the hearth was achieved by a variable speed servo motor with a sliding speed of up to 9mm/min. During the sliding process the load cell output was fed into an amplifier and then to an (x, y) chart plotter. The load cell was mounted in line with the hearth and was directly calibrated with weights attached to a string passed over a pulley wheel at the other end of the hearth. Having known weights and measuring the displacement on the chart recorder (Figure 2.3), a calibration curve (Figure 2.4) was then plotted to convert displacement on the (x,y) chart to frictional force.

RECORDER & AMPLIFIER

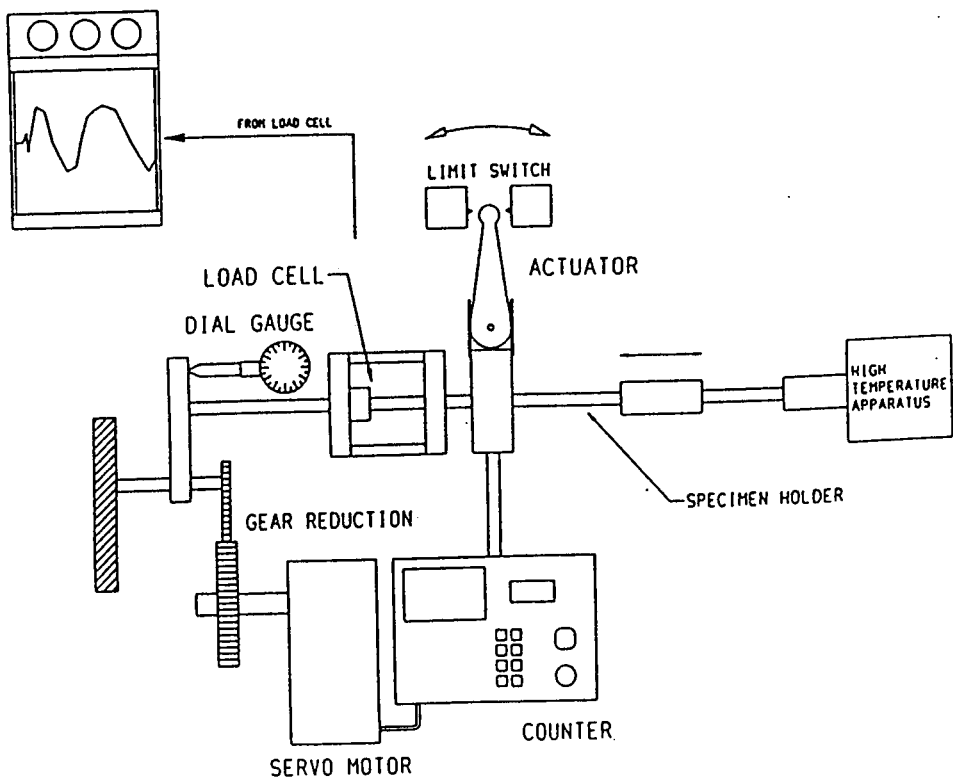


Figure 2.2 Schematic representation of sliding friction unit

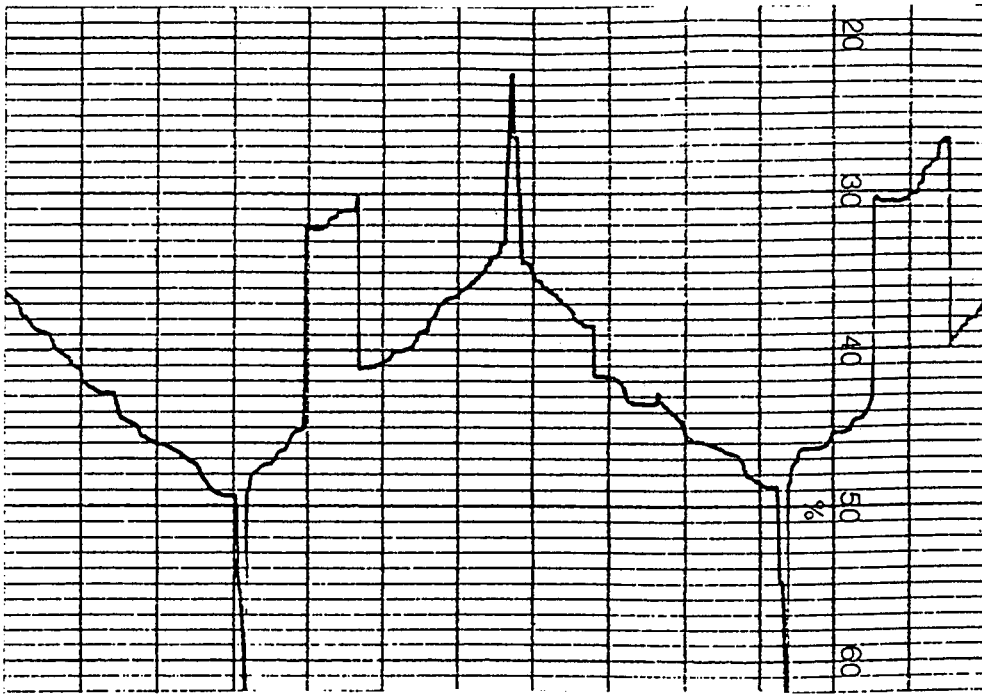
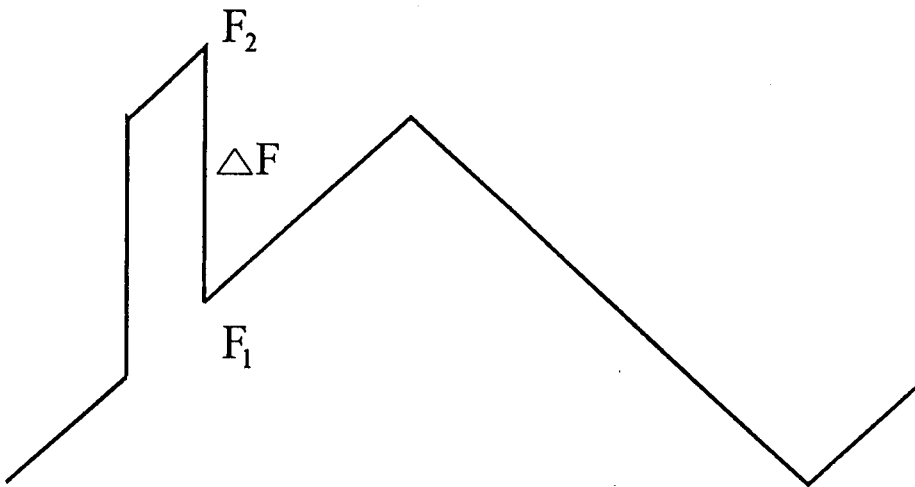


Figure 2.3 (a) Typical recording of the friction force during the reciprocation of the slider



- ΔF = Frictional force between surfaces
- F_1 = Background frictional force
- F_2 = Frictional force due to loading slider on the flat surface

Figure 2.3 (b) Schematic representation of the friction force recordings during the reciprocation of the slider

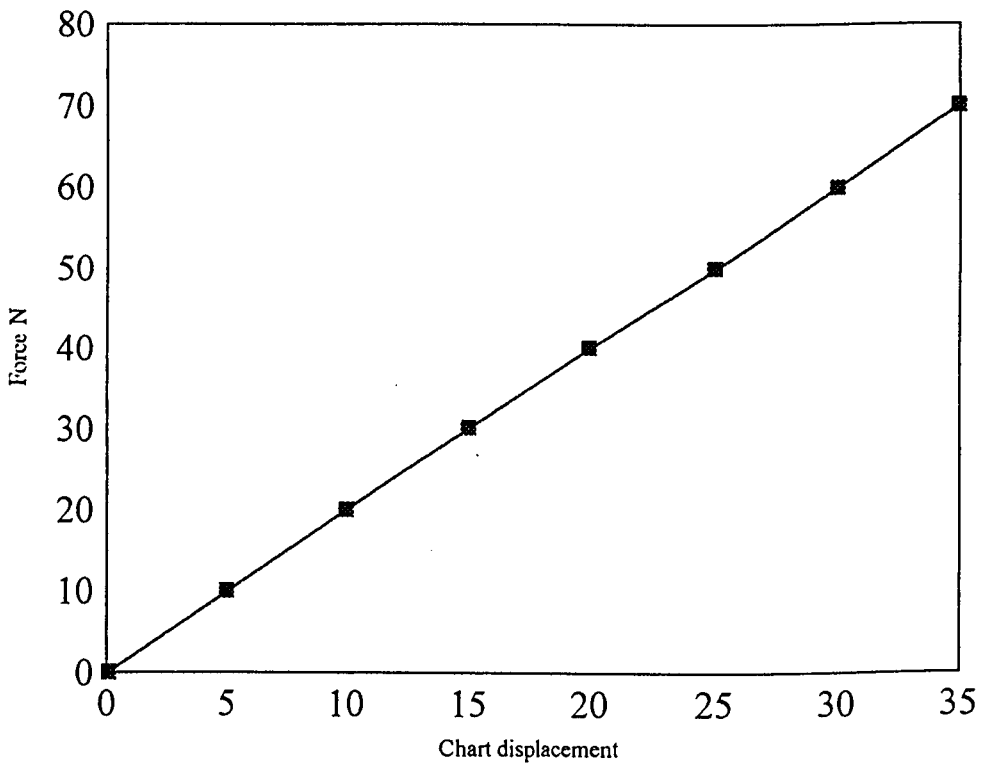


Figure 2.4 Calibration chart for the load cell

2.3 Temperature measurement

The surface temperature of the specimen was measured externally by an optical pyrometer sighted through a glass window. This pyrometer was able to measure temperatures in the range 700°-3000°C by focusing on the specimen surface and using the disappearing filament technique. A contact thermocouple was also used to calibrate the accuracy of the optical pyrometer and it was found that at 1100°C the variation was $\pm 25^{\circ}\text{C}$ (2.2%) for a number of different operators.

2.4 Preparation of specimen, impressors and sliders

◆ Specimens

Impression creep and sliding friction and wear experiments were carried out on materials which were originally manufactured by De Beers as tool inserts with flat parallel surfaces (rake face). Polycrystalline diamond materials i.e. Syndax (round), Syndite (rectangular), and CVDite (square) were supplied in the polished condition by De Beers. cBN materials (Amorite) were prepared and polished by a technique developed in this project as follows:

1. The flat cBN surface was mounted in a hard resin (Bakelite).
2. The mounted specimen was loaded onto a rotating SiC disc in order to remove the resin from the surface of the specimen.
3. It was then loaded onto a grooved ceramic platen hard disc (metlap10) with a rotational speed of 200 rpm. The platen was charged with 25 μm diamond

slurry and polished for 10 minutes. This time was sufficient to allow the grinding process to level the surface of the hard particles in the specimen.

4. Then a grooved iron composite platen hard disc, manufactured from a homogeneous mix of synthetic resins and metal particles* (metlap 4), rotating at 150 rpm and charged with 14 μ m diamond slurry, was used for 30 minutes. Then 6 μ m diamond slurry was added to the same disc and the speed was maintained for further 45 minutes.
5. For final polishing, a 1 μ m diamond paste was used with an aluminium disc, covered by hard and smooth polymeric cloth, rotating at 200rpm and for 45 minutes.

◆ Impressors

All the impressor and sliders were mechanically shaped and ground into a conical shape with an included angle of 120° (Figure 2.1). Before the specimen and indenter were loaded into the chamber for the test, all the greases and contaminants were removed by cleaning them ultrasonically in acetone for 15 minutes and then they were loaded carefully into the chamber. Also, the specimen was heated in the vacuum typically at 1000°C for 30 minutes, in order to remove the surface gases. Details are given in the appropriate chapter where, in particular cases, these cleaning conditions were varied.

For the impression creep experiments and the measurement of flow stress of Syndax, cubic boron nitride (Amborite) was used as an impressor. Similar measurements for Amborite were carried out with titanium diboride impressors.

* Kemet surface finishing manual, Dec 1993

A number of different ceramic and metallic sliders have been used for the sliding friction experiments e.g. (TiB₂, aluminium, ferrous alloy, titanium alloy and nickel alloy).

2.5 Sliding friction and wear experiments at room temperature

Amborite, Syndax, Syndite, CVDite and diamond were investigated under the action of reciprocating sliding friction. A group of metallic and ceramic materials were selected as sliders (initially cones shaped with 120° included angle). These materials were selected to provide a range of hardness from Hk₂₀₀ 1.1 GPa (aluminium) to Hk₂₀₀ 3.2 GPa (titanium alloy). The ceramic sliders were TiB₂ and cBN with Knoop hardness (Hk₅₀₀) of 13 and 38 GPa respectively.

The tests were carried out in the high temperature apparatus, in air and in vacuum. Some of the sliders with high melting point were selected for the tests at high temperature in order to develop sufficiently high pressures to initiate cracking and wear.

To remove the surface contaminants, before sliding, the specimen and the slider were cleaned ultrasonically in acetone for 15 minutes. The adsorbed surface gases on diamond, Syndax, CVDite and Amborite specimen were removed by heating them in vacuum for 30 minutes at 1000°C. However, a temperature of 700°C for 45 minutes was used for the Syndite specimen because of its thermal instability at higher temperatures.

The normal load used for the sliding friction and wear tests was 100N, the sliding speed was 0.1mm/sec and the length of each track was about 3mm.

When a slider was first loaded against a harder specimen surface, the tip was blunted by plastic flow and the resultant circular area of contact increased until it was sufficient to support the applied load elastically. By dividing the applied load by this contact area, an effective mean pressure (P_m), which is directly related to the indentation hardness of the material from which the cone is made, was determined. For metals, the effective mean pressure (P_m) is about one third of the indentation hardness of the slider (cone) materials i.e. $P_m = H/3$ (Brookes, Shaw and Tanner 1986). The apparent mean pressure was evaluated by dividing the applied load by the resulting contact area of the tip after the sliding process. The value of the apparent mean pressure was normally less than the effective mean pressure due to the increase in apparent contact area with sliding.

After the out-gassing of the specimen surface, the experiment was started by applying the load onto the cone to blunt its tip before sliding. The cone was then moved to another position and the friction force was measured over the first reciprocating traversal. When the coefficient of friction was low and there was no significant transfer of the slider material, further traversals were carried out. In those cases, continuous friction measurements were made for tracks of 10, 100, 1000 and 3500 traversals. The resultant tracks were examined using optical and scanning electron microscopy and dimensions were determined using Taylor-Hobson Talysurf Series 50. In this system the diamond stylus traversed the surface and the pick-up converts its vertical movement (caused through surface irregularities) into an electrical signal. This signal is amplified, processed to give various parameters, and the result output to a visual display or print out device.

Scanning electron microscopy (SEM) was carried out using the Cambridge Stereoscan 200 to observe the nature of deformation and wear. Whilst using the SEM, analyses was carried out with a Link QX2000 energy dispersive X-ray analyser.

2.6 Measurement of the volume of impressions

Two polycrystalline materials were selected for the creep impression experiments, cBN (Amorite) representing the polycrystalline cubic boron nitride materials and Syndax which was selected to represent the diamond based materials because it has the best thermal stability. All the creep impressions on both materials were performed using cubic boron nitride (Amorite) as the indenter. All the impressors were made from the same toolpiece materials.

Impressions were made for dwell times of 300s, 1000s, 1800s and 3000s for each temperature and an initially sharp impressor was used for each individual measurement. The selected experimental temperatures were 1000°C, 1250°C, 1450°C for Amorite and 850°C, 1000°C, 1200°C, and 1300°C for Syndax.

Measurement of the diameter of the contact areas was made by using a filar micrometer eyepiece on a Nikon Optiphot light microscope with an accuracy of better than 0.2µm.

In this study, the volumes and depths of the impressions on Amorite and Syndax specimens were obtained and evaluated using a system developed in this department based on the direct phase detecting interferometer (DPDI). As shown in Figure 2.5, this system consists of a double beam interference microscope connected to a stepper motor, a video camera and a video frame

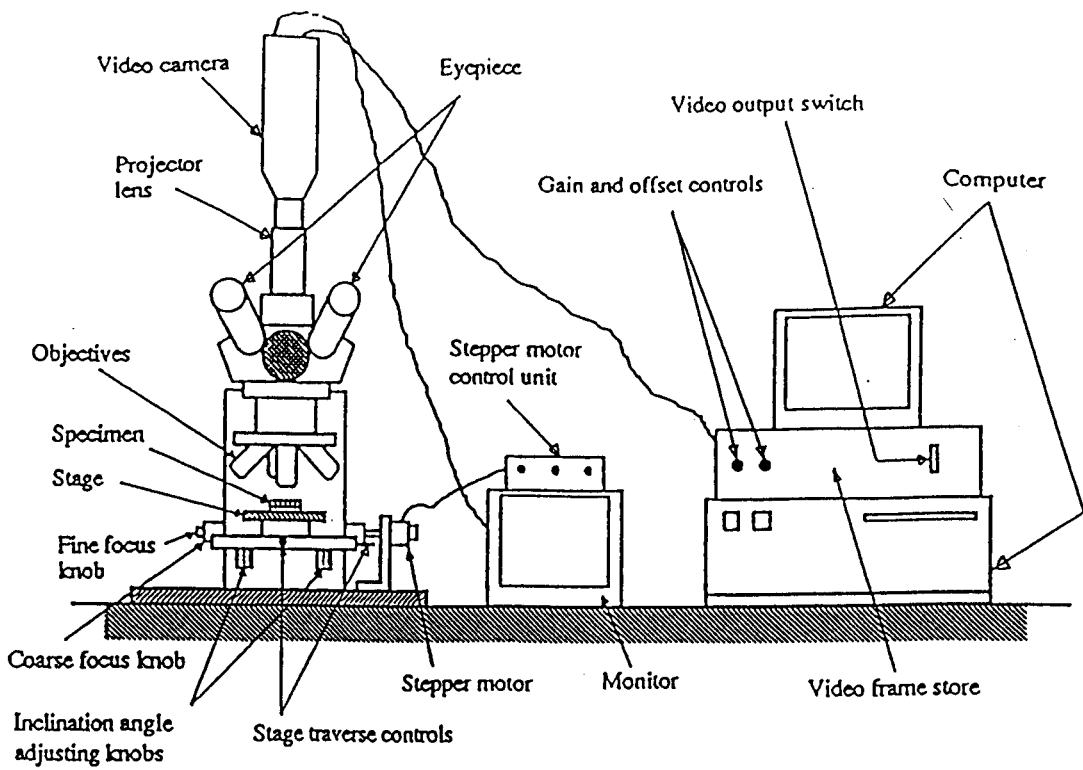


Figure 2.5 Direct phase detecting interferometer (DPDI)

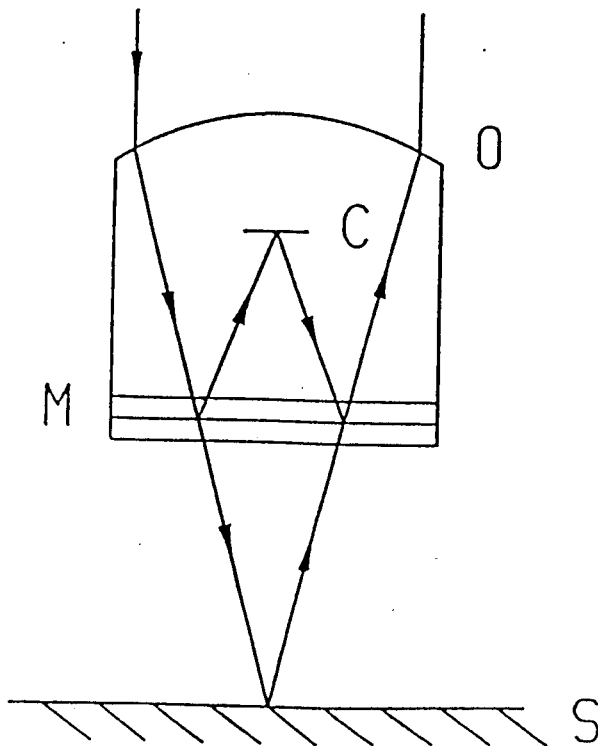


Figure 2.6 The principle of double beam interference

store (frame grabber) all of which are connected to a controlling computer. The specimen was mounted on a controllable stage which was tilted, through the adjusting knobs, until the surface of the specimen was normal to the optical path through the Mirau lens. To develop the interference fringes, the light emitted from a single source was passed through a beam splitter to produce two beams of light. After traversing different paths, the beams recombine to form destructive and constructive interference resulting in dark and light fringes on a screen. Each fringe represents a step change in contour.

In the specific application illustrated in Figure 2.6 the length of the optical path of the two beams is critical in obtaining the desired fringes. The single beam passes through objective (O) and the semi-transparent mirror (M). Part of the beam passes through the mirror and reflects off the specimen surface (S). The other part of the beam is reflected onto a plane mirror (C) which in turn reflects it to superpose the first beam arriving back from the specimen at (M). As a result of this superposition, circular fringes are produced when observing a circular impression. The difference in height between two consecutive similar fringes is half of one wavelength (λ) of light (273nm) since the path length difference is an integral number of wavelengths.

In this particular study, the materials which were investigated were all polycrystalline. Different grains and phases are discontinuous and have different reflectivity resulting in discontinuous fringes. Therefore, it was impossible to establish the order of the dark fringe using monochromatic light. Consequently, white light was used. Once an interferogram was obtained, the lens was focused on a point at the bottom of the impression. Usually this point represented the

small area of a truncated pyramid. From the video camera, which was mounted on the microscope, the frame grabber recorded that point taking it as a reference point. The areas delineated by segments of dark fringes allowed the area of contact to be estimated. Subsequently, the microscope stage was then moved by the stepper motor in steps of 4nm and new area was determined. This process was repeated until an overflow was reached, which indicated the spread of the fringes at the top of the impression level with the specimen surface. The evaluation of the depth of the impression is based on the number of fringes for each impression.

The volume of the impressions were calculated by using the formula which is valid for the truncated cone shown in Figure 2.7.

$$h_1 = \frac{r_1}{(r_2 - r_1)} dh$$

$$h_2 = \frac{r_2}{(r_2 - r_1)} dh$$

$$dv = \frac{1}{3} \pi r_2^2 h_2 - \frac{1}{3} \pi r_1^2 h_1 \Rightarrow dv = \frac{dh}{3} (A_1 + A_2 + \sqrt{A_1 A_2})$$

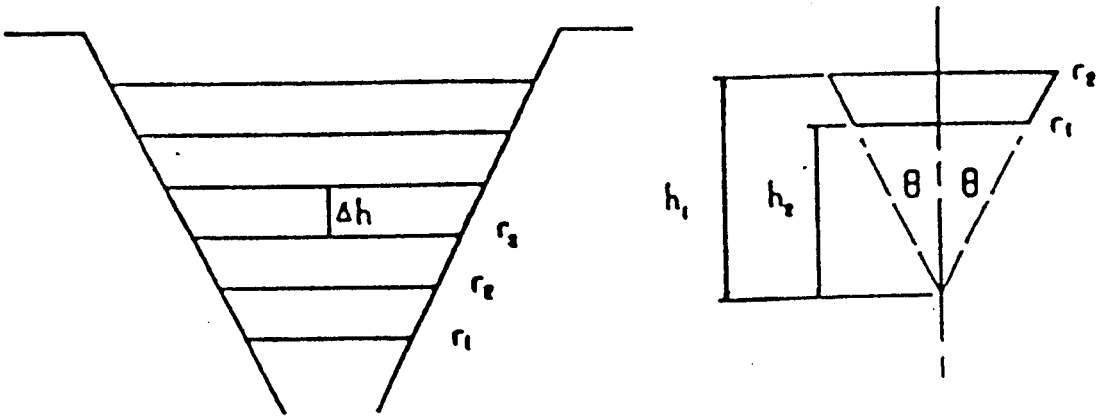


Figure 2.7: Truncated cone diagram to illustrate the method of volume calculation

Chapter 3 The effect of temperature on the flow stress of ultra-hard materials

3.1 Introduction

Many materials when stressed above a certain minimum stress, show permanent, non-recoverable or plastic deformation. This is the result of the displacement of atoms or groups of atoms from their original position in the lattice. That minimum stress is defined as the yield stress (σ_y). Continued plastic deformation or flow takes place when the effective flow stress exceeds the initial yield stress of the material. A flow stress therefore is the stress required to maintain plastic deformation, and is normally higher than the yield stress. An exception is the lower yield point as in the yield-drop phenomenon in materials such as silicon and germanium.

The plastic properties of materials are normally measured using standard uniaxial tension or compression techniques and the data is displayed as a load-elongation or a stress-strain curve. Figure 3.1 shows a typical schematic tensile stress-strain curve for a polycrystalline ductile metal. Following linear elastic deformation (where the strain is proportional to the stress and the deformation is reversible), plastic flow commences at a stress approximately equal to the tensile yield stress (σ_y , point A in the schematic). Following yielding, the material work hardens and the flow stress required to continue deformation increases with increasing strain, i.e. after initial yielding has occurred, plastic flow will continue either under a constant yield stress (e.g. for fully work-hardened materials or at high homologous temperatures, where, essentially, the flow stress is constant) or

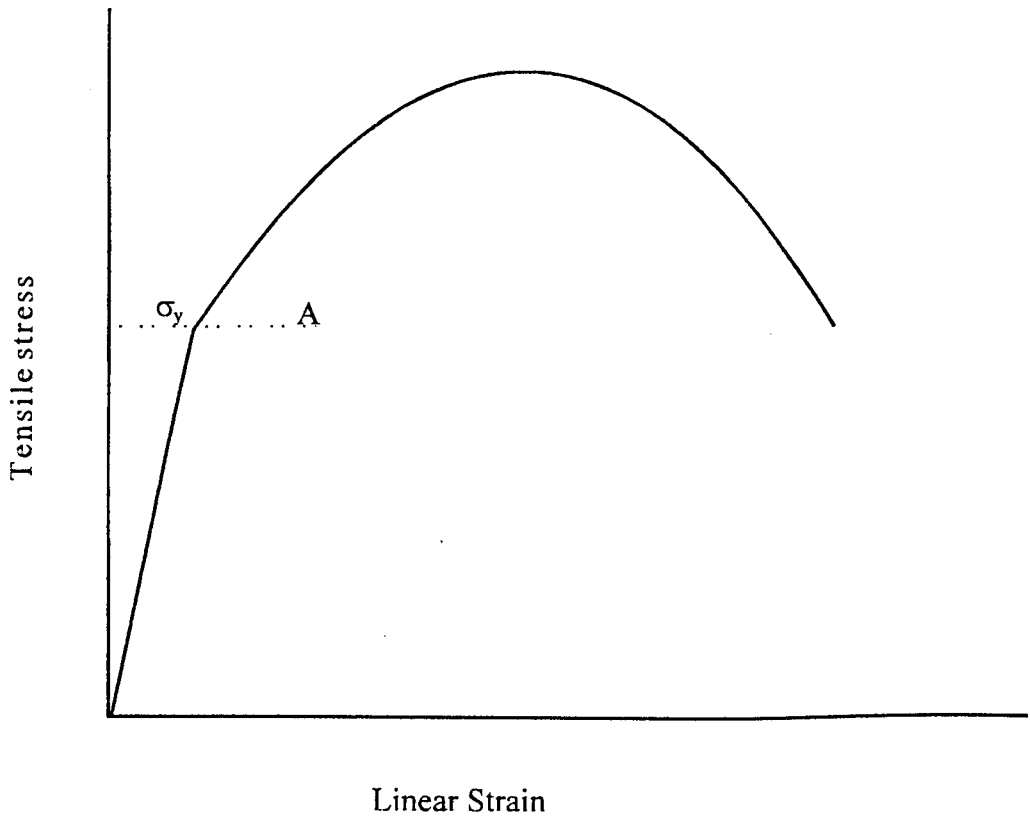


Figure 3.1 A schematic of tensile stress-strain curve

under an increasing flow stress. The main factor affecting the flow stress is work-hardening, (or strain hardening). Over a limited portion of the stress-strain curve i.e. from yield to the maximum tensile stress, the flow stress, σ_F , can be represented by the relationship:

$$\sigma_f = b\epsilon^n$$

where b is a constant, ϵ is its plastic strain and n is the work hardening index.

◆ Indentation plasticity

As mentioned in Chapter 1, the indentation hardness measurement of metals provides a convenient method of material testing, indicating the plastic properties of the material and enabling an estimated value of the yield stress (σ_y) to be obtained. It is of extreme value in investigating the mechanical properties of specimens which are too small to provide standard tensile or compression test specimens or materials which exhibit brittle behaviour. The stresses generated below an indentation form a core of hydrostatic pressure (which tends to inhibit fracture) and shear stresses (which cause plastic deformation outside the contact area). Many workers have attempted to relate the indentation hardness to the yield properties of the material. Tabor (1951) established that the Vickers hardness is a measurement of the flow stress in compression according to:

$$P = C\sigma_y$$

For fully workhardened, ductile polycrystalline materials, Tabor (1951) considered the ratio of the indentation pressure (hardness) to the uniaxial yield stress, σ_y , to be approximately 3 for the Vickers indenter:

$$P \cong 3\sigma_y$$

In this analysis it is assumed that the flow stress does not increase and that the applied pressure is uniform i.e. the effect of friction in the contact area between the indenter and the sample is ignored. However, to interpret the deformation of an annealed metal in terms of a plastic model, the increase in flow stress due to work-hardening must be taken into consideration. The work-hardening leads to the concept of a representative strain where the flow stress is related to its value. Tabor (1951, 1970) demonstrated that, for annealed metals, the hardness should be compared to the flow stress of the material at 8% strain (e.g. $\epsilon \cong 0.08$ for the Vickers pyramid) or:

$$P = 3 \sigma_{f(0.8)}$$

One of the observed features during the indentation of fully annealed metals is the tendency for the metal to be depressed around the indentation. This effect is known as 'sinking-in'. Alternatively, for highly work-hardened material, there is an upward extrusion of displaced metal so as to form a raised crater. This effect is known as 'piling-up'. However, neither effect alters the projected area of the indentation and hence the measured hardness is nearly equal to the actual applied pressure.

The above model of Tabor ignored elastic effects in the indentation process. The plastic strain in the zone beneath the indentation, over which the indentation pressure acts, diminishes with distance from the contact area until the plastic strain equals the elastic strain in the hinterland. This problem was analysed by Hill (1950) where he showed that the pressure P depends on the ratio of yield stress to elastic modulus:

$$\frac{P}{\sigma_y} = 0.4 + \frac{2}{3} \ln \frac{E}{\sigma_y}$$

Here he assumed that Poisson's ratio $\nu=0.5$.

Following the observation that there appeared to be a flow of material away from the indenters in some metals (Samuels & Mulhearn, 1957), Marsh (1964) suggested that this was due to elastic deformation of the hinterland and that the deformation beneath the indentation resembled the expansion of a hemi-spherical cavity into an elastic-plastic solid. For a Vickers indenter the results of Marsh followed the relation:

$$\frac{P}{\sigma_y} = 0.07 + 0.6 \ln \frac{E}{\sigma_y}$$

When E/σ_y is small (i.e. $\cong 10$), $P = 1.5\sigma_y$. This is a very elastic material which can accommodate the plastic strain and reduce the constraint on plastic flow, i.e. some polymers. When E/σ_y is large ($E/\sigma_y \cong 20$), $P=1.8\sigma_y$, i.e. for a glass. For values of E/σ_y above about 100, $P > 3\sigma_y$ - such as thought to be the case for the ultra-hard materials studied in this project.

According to Hill's original analysis, (1950) the elastic-plastic boundary is at a distance c from the centre of the contact area and the pressure in the expanding core is given by :

$$\frac{P}{\sigma_y} = \frac{2}{3} + 2 \ln \frac{c}{a}$$

where a is the radius of the impression.

Here the elastic-plastic core boundary coincided with the plastic core boundary, $c=a$, at $P = \frac{2}{3}\sigma_y$. Below this contact pressure the analysis is not valid.

For conical and pyramidal indenters of large apical angles, the plastic yield pressure depends on E/σ_y and the analysis of radial expansion of a hemispherical core is justified. For indenters with small apical angles the deformation mode is different i.e. it resembles that of a rigid plastic metal (Atkins *et al* 1966) in that material is pushed up along the sides of the indenters (i.e. pile-up). The analysis of Johnson (1970) describes the indentation process in terms of the semi-angle (θ) of the indenter or by the ratio of d/D of a spherical indenter, assuming that deformation along the elastic plastic boundary must accommodate the volume of material displaced by the indenter. Thus the equation of Hill becomes:

$$\frac{P}{\sigma_y} = \frac{2}{3} \left(1 + \ln \frac{E \cot \theta}{3\sigma_y} \right)$$

where $\cot \theta$ is replaced by d/D for spherical indenters.

In summary, under indentation conditions with rigid pyramids, the mean pressure (P) is between 1.5 to 3.0 times the representative flow stress (σ_f).

◆ Single crystals

A fully work-hardened polycrystalline material behaves as an isotropic plastic solid with a hardness approximately three times the uniaxial yield stress. The onset of plastic flow occurs at a point where the principal shear stress is the highest. An ideally plastic solid will not work-harden. In reality, a single crystal of the same material has a much lower yield stress, however this is not reflected in the difference in hardness values. This is due in part to the rapid

work-hardening rate of single crystals, but it is also related to the constraints imposed by the limited number of available slip systems around the indentation. Therefore a critical resolved shear stress (CRSS) criterion is required to determine the response of the various slip systems in the bulk of the single crystal under the applied load i.e. the stress to activate dislocation sources on the most favourably slip plane. For single crystals the hardness can be related to the resolved shear stress as:

$$H = C \times \text{CRSS}$$

where the constant C is dependent on the indenter geometry, orientation and the crystallography of the materials. For many ceramic single crystals the average between the hardness and the CRSS is of the order of 35 - compared to 100 for f.c.c. crystals and 3 for work-hardened polycrystalline metals.

The critical resolved shear stress is normally evaluated from stress-strain curves derived from standard uniaxial tension or compression tests or bending experiments. These methods are well adapted for metallic materials and ionic single crystals such as MgO. Covalent ceramic single crystals generally display a threshold brittle-ductile transition temperature referred to as B-D-T, above which dislocation motion and extensive plastic deformation, as opposed to brittle fracture, becomes the predominant deformation mode. At lower temperatures the measurement of the plastic properties of ceramics by these methods is difficult due to their tendency to brittle failure - this is especially true for diamond. The B-D-T temperature for diamond was first identified by Evans and Wild, (1965) as 1870K ($\cong 0.45 T_m$) where T_m is the melting point in K. In this work the brittle-ductile transition temperature was evaluated by the three point

bending technique and during those experiments there was no sign of plastic deformation below that temperature. However, more recent research (Brookes, 1992) has demonstrated that plastic flow occurs at much lower temperatures (750°-1100°C) - i.e. those which are likely to be developed during some metal cutting processes.

Standard indentation hardness techniques, based on rigid indenters such as Knoop or Vickers, do not allow the evaluation of the critical resolved shear stress. Furthermore, the stress concentration is very high at the tip of the indenter, giving rise to high levels of strain and fracture will dominate the deformation - especially in materials such as diamond. In fact, indentations in diamond invariably produce cracks even at the highest experimental temperatures.

3.2 Soft impression technique

The soft impression technique has been developed by Brookes and co-workers, (1987, 1990) to evaluate, among other things, the critical resolved shear stress in diamond and other ceramic materials. In this technique, the contact stress applied by a softer cone is less than the hardness of the impressed material and is determined by the hardness of the impressor. The choice of different materials as impressors, gives the opportunity to change the applied contact pressure and therefore the level of deformation and strain.

One of the most important features of the soft impression technique is that the resolved shear stresses developed in the crystal, beneath the contact area, are

sufficient to initiate dislocation movement (provided the contact pressure is sufficient to exceed the CRSS) whilst the tensile stresses in the surface are insufficient to develop cracks. By using impressors from different materials with hardnesses much less than that of diamond, Brookes and co-workers showed that mechanisms of plastic deformation in diamond could be investigated.

Brookes and Green (1972) first demonstrated that the harder surface of magnesium oxide (MgO) can be plastically deformed during both static indentation and sliding by replacing a conventional indenter with a copper cone. Subsequent serial polishing of the MgO confirmed that the extent of the dislocation movement beneath the softer copper cones was comparable to that beneath a rigid diamond indenter. In later work on the (001) surface of MgO, Brookes *et al* (1987) compared the dislocation behaviour in response to a range of impressors made from different materials. They demonstrated that, under the same experimental conditions the configuration beneath a copper cone was comparable with that of a steel cone even though the mean contact pressures were 0.7 GPa and 4.5 GPa respectively. The density of the dislocations within that constant volume, and therefore the effective, average or representative strain, increased with the hardness of the impressor until at a certain level cracks were initiated (Shaw and Brookes 1989).

Brookes *et al* (1987) and Shaw and Brookes (1989) have also shown that, under lubricated conditions, the repeated sliding contact between a hard ceramic surface and softer metallic sliders can also increase the effective strain leading to work hardening, fatigue and fragmentation of the hard crystal surface.

As the normal load is applied to a conical shaped soft impressor, the initial sharp tip of the softer impressor is flattened by plastic flow, increasing the blunt contact area, until it is sufficient to support the applied load elastically. The mean contact pressure (P_m) is determined by the normal load divided by the apparent contact area (Figure 3.2). This mean contact pressure is approximately one third of the indentation hardness of the fully work hardened metallic impressor materials (Shaw and Brookes 1989). By controlling the magnitude of the resultant mean pressure (P_m), the minimum contact mean pressure, which is only just sufficient to move a few dislocations on the active slip system of single crystals, can be determined. This results in an approximate estimation of the critical resolved shear stress of that particular crystal. Impressors made from materials with greater hardness will produce higher levels of mean pressure and hence will move an increasing number of dislocations producing a higher level of strain within the dislocated zone beneath the impressor.

Brookes *et al* (1991) utilised this technique when they proposed an alternative method for determining the threshold level of mean pressure to produce plastic flow. In this method an aluminium cone was used to apply a range of contact pressures at a given normal load. The range of pressure was realised by allowing the aluminium cone tip to creep over an extended dwell time, increasing the area of contact and hence reducing the mean contact pressure. With time, P_m decreased until a certain point where the mean pressure was then too low to initiate any further dislocation movement. This minimum mean pressure was assumed to be the mean pressure necessary to initiate slip and using the relationship $P_m=3\tau_c$ resulted in an estimation of the CRSS.

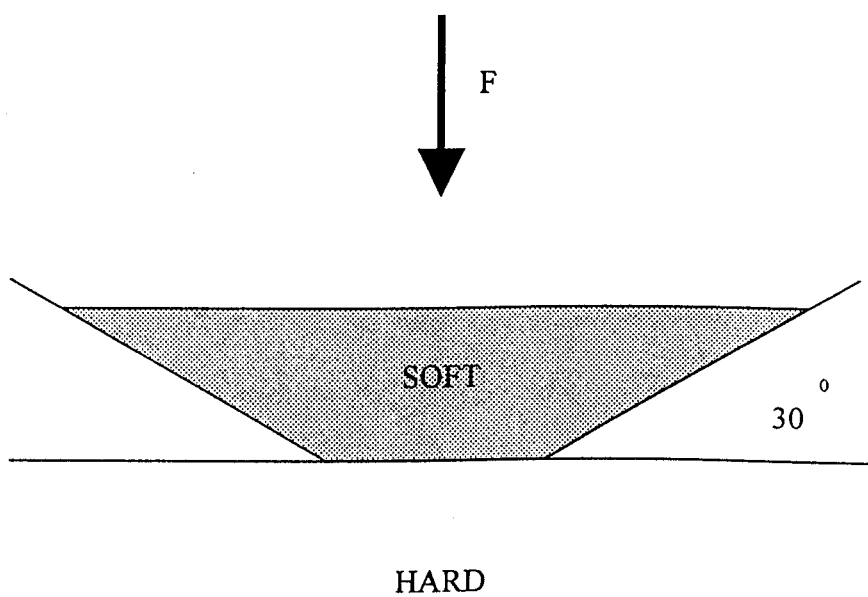


Figure 3.2 The soft impressor technique

The soft impression technique was used successfully to evaluate the critical resolved shear stress of materials such as MgO where a suitable dislocation etchant is available and the onset of dislocation mobility can be readily verified. Although this technique has proven to be applicable to diamond, plastic deformation was monitored by the observation of visible slip steps on the deformed surface because no suitable dislocation etchant was available for diamond. This leads to an estimate of the critical resolved shear stress in diamond which is somewhat higher than the actual value.

Furthermore it has been observed that the dislocated volume developed beneath both conventional rigid and soft indenters increases with dwell time so as to preserve geometrical similarity. With a continuous increase in the size of the flattened tip, and therefore a continuously decreasing mean pressure, the average level of plastic strain in the dislocated volume decreases. It was shown that this impression creep process continues whilst the mean pressure exceeds the threshold pressure for the hard crystal. This type of behaviour was verified for single crystals of both MgO and diamond (Brookes *et al* 1991).

3.2.1 Modelling of the soft impression technique

An analysis of the stress field of a uniformly loaded circular contact was originally made by Love (1929). This model was extended to analyse the anisotropy in Ge and GaAs (Hirsch *et al* 1985) and MgO (Roberts *et al* 1988), the hardness polarity in GaAs, (Roberts *et al* 1986) and the plastic behaviour of diamond (Brookes *et al* 1990). Essentially the model, developed by Roberts, resolves the stresses onto the available slip systems.

◆ **The Roberts model for $\{111\}\langle 110\rangle$ slip systems**

The Roberts model for circular and uniform contact on a (001) surface of a crystal with $\{111\}\langle 110\rangle$ slip systems, such as diamond, is shown in Figure 3.3. This figure represents sections taken normal to the deformed surface and passing through the centre of contact. The sections are divided by broken lines into regions where different slip systems are the most highly stressed. The slip systems are labelled as shown on the slip plane pyramids. Roberts applied a simple convention for the labelling of slip planes where the positive side of the slip plane is always upwards with respect to the deformed surface and the negative sense is always downwards. Therefore, a positive sense of RSS indicating shear is such that the top side of the slip plane will slip into the crystal and a negative sense will indicate that the underside of the slip plane will slip into the crystal. The negative value of the resolved shear stress is indicated by those numbers with a bar sign over them. The contours shown are of the highest resolved shear stress, expressed in units of $P_m \times 10^{-3}$, irrespective of the slip system. In figure 3.3 (a) in the (100) section, the peak is at $x = 0.58a$, $z = -0.54a$, with a $RSS = 0.316P_m$. In Figure 3.3(b) the maximum stress in the $(\bar{1}\bar{1}0)$ section is at $x = 0.52a$, $z = 0.5a$, with a $RSS = 0.3P_m$ (P_m is the applied pressure). The resolved shear stress values directly under the contact area are low, $<0.15P_m$ and the only slip systems not stressed in the region are those with their slip direction parallel to the surface. The slip systems with the highest RSS values are those on inclined slip planes of the convergent type (i.e. 11 and 12 in the Figure 3.3 (b). Outside the contact area, slip systems with slip vectors parallel to the surface

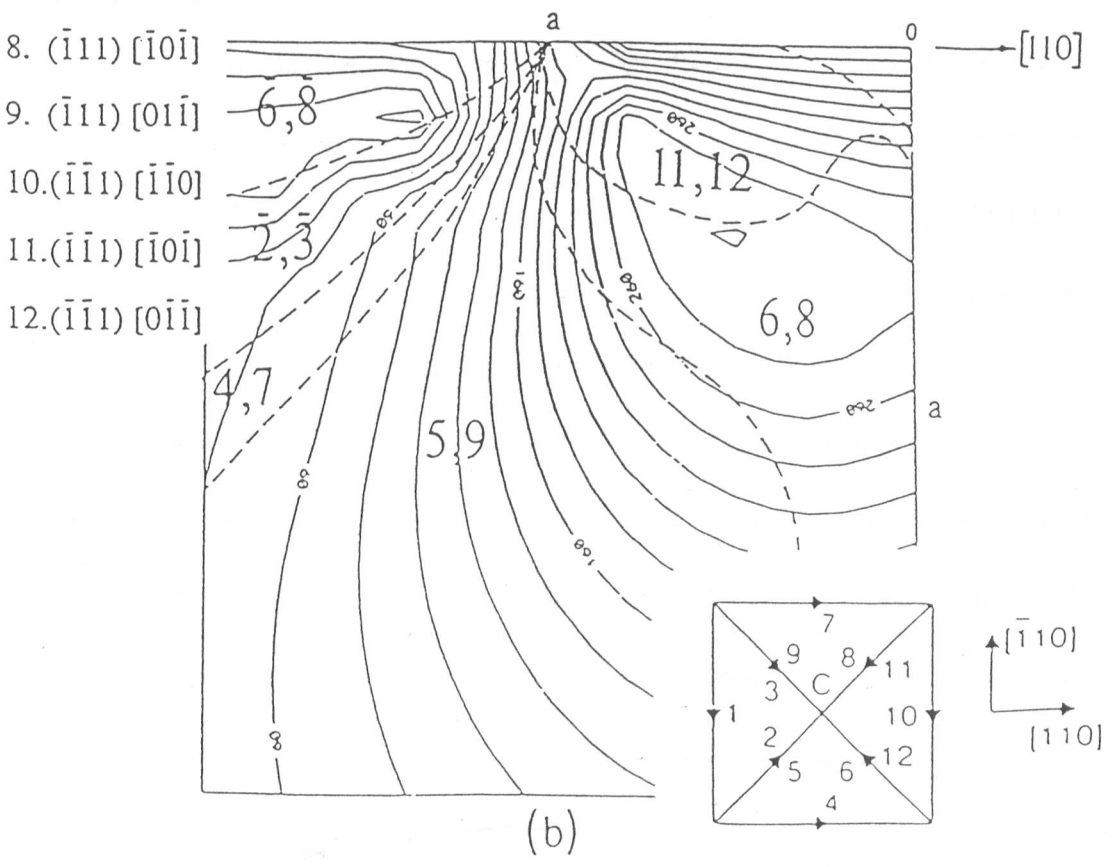
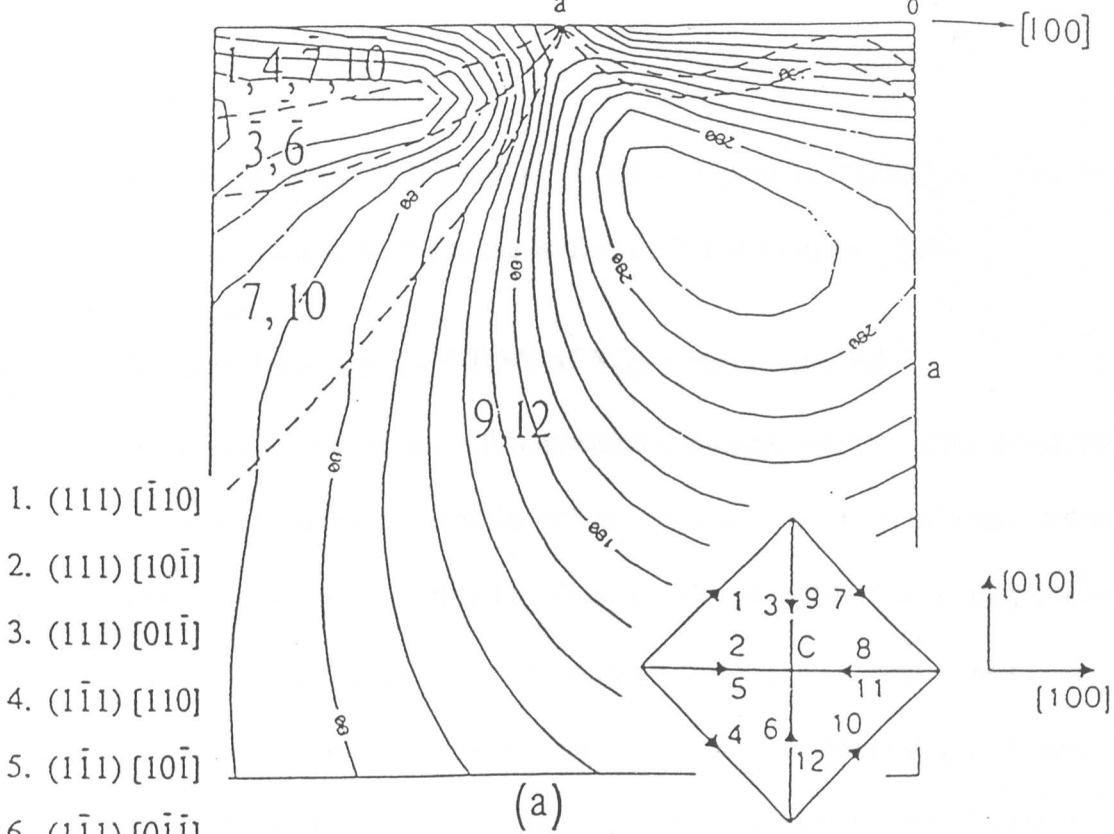


Figure 3.3: Resolved shear stress contours for crystals with $\{111\}\langle 110\rangle$ systems
 (a) (100) section
 (b) $(\bar{1}\bar{1}0)$ section

have the highest RSS at depth i.e. 7 and 10 Figure 3.3 (a) and divergent planes have the highest RSS near to the surface i.e. 3 and 6 Figure 3.3 (b).

3.3 Determining the CRSS of MgO and diamond

The investigations of the soft impression technique resulted in the development of two methods to evaluate the critical resolved shear stress of brittle materials. The first method was outlined by Shaw and Brookes (1989) when they employed a range of metallic impressors to evaluate the threshold mean pressure (P_m) to move a few dislocations on the active slip system in MgO single crystals. The critical resolved shear stress was estimated according to that threshold mean pressure using the relationship $P_m = 3\tau_c$. In that work it was established that the degree to which the cone flattened under the load was inversely proportional to the nominal hardness of the impressor material. After using a dislocation etchant to reveal the configuration and density of the dislocations produced by each sharp metallic cone in the magnesium oxide, it was found that the cadmium impressor had generated the lowest dislocation density and it was assumed that the minimum mean pressure to initiate dislocations in MgO was close to that developed by cadmium. Dislocations were consistently produced by all of the harder materials used i.e. zinc, aluminium, copper, brass and steel. The dislocations developed by all the metallic cones, except the steel cone, were restricted to a small number of discrete $\{110\}_{45}$ planes, all inclined at 45° to the (001) surface, and directly below the contact area, with no region of high dislocation density. The steel indenter had also induced slip on $\{110\}_{90}$ in addition to slip on the $\{110\}_{45}$ planes. However the dislocations on the $\{110\}_{90}$ slip planes did not penetrate into the crystal to the same depth as dislocations on

the $\{110\}_{45}$ slip planes. In addition it was found that the dislocations developed beneath the contact area were not dependent on the hardness of the cone material i.e. the mean contact pressure developed, but that the extent of the dislocation movement was determined by the normal load. The threshold mean pressure developed by cadmium was 0.17 GPa, giving a critical resolved shear stress of 0.06 GPa. This value was calculated based on the Roberts model (section 3.2.1) which predicts a maximum resolved shear stress of $0.35 P_m$ for a (001) surface with $\{110\} \langle 110 \rangle$ slip system with the maximum located at 0.33 of the radius of the contact area beneath the surface (Brookes 1992). The CRSS value determined by Shaw and Brookes using this method was in agreement with that of Groves and Kelly (1963) when they evaluated the CRSS of MgO by applying the uniaxial compression test and measured a CRSS value of between 0.049 and 0.069 GPa.

An alternative method to determine the minimum contact mean pressure required to move dislocations, was developed by exploiting the creep properties of the cone material. Brookes *et al* (1991) have investigated this possibility, using the (001) surfaces of MgO, through monitoring the increase in contact area with loading time on a pure aluminium cone. In those experiments, a normal load of 1kgf was applied onto the hard surface for a dwell time of 300 seconds. This initial stage developed a mean pressure of 0.25 GPa. When the cone was removed and reloaded on to a new position on the specimen, a fresh set of dislocations were produced over the new contact area which was enlarged due to the creep of the aluminium cone. In this second impression the mean pressure was reduced to 0.2 GPa. Following a dwell time of 10^5 seconds, a contact

pressure of 0.15 GPa developed and the dislocated region stopped expanding. When this particular flattened cone was reloaded in a new undeformed region no dislocations were evident in the new contact region. This was an indication that the threshold mean pressure to initiate dislocation movement in MgO at room temperature was between 0.2 and 0.15 GPa in agreement with the value of 0.17 GPa evaluated earlier by the first method by Shaw and Brookes (1989).

This later technique was utilised by Brookes (1992) to determine the critical resolved shear stress of three types of diamond i.e. Ib, Ia and IIa diamonds as a function of temperature. In addition, the brittle to ductile temperature was established for each type. In that work, impressions were made in all three types of diamond in the temperature range of 20° to 1600°C, using cones made from cBN, Si₃N₄, TiB₂, TiC and Ir. Although the Knoop hardness of cBN is considered high (32 GPa) compared with all materials, it is considerably softer than diamond (70 GPa). It was found that between room temperature and 450°C, the contact pressure developed by the cubic boron nitride cones on (001) surfaces of all the diamond types decreased from about 20 to 11 GPa. Spiral ring cracking was produced, with no evidence of slip lines. Above 450°C, the cracks disappeared, and no macroscopic evidence of dislocation movement was found. The minimum temperature at which visible slip lines were observed was 770°C in type Ib synthetic diamond using a cBN cone with a mean pressure of 12 GPa. This temperature is the temperature at which dislocations start to move and multiply and is referred to as the brittle-ductile transition temperature (BDT). Under these experimental conditions this BDT was established as 950°C for type Ia diamond with a minimum mean pressure of 9.5 GPa and 1100°C for type IIa

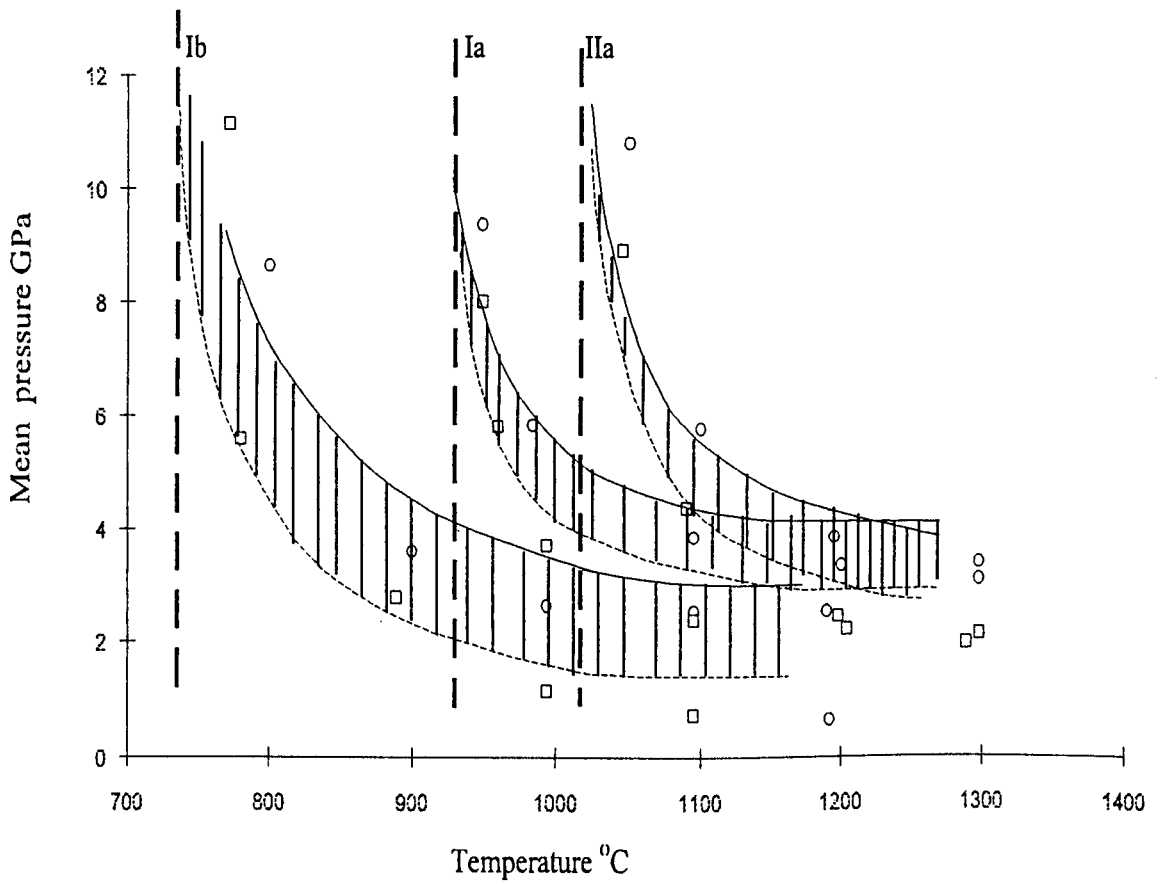


Figure 3.4 The effect of temperature on the flow stress of different types of diamond and showing the relevant BDT temperatures

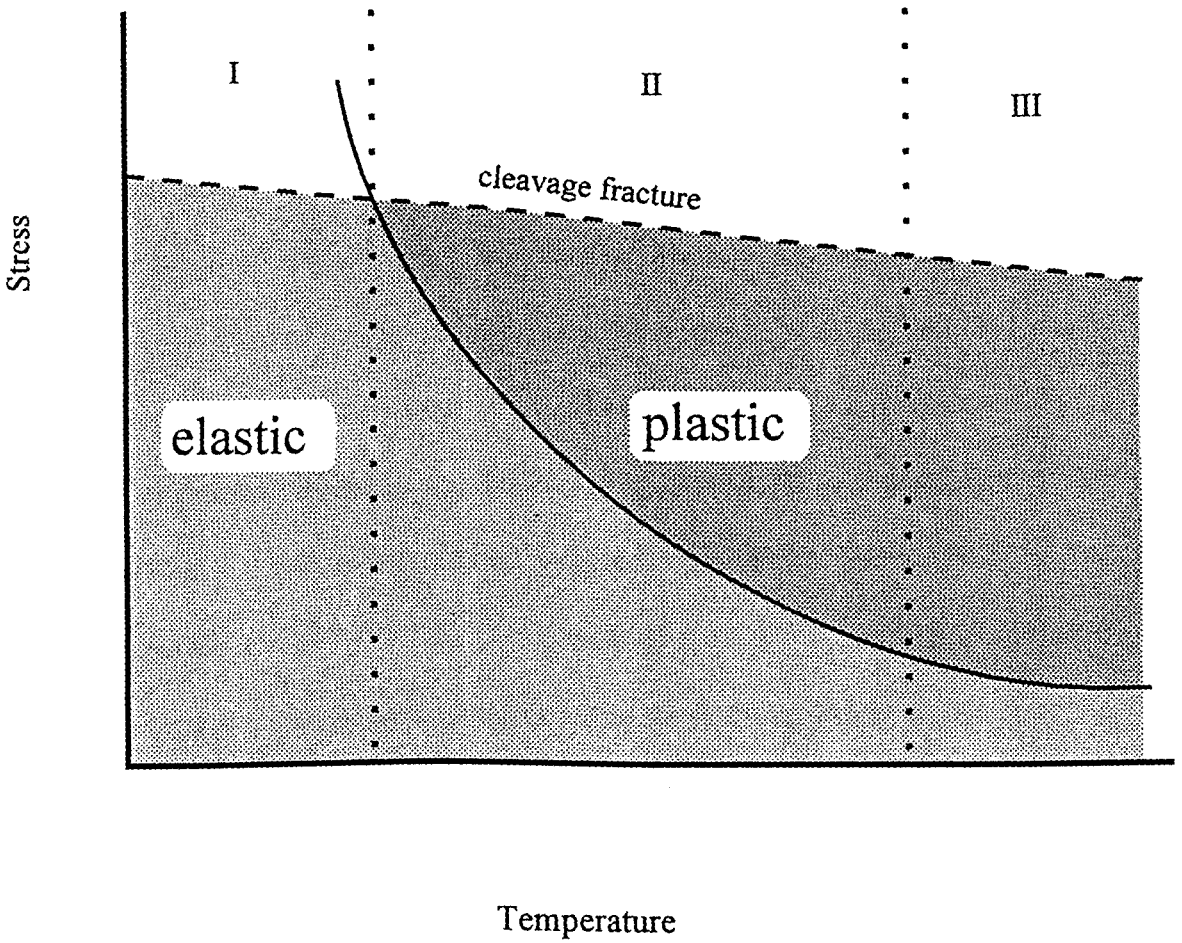


Figure 3.5 Schematic diagram showing the effect of temperature on the deformation of covalent crystals

diamond with a minimum mean pressure of 5.5 GPa (Figure 3.4). Cones made from other ceramic materials also initiated plastic deformation in diamond. The effect of temperature on the flow stress of diamond at high temperatures is summarised in the schematic diagram in Figure 3.5. This schematic shows the temperature at which the pressure required to start to move and multiply dislocations becomes less than that to cause cleavage fracture. Below the brittle to ductile transition temperature (regime I) the deformation is elastic: brittle and fracture occurs above a given P_m . In (regime II) it was found that the mobility of dislocations is such that time dependent plastic flow occurs, impression creep, and cracking is not on the cleavage planes but tends to be along the $\{110\}$ planes as a result of dislocation interactions. Here the flow stress decreases sharply as the temperature rises. In regime (III), the flow stress is independent of the temperature. The mean contact pressure to initiate plastic flow in the temperature range 700°-1400°C was evaluated for the three types of diamond. Using these measurements of minimum mean pressure in conjunction with the Roberts model the critical resolved shear stress was estimated for three types of diamond I_a, I_b and II_a. A summary of the evaluated critical resolved shear stress data is shown in Table 3.1 (Brookes 1992).

Table 3.1 Estimates of the critical resolved shear stress (GPa) between 700 and 1400°C.

°C	Type Ib	Type Ia	Type IIa
770	3.8		
950	1.3-2.4	3.0	
1000	0.32-1.3	2.3-2.5	
1100	0.32-1.3	0.64-1.6	1.60-3.7
1200	0.32	0.32-1.0	0.95-2.56
1300	0.32	0.32	0.64-1.44
1400	0.32	0.32	0.32-1.3

3.4 The application of the soft impression technique to measure the minimum contact mean pressure to plastically deform polycrystalline materials

In this work the application of the soft impressor technique has been extended to determine the flow stress of ultra-hard polycrystalline materials as a function of temperature. The justification of this determination is based on measurement of the minimum contact mean pressure to plastically deform polycrystalline copper correlated with its measured yield strength in tension. The selection of polycrystalline copper material to justify this technique was based on: **firstly**, the availability of large samples of copper for conventional tension test and the ability to machine it to the required shape; **secondly**, the plastic deformation (grain boundary and slip within each grain) around the impression on copper could be traced easily by optical and electron microscopes (Figure 3.7 and 3.8); **thirdly**, the ease of measurement and a high degree of reliability; **finally**, the difficulty to shape and deform ultra-hard polycrystalline materials at room temperature.

However, since polycrystalline materials are isotropic, the Roberts' model for single crystals (section 3.2.1) which has been verified for MgO and diamond is not applicable for the determination of maximum shear stress of polycrystalline materials. Therefore, a model has been developed to predict the behaviour of polycrystalline materials under a soft circular contact. As with the Roberts model, the required analysis was based on Love's work (1929), since all the

conditions of Love's model are satisfied in the experimental technique used in this work.

Once the model was developed and verified for the results obtained for the polycrystalline copper sample, it was applied to two ultra-hard materials; namely polycrystalline diamond (Syndax) and polycrystalline cubic boron nitride (Amorite).

3.4.1 Evaluation of the minimum contact mean pressure to plastically deform polycrystalline copper

Using the apparatus described in Chapter 2, a 120° cone of aluminium was loaded on a lubricated and polished copper surface (at room temperature and load of 100N) for five minutes. It was then reloaded in another position for the same time. The blunted tip increased in size, with increased dwell time, due to the creep of aluminium and hence the mean contact pressure correspondingly decreased. This procedure was repeated using the same cone in different positions on the copper sample until a minimum contact pressure was observed just sufficient to create an impression with minimal signs of plastic deformation around it. This process has been explained schematically in Figure 3.6. Here, the area of contact has increased with increased dwell time, and the density of the plastic deformation decreased with the decrease in mean pressure (blunting of the cone). R_1 represents the first impression which has high contact pressure and hence very dense signs of plasticity around the impression. R_5 represents the last impression, with minimum mean pressure and minimum plasticity.

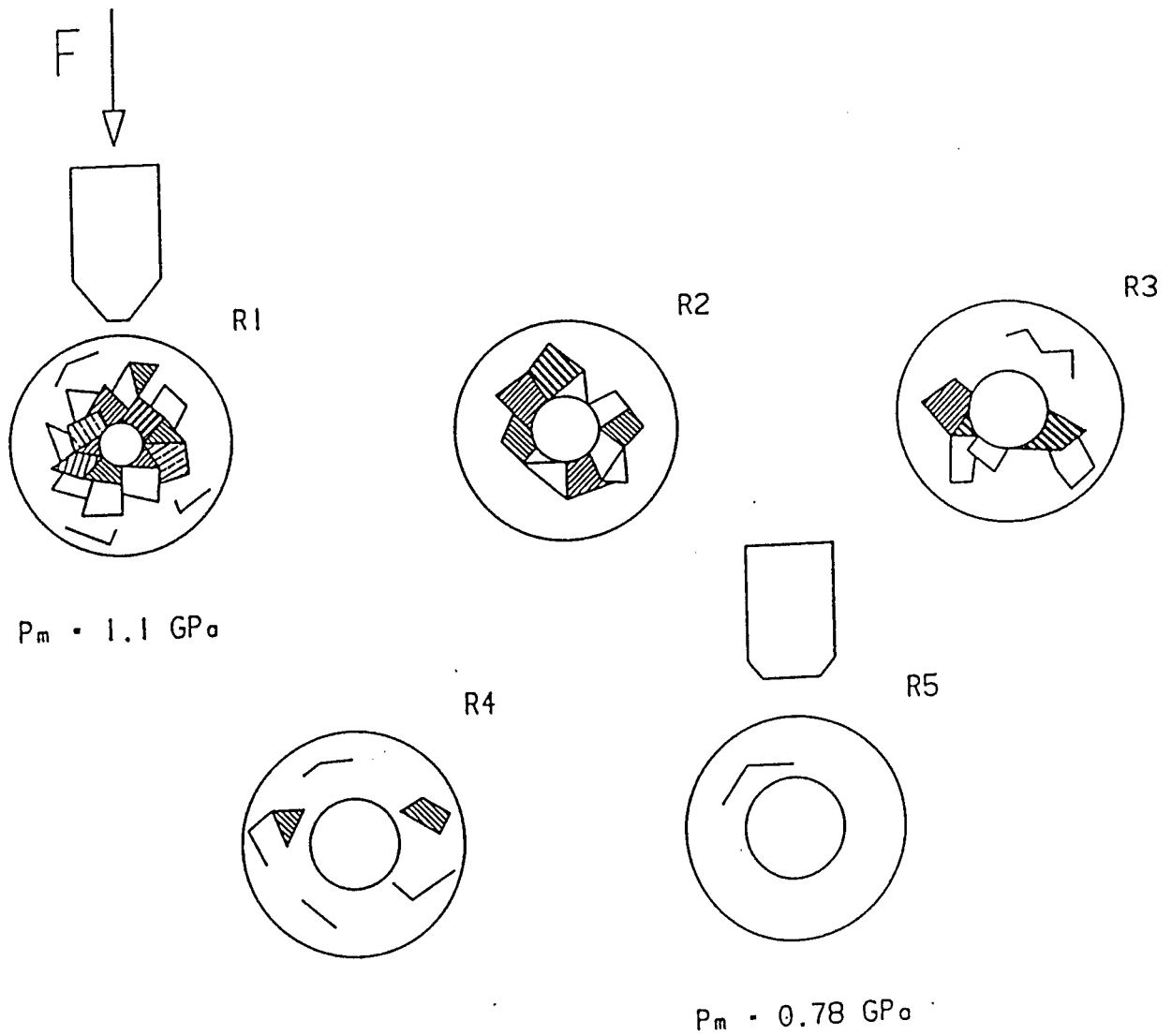
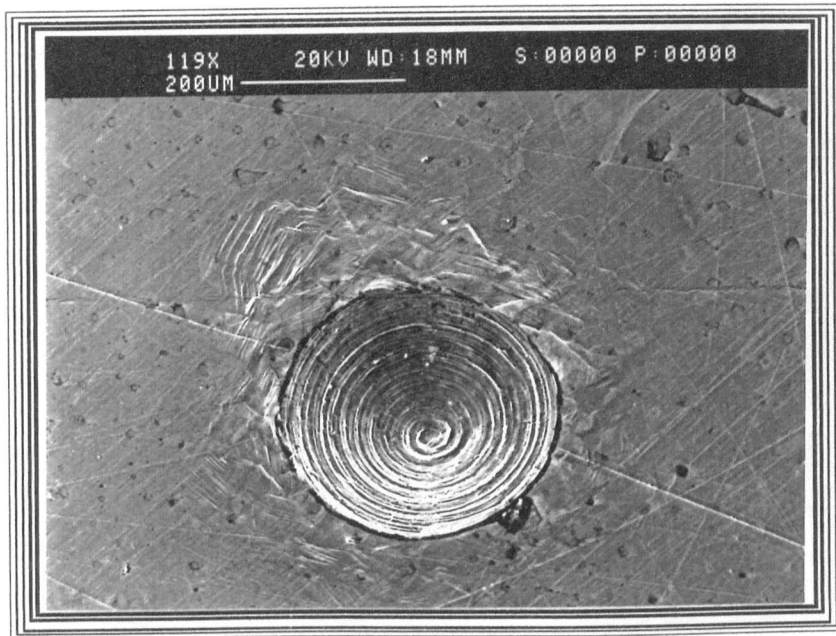


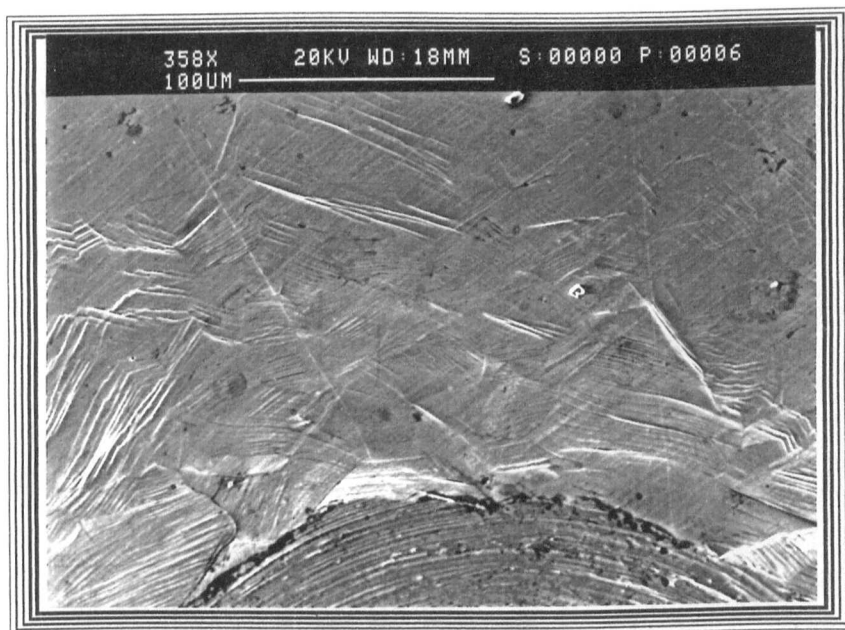
Figure 3.6 Schematic drawings to show the extent of plastic deformation decreases with decreasing contact pressure (blunting of the cone)

R1= First impression- gross plasticity

R5= Last impression- minimum plasticity



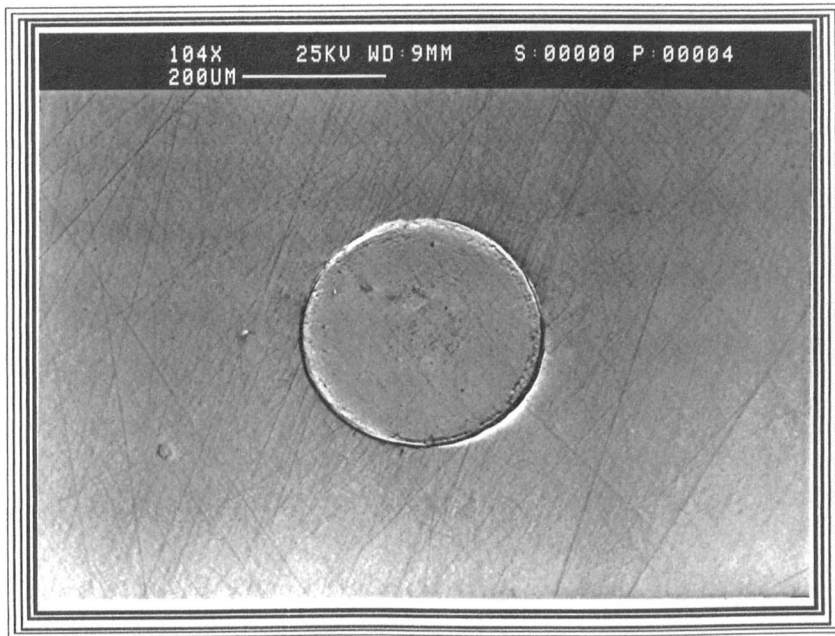
(a)



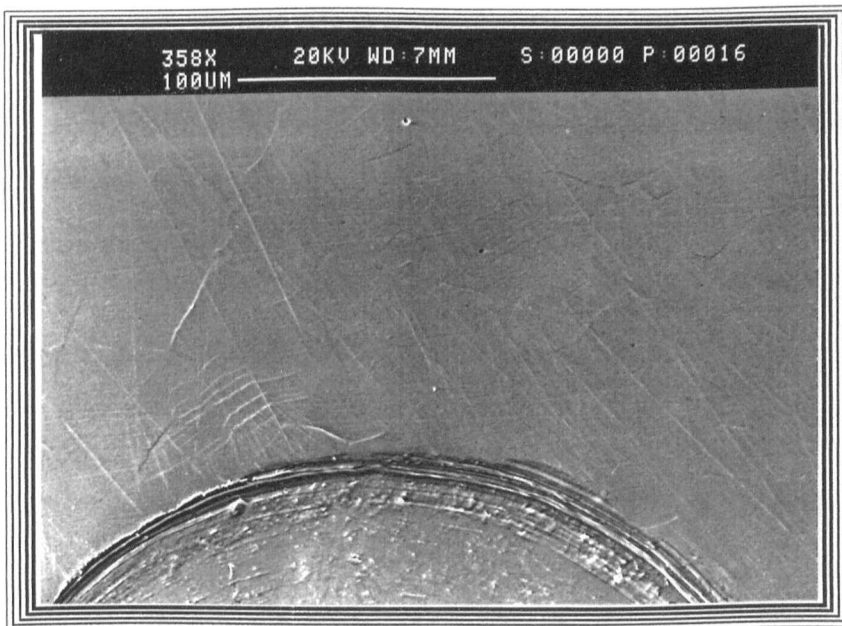
(b)

Figure 3.7 SEM micrograph of:

- (a) Impression made by sharp Al impressor on the copper sample
- (b) Section of (a) showing the extent of the plastic deformation



(a)



(b)

Figure 3.8 SEM micrograph of:

- (a) Impression made by blunt Al impressor on the copper sample
- (b) Section of (a) showing the extent of the plastic deformation

The micrographs in Figure 3.7 (a,b) and Figure 3.8 (a,b) show, in contrast, the first impression with the sharp indenter (R_1 in the schematic) and the last impression (R_5) when the contact mean pressure was just sufficient to deform the specimen plastically. Figure 3.7 (a) shows an impression made by a sharp aluminium cone on the copper sample and Figure 3.7 (b) shows a part of that impression with higher magnification to highlight the extent of plasticity (slip lines and grain boundaries). On the other hand, Figure 3.8 (a) shows an impression made by a blunt aluminium cone. The signs of plasticity were minimal, as shown in Figure 3.8 (b).

The minimum contact mean pressure at which visible plastic deformation was observed was 0.78 GPa. This value has been achieved by dividing the load (100N) by the area of contact of the last impression on the copper sample which was $= 1.28 \times 10^{-7} \text{m}^2$ (where the diameter of that impression = 0.404 mm). This compares with the mean contact pressure developed in the first impression (initially sharp cone) of 1.10 GPa and a Knoop hardness of 1.2 GPa (Table 3.2). In this method the minimum mean pressure using an aluminium cone was achieved by permitting the indenter to deform due to creep processes. However, to decrease the required dwell time to achieve the minimum mean pressure (P_m), an alternative method for producing a flat indenter with an increased contact area (and thus a reduced contact mean pressure) was to flatten the indenter by loading it on a harder surface like brass or steel with a higher load. By using both of these methods a comparable value of the minimum mean pressure (P_m) was obtained. A cone with a tip flattened to a larger contact area developed a mean

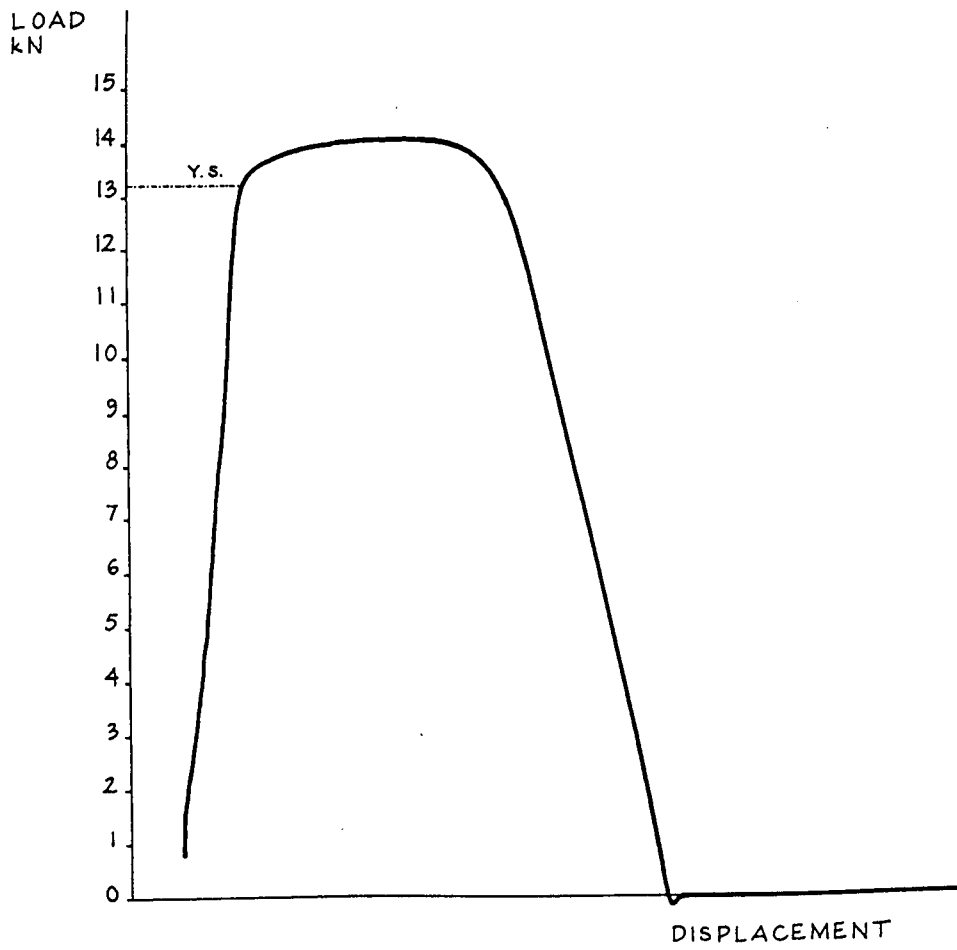


Figure 3.9 The standard tensile test on the copper sample
($\sigma_y = 0.258 \text{ GPa}$)

contact pressure of 0.56 GPa, but this was found to be too low to produce any visible plastic deformation.

The yield stress (σ_y), was evaluated for this copper sample by the standard tension test. The load:displacement curve is shown in Figure 3.9. Onset of plasticity occurred at 13.3 KN giving a value for the yield stress of 0.26 GPa.

Considering the schematic in Figure 3.10, which represents the uniaxial tension test, the shear stress can be related to the yield stress. By analysing this system in its equilibrium state, the vertical and horizontal forces can be written as:-

- Vertically:

$$\begin{aligned} T &= (F_n + F_s) \cos 45 \\ &= \frac{1}{\sqrt{2}} (F_n + F_s) \end{aligned}$$

Where F_n and F_s are (respectively) the normal and shear(parallel) forces acting on the area A' .

- Horizontally

$$F_n - F_s = 0 \Rightarrow F_n = F_s$$

Therefore:-

$$T = \frac{2}{\sqrt{2}} F_s = \sqrt{2} F_s$$

The shear stress τ on the surface A' is:

$$\tau = \frac{F_s}{A'}$$

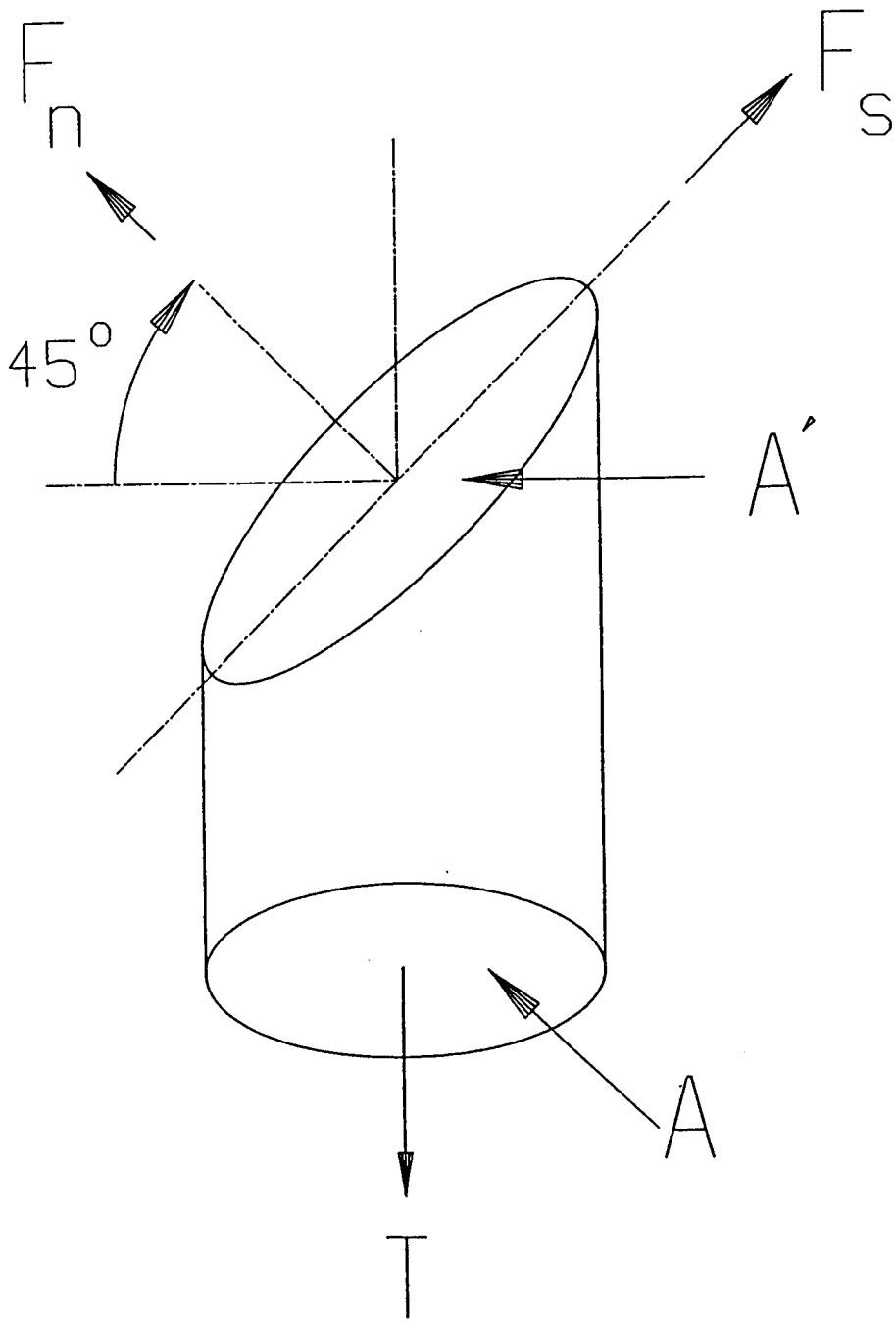


Figure 3.10: Schematic representation of the uniaxial tension test

$$= \frac{T}{\sqrt{2} A}$$

$$= \frac{T}{\sqrt{2}\sqrt{2} A}$$

This equation gives:

$$\tau = \frac{1}{2} \frac{T}{A}$$

$$= \frac{1}{2} \sigma$$

Where σ is the tensile stress on the cross sectional area A.

According to this relation the maximum shear stress for copper where $\sigma_y=0.26$ GPa, is:

$$S_{\max} = \frac{1}{2} \times 0.26 = 0.13 \text{ GPa}$$

The experimental results for copper are summarised in Table 3.2

Table 3.2 The experimental results of copper

Knoop hardness of copper	1.20 GPa
Minimum contact pressure(P_m)	0.78 GPa
Tensile yield strength	0.26 GPa

3.4.2 Modelling of the maximum shear stress(S_{\max})

Love (1929) calculated the stresses in a semi-infinite elastic and isotropic solid, due to uniform pressure, over a circular area on its plane surface. These

calculations were based on certain conditions which can be summarised as follows:

- i) The solid was elastic and isotropic.
- ii) A semi-infinite solid, with a plane surface.
- iii) The applied pressure was uniform over the contact area.

The experimental procedure and the material selected all satisfied these conditions as follows:

- 1) Polycrystalline copper material is an elastic and isotropic solid.
- 2) The copper samples were cylindrical in shape, 10mm in cross-section, length 20mm and the impression diameter was always less than 300 μ m. Taking the ratio of the impression to the sample diameter, this solid was considered as semi-infinite.
- 3) The applied pressure was uniform. Initially the aluminium impressor was a sharp cone, with 120° included angle and a Knoop hardness of 1.1 GPa. By reloading the impressor, the contact tip increased in diameter due to the plastic flow (creep) of aluminium and hence the contact area increased. Plastic flow spreads the impressor material uniformly (replicating the surface of the impressed material) and hence the applied pressure was uniform.

Taking the co-ordinate system (r, θ, z) shown in Figure 3.11, the stress components evaluated by Love (1929), due to a uniform pressure P applied over a circle of radius a , on its plane surface are given in the form of the following integrals:

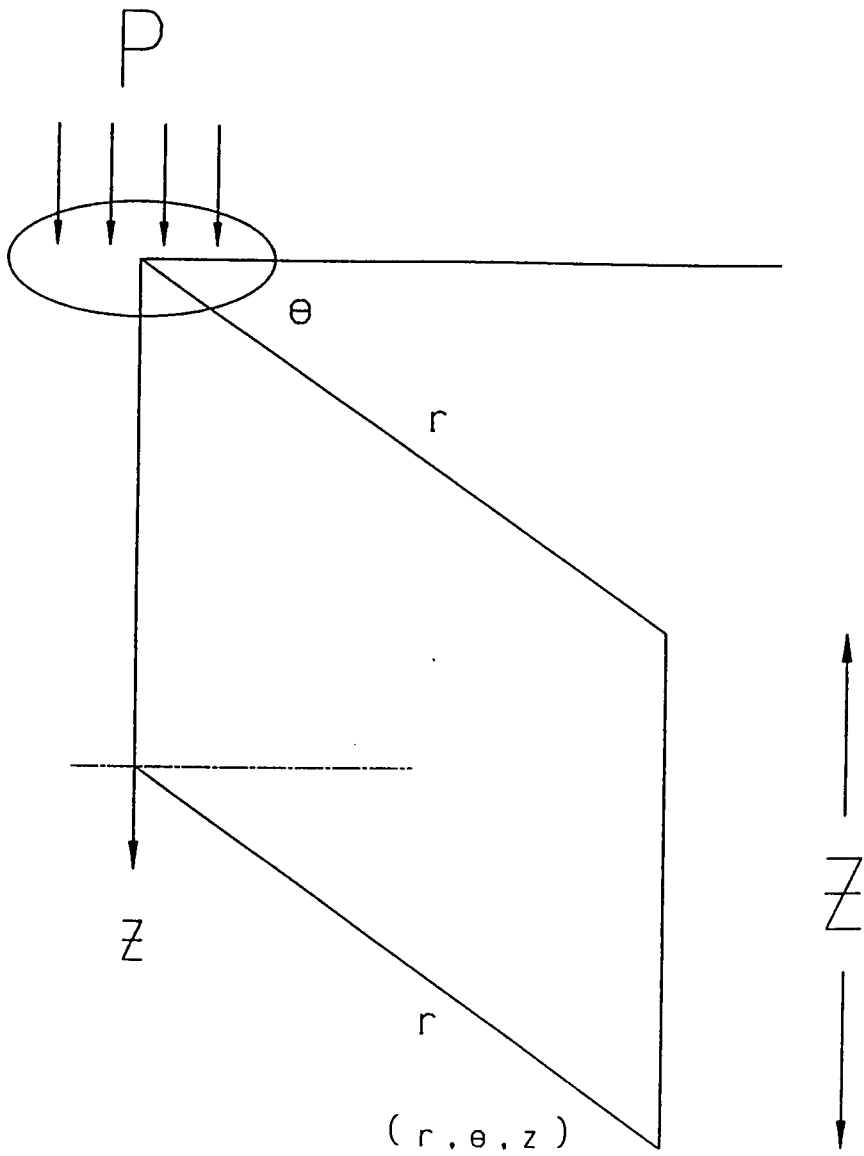


Figure 3.11 The co-ordinate system

$$\left. \begin{aligned}
 \sigma_r &= \frac{P}{2\pi} \{S_1 - 2\nu S_2 + ZS_3\} \\
 \sigma_\theta &= \frac{P}{2\pi} \{2\nu S_1 - S_2 + ZS_4\} \\
 \sigma_z &= \frac{P}{2\pi} \{S_1 - S_2 + ZS_5\} \\
 \tau_{rz} &= -\frac{Z^2 P}{2\pi} S_6
 \end{aligned} \right\} \quad (3.1)$$

where

$$S_1 = \int_0^{2\pi} \frac{(\rho - \cos\phi) \cos\phi}{R(Z + R)} d\phi$$

$$S_2 = \int_0^{2\pi} \frac{\sin^2 \phi}{R(Z + R)} d\phi$$

$$S_3 = \int_0^{2\pi} \frac{(\cos\phi - \rho) \cos\phi}{R^3} d\phi$$

$$S_4 = \int_0^{2\pi} \frac{\sin^2 \phi}{R^3} d\phi$$

$$S_5 = \int_0^{2\pi} \frac{(\rho \cos\phi - 1)}{R^3} d\phi$$

$$S_6 = \int_0^{2\pi} \frac{\cos\phi}{R^3} d\phi$$

with $\rho = \frac{r}{a}$, $Z = \frac{z}{a}$ and $R^2 = \rho^2 + Z^2 + 1 - 2\rho \cos\phi$

For general values of ρ and Z the integrals have to be evaluated by applying a numerical technique. However on the surface when $Z=0$ or on the axis of symmetry when $\rho=0$ the integrals could be solved exactly.

1) On the surface when Z=0

When Z=0 the stress components (3.1) could be rewritten as:

$$\left. \begin{aligned} \sigma_r &= \frac{P}{2\pi} \{S_1 - 2\nu S_2\} \\ \sigma_\theta &= \frac{P}{2\pi} \{2\nu S_1 - S_2\} \\ \sigma_z &= \frac{P}{2\pi} \{S_1 - S_2\} \\ \tau_{rz} &= 0 \end{aligned} \right\} \quad (3.2)$$

where

$$S_1 = \int_0^{2\pi} \frac{(\rho - \cos\phi) \cos\phi}{\rho^2 - 1 - 2\rho \cos\phi} d\phi$$

$$S_2 = \int_0^{2\pi} \frac{\sin^2 \phi}{\rho^2 - 1 - 2\rho \cos\phi} d\phi$$

These can be calculated exactly by analytical methods.

For $0 < \rho < 1$ the exact values of the integrals are:

$$S_1 = -\pi \quad \text{and} \quad S_2 = \pi$$

Substituting in (3.2) the values of stress components

become:

$$\left. \begin{aligned} \sigma_r &= -P \frac{(1+2\nu)}{2} \\ \sigma_\theta &= -P \frac{(1+2\nu)}{2} \\ \sigma_z &= -P \\ \tau_{rz} &= 0 \end{aligned} \right\} \quad (3.3)$$

And for $\rho > 1$ (outside the contact area), the values of the integrals are:-

$$S_1 = \frac{\pi}{\rho^2} \text{ and } S_2 = \frac{\pi}{\rho^2}.$$

Substituting in (3.2) the values of stress components are:

$$\left. \begin{aligned} \sigma_r &= P \frac{(1-2\nu)}{2\rho^2} \\ \sigma_\theta &= -P \frac{(1-2\nu)}{2\rho^2} \\ \sigma_z &= 0 \\ \tau_{rz} &= 0 \end{aligned} \right\} \quad (3.4)$$

The co-ordinate axes (r, θ, z) are principal axes because $\tau_{rz} = \tau_{r\theta} = \tau_{z\theta} = 0$ and hence the principal stresses on the surface are σ_r, σ_θ and σ_z . The maximum shear stress acts on the 45° planes to the principal axes, and hence the limiting shears are:

$$\frac{1}{2} |(\sigma_r - \sigma_\theta)|, \frac{1}{2} |(\sigma_\theta - \sigma_z)|, \frac{1}{2} |(\sigma_z - \sigma_r)| \quad (3.5)$$

By substituting the value of the stresses evaluated above in (3.5), the limiting shear values were derived as follows:

where $0 < \rho < 1$, the limiting shear values were derived by substituting the stresses from (3.3) in (3.5) as:

$$0, \frac{1}{4}(1-2\nu), \frac{1}{4}(1-2\nu) \quad (3.6)$$

and where $1 < \rho$, the limiting shear values were derived by substituting the stresses from (3.4) in (3.5):

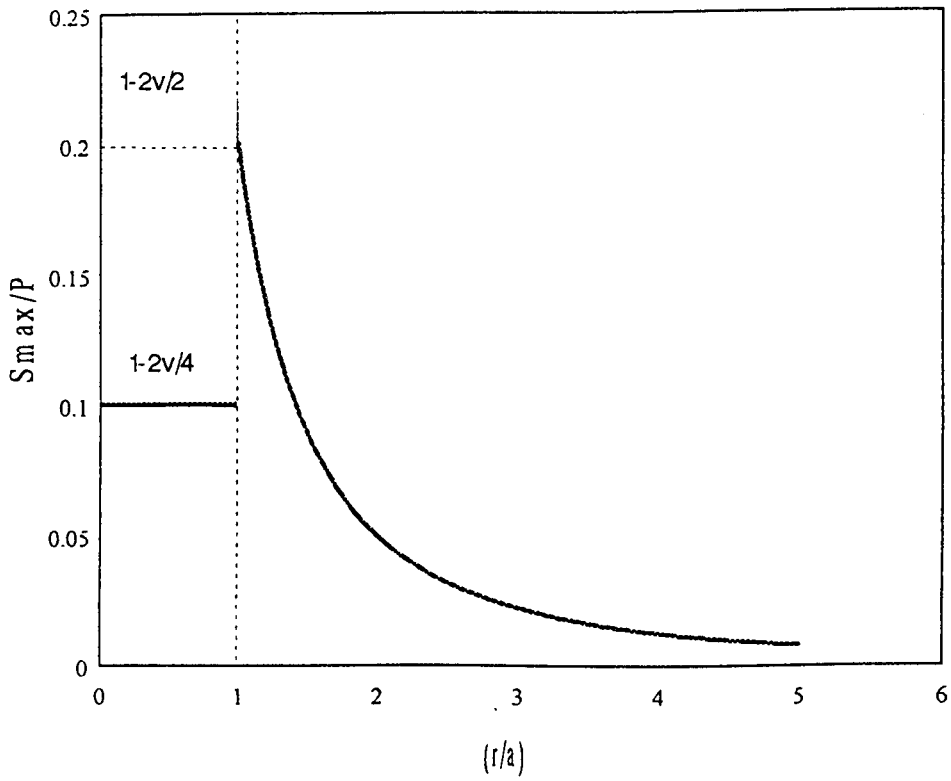


Figure 3.12 Maximum shear stress on the surface
Poisson's ratio = 0.3

$$\frac{1}{2\rho^2}(1-2\nu), \frac{1}{4\rho^2}(1-2\nu), \frac{1}{4\rho^2}(1-2\nu) \quad (3.7)$$

Therefore the ratio of the maximum shear S_{\max} to the pressure derived in (3.6) and (3.7) can be summarised:

$$\text{for } 0 < \rho < 1 \quad \frac{S_{\max}}{P} = \frac{1}{4}(1-2\nu) \quad (3.8)$$

$$\text{and for } \rho > 1 \quad \frac{S_{\max}}{P} = \frac{(1-2\nu)}{2\rho^2} \quad (3.9)$$

On the surface, the maximum shear stress can be evaluated by using the above relations i.e. (3.8) and (3.9). Using this analysis, the highest value of maximum shear stress was found to be $\frac{1-2\nu}{2}$ when $\rho=1$. This is shown in the graph presented in Figure (3.12).

2) On the axis when $\rho=0$

On the axis of symmetry, when $\rho=0$, the integrals have been evaluated exactly as follows:

$$S_1 = \int_0^{2\pi} \frac{-\cos^2 \theta}{R(R+Z)} d\theta = \frac{-\pi}{R(R+Z)}$$

$$S_2 = \int_0^{2\pi} \frac{\sin^2 \theta}{R(R+Z)} d\theta = \frac{\pi}{R(R+Z)}$$

$$S_3 = \int_0^{2\pi} \frac{\cos^2 \theta}{R^3} d\theta = \frac{\pi}{R^3}$$

$$S_4 = \int_0^{2\pi} \frac{\sin^2 \theta}{R^3} d\theta = \frac{\pi}{R^3}$$

$$S_5 = \int_0^{2\pi} \frac{d\theta}{R^3} = \frac{-2\pi}{R^3}$$

$$S_6 = \int_0^{2\pi} \frac{\cos\theta}{R^3} d\theta = 0$$

where

$$R^2 = 1 + Z^2$$

Substituting the values of these integrals in the stress components (3.1) then:

$$\begin{aligned} \sigma_r &= \frac{P}{2} \left[\frac{Z}{R^3} - \frac{(1+2\nu)}{R(R+Z)} \right] \\ \sigma_\theta &= \frac{P}{2} \left[\frac{Z}{R^3} - \frac{(1+2\nu)}{R(R+Z)} \right] \\ \sigma_z &= -P \left[\frac{Z}{R^3} - \frac{1}{R(R+Z)} \right] \\ \tau_{rz} &= 0 \end{aligned} \tag{3.10}$$

The co-ordinate axes (r, θ, z) are principal axes because $\tau_{rz} = \tau_{r\theta} = \tau_{z\theta} = 0$ so that the above relations represent the principal stresses. Substituting in (3.5), the limiting shears on the axis are as follow:

$$\begin{aligned} \frac{1}{2} |(\sigma_r - \sigma_\theta)| &= 0 \\ \frac{1}{2} |(\sigma_\theta - \sigma_z)| &= \frac{3Z}{4R^3} + \frac{1-2\nu}{4R(R+Z)} \\ \frac{1}{2} |(\sigma_z - \sigma_r)| &= \frac{3Z}{4R^3} + \frac{1-2\nu}{4R(R+Z)} \end{aligned}$$

i.e. on the axis $\frac{S_{\max}}{P}$ is $f(Z)$:

$$\frac{S_{\max}}{P} = f(Z) = \frac{3Z}{4R^3} + \frac{1-2\nu}{4R(R+Z)} \quad (3.11)$$

where $R^2 = 1 + Z^2$

The position of the largest maximum shear stress on the axis occurs when

$$\frac{df}{dz} = 0, \text{ i.e. when } Z^2 = \frac{2(1+\nu)}{7-2\nu} \quad (3.12)$$

Taking Poisson's Ratio as $\nu = 0.3$ the largest value of $\frac{S_{\max}}{P}$ is 0.333 and occurs at the point $Z = 0.64$.

From the above, the maximum shear stress was calculated exactly on the surface ($Z = 0$) and on the axis ($\rho = 0$). These were the special cases. However, to establish the maximum shear stresses beneath the contact area i.e. for general values for Z and ρ , the integrals were calculated by applying a standard numerical method, Simpson's rule.

The resolved values of $(\frac{S_{\max}}{P})$ for the volume beneath the contact area were computed and are displayed as contours in Figure 3.13. This Figure shows the developed model for a uniformly loaded circular contact on a polycrystalline copper surface taking Poisson's ratio of 0.3. This represents the elastic deformation of an isotropic polycrystalline material by a uniformly loaded flat impressor. Using this analysis, it can be seen that the maximum shear stress in the bulk of the material is developed just beneath the surface and very close to the edge of the contact area.

According to the model reported by Tabor (1951) for elastic deformation of a flat surface of metal by a **sphere**, the maximum value of shear stress occurs at a

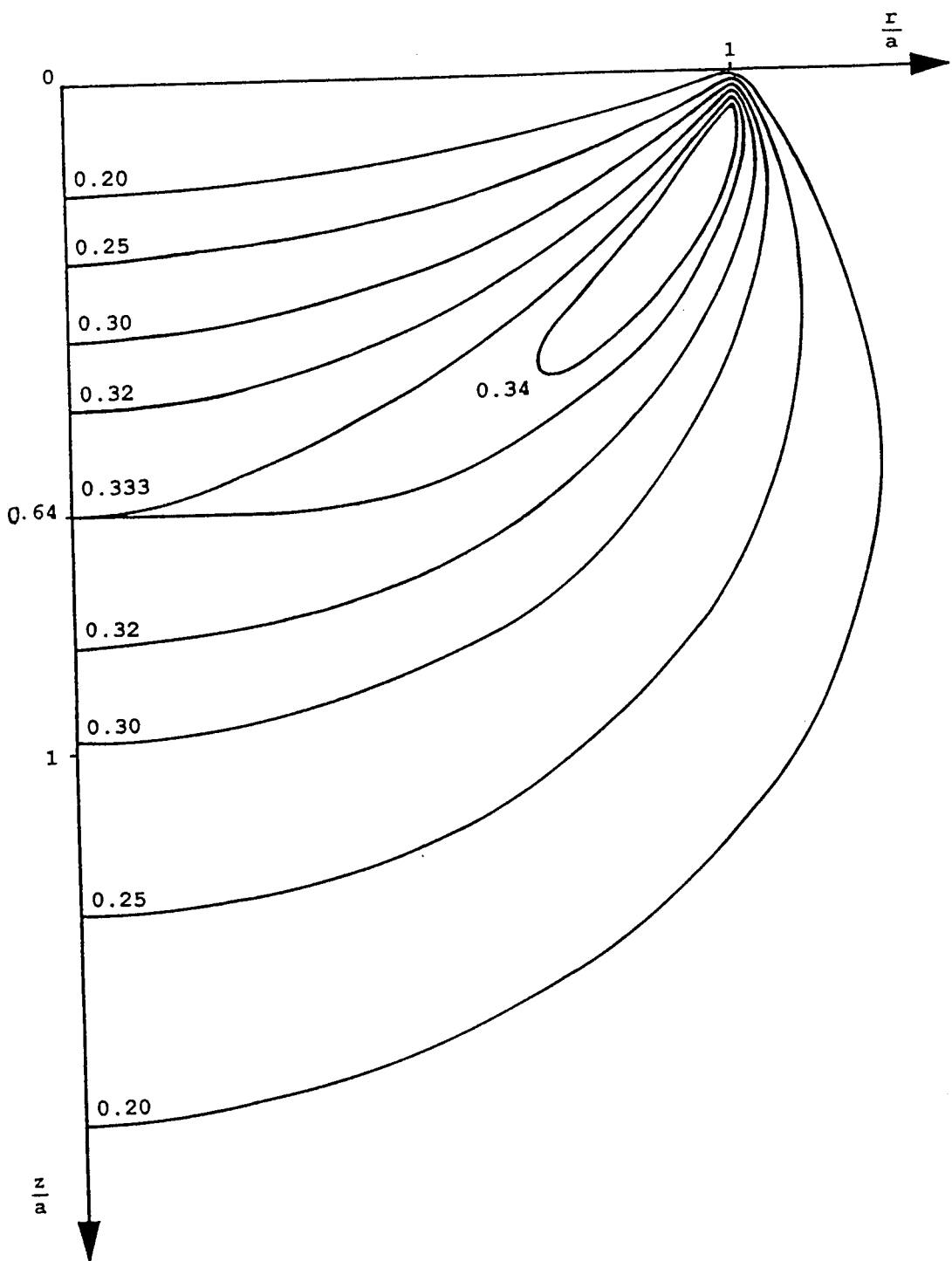


Figure 3.13 Contours of equal maximums (S_{\max}/P) for copper (Poisson's ratio (ν) = 0.3)

point about $0.5a$ below the centre of contact (where a is the radius of the contact area). This implies that plastic flow will occur first at that point of maximum shear on the central line below the contact area. However, the model developed above shows that the maximum shear occurs near the surface around the edges of the contact area. The justification for this model can be seen in Figure 3.8 (b). This micrograph is a higher magnification of a section of an impression produced by an aluminium impressor with mean pressure just sufficient to introduce plastic flow into the copper sample. The first visible signs of plasticity, i.e. delineation of grain boundaries and slip lines, occur where the model predicts.

This model can now be used in conjunction with the experimental observations presented in the previous section for copper. Applying equation 3.9, when $\rho=1$, the maximum shear on the surface:

$$\frac{S_{\max}}{P} = \frac{(1-2\nu)}{2} \quad (3.13)$$

For copper, as well as for typical metals, Poisson's ratio is on the order of 0.3 (Eisenstadt (1971) and Courtney (1990)). Using this value of Poisson's ratio and substituting in (3.13):

$$S_{\max} = 0.2P \quad (3.14)$$

where P is the minimum contact mean pressure to plastically deform the copper sample. This was measured as 0.78 GPa (Table 3.2).

Substituting the minimum contact mean pressure measured by the soft impression technique in equation 3.14, gives a maximum shear stress of 0.15 GPa. This value is directly comparable with the maximum shear stress ($S_{\max}=0.13$ GPa) measured by the standard tensile test method.

The two values determined by independent methods are given in Table 3.3.

Table 3.3 S_{max} of copper

S_{max} evaluated by the standard tension test methods	0.13 GPa
S_{max} predicted by the model and based on the minimum contact mean pressure	0.15 GPa

The agreement between the two values has reinforced the validity of the selection of the model and suggests that the soft impression technique is a suitable method for the evaluation of the flow stress of polycrystalline materials.

3.4.3 Evaluation of minimum contact mean pressure to deform ultra-hard materials (Syndax and Amborite).

One of the main features of ultra-hard polycrystalline materials (Syndax and Amborite) is their ability to retain their high hardness even at higher temperatures. This makes the choice of selecting soft impressors capable of deforming them at those temperature very limited.

◆ Experimental procedure and results

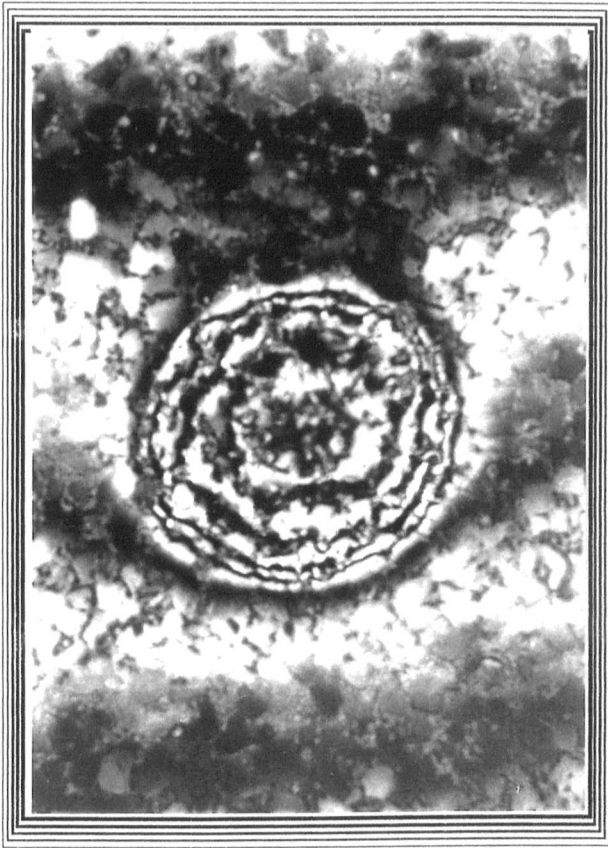
Two ceramic impressors were used to evaluate the minimum contact mean pressure of ultra-hard polycrystalline materials.

Polycrystalline cubic boron nitride (Amborite), with a room temperature Knoop hardness of 32 GPa, was selected to be used for the evaluation of the flow stress of Syndax (H_k at 20°C=50 GPa). Impressions in Syndax in the temperature range 700°-1300°C were round and there was no sign of crack formation over that

range of temperature. The use of the same impressor on Amborite (i.e. of similar hardness) has resulted in a relatively deep impressions (see Chapter 4) with severe cracks. On the other hand, the mean pressure generated by a titanium diboride impressor (H_k at $20^\circ\text{C} = 13 \text{ GPa}$) was insufficient to deform Syndax over the experimental temperature range, whereas it was able to deform Amborite without cracking.

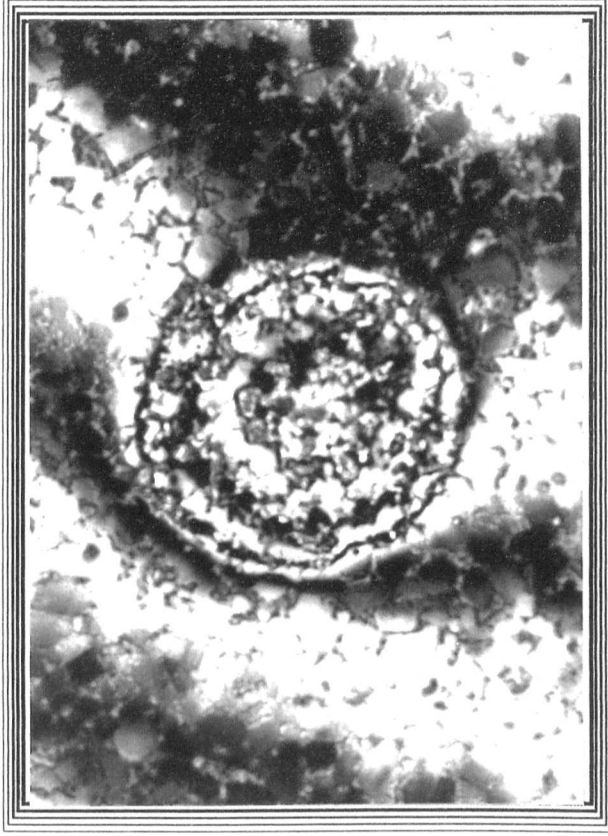
◆ Syndax

For the evaluation of the flow stress of Syndax, a cubic boron nitride impressor was loaded on the sample for 600s. Then the same impressor, at the same temperature, was reloaded on another position for the same time. This procedure was continued until a certain point when the contact mean pressure was just sufficient to deform the hard surface. The decrease of the mean pressure was achieved through the creep of the cone material as the dwell time was increased. Figure 3.14 (a, b and c) shows a series of impressions made with a cubic boron nitride impressor on Syndax at 900°C taken by the interference microscope. Figure 3.14 (a) shows that the first impression was the deepest (685 nm) and the depth decreased until it reached the minimum depth in Figure 3.14 (c) (274 nm) and that this impression was the shallowest which could be detected. The pressure to form this impression was taken as the minimum contact mean pressure at that particular temperature. The minimum contact mean pressures, for Syndax in this temperature range $700^\circ\text{-}1300^\circ\text{C}$, are shown in Table 3.3 and plotted in Figure 3.15.

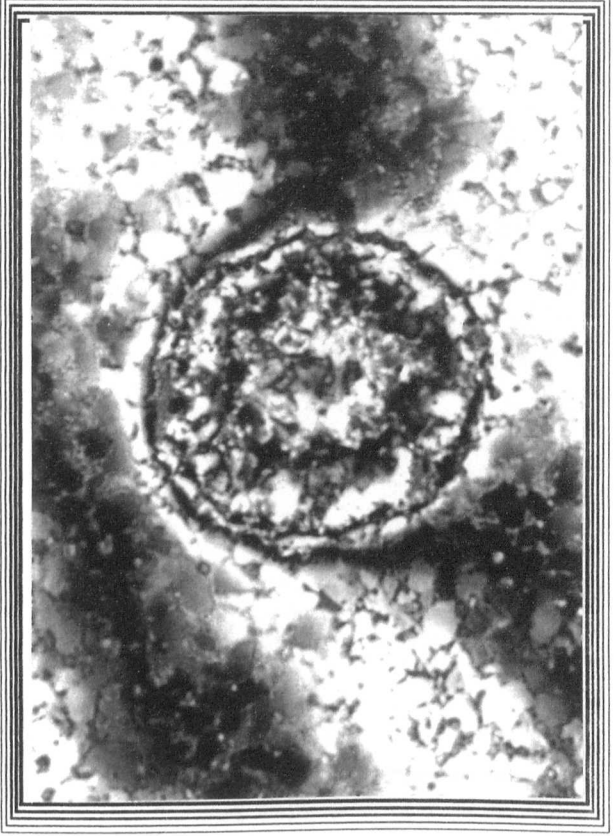


(a)

68 μm



(b)



(c)

Figure 3.14 Showing series of impressions made by cBN
impresor on Syndax at 900C

- (a) First impression
- (b) Third impression
- (c) Last impression

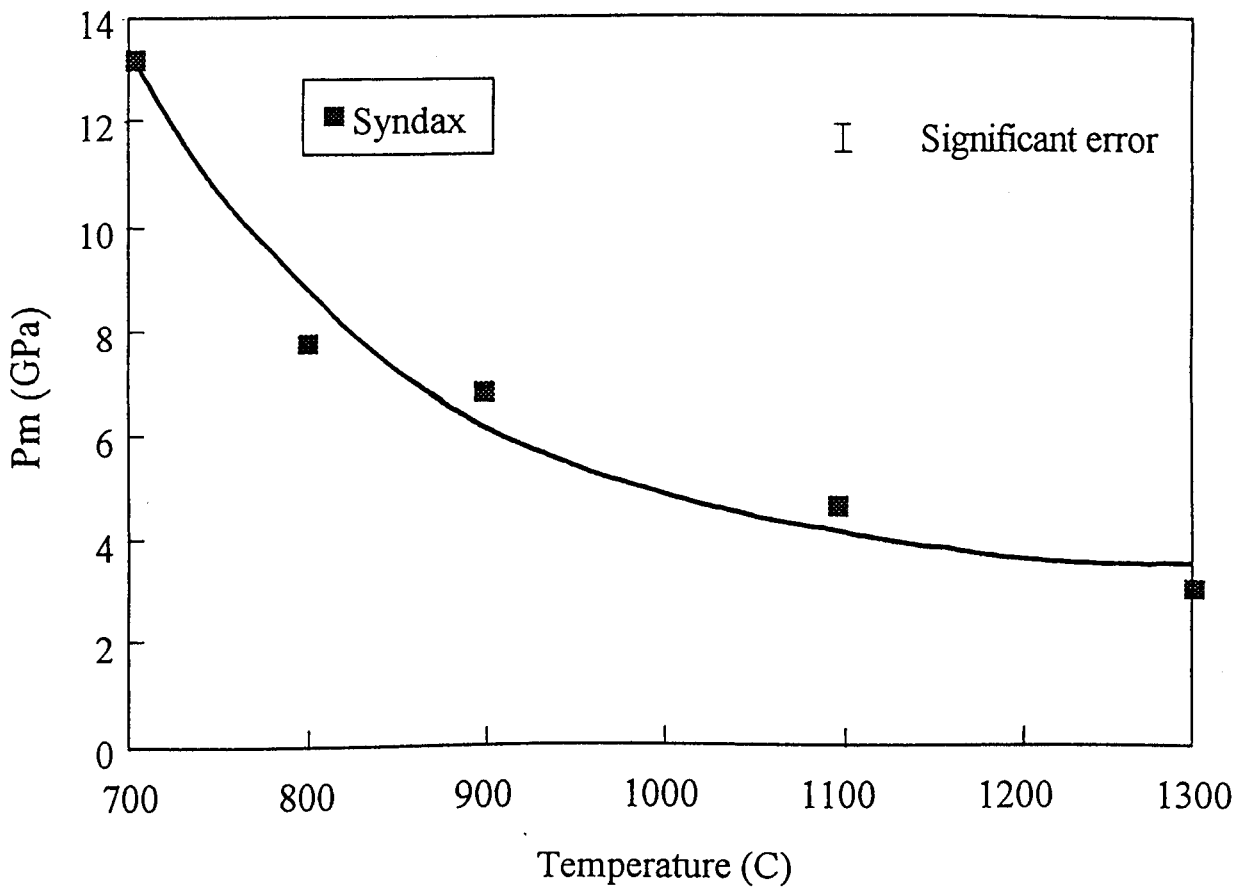


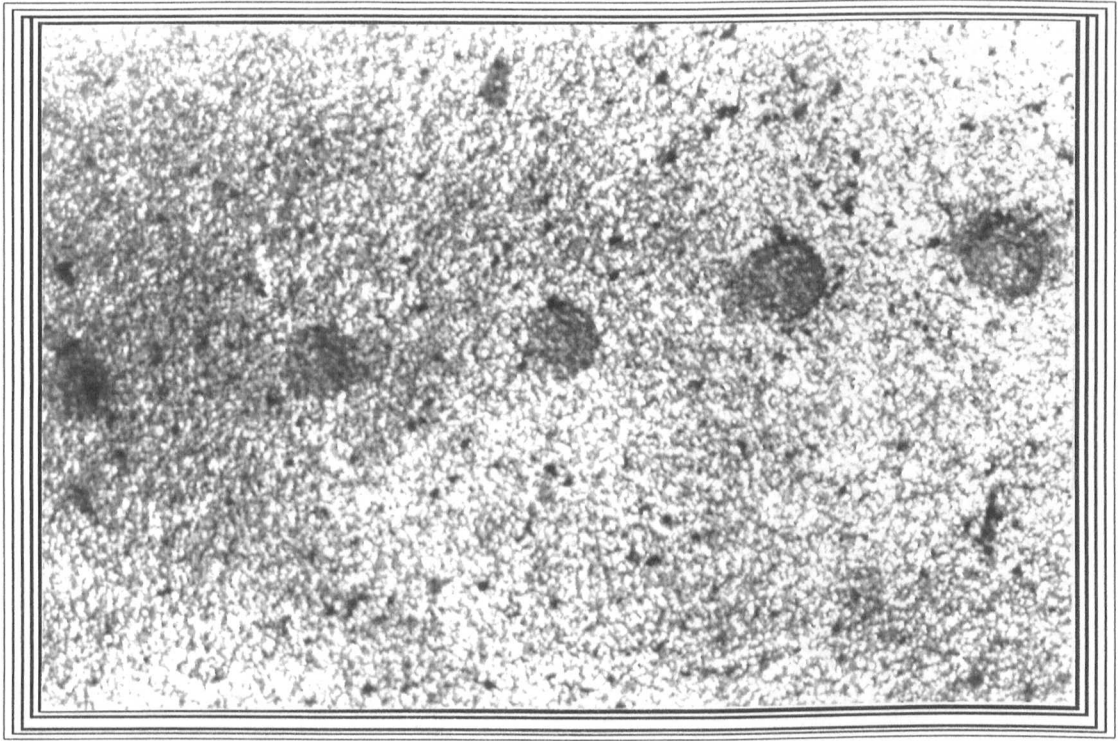
Figure 3.15 The minimum contact mean pressure to produce plastic deformation on Syndax vs temperature

Table 3.3 Minimum contact mean pressure of cBN on Syndax to produce plastic deformation.

Test No.	Temperature (°C)	P _m (GPa)
1	700	13.25
2	800	7.8
3	900	6.8
4	1100	4.6
5	1300	3

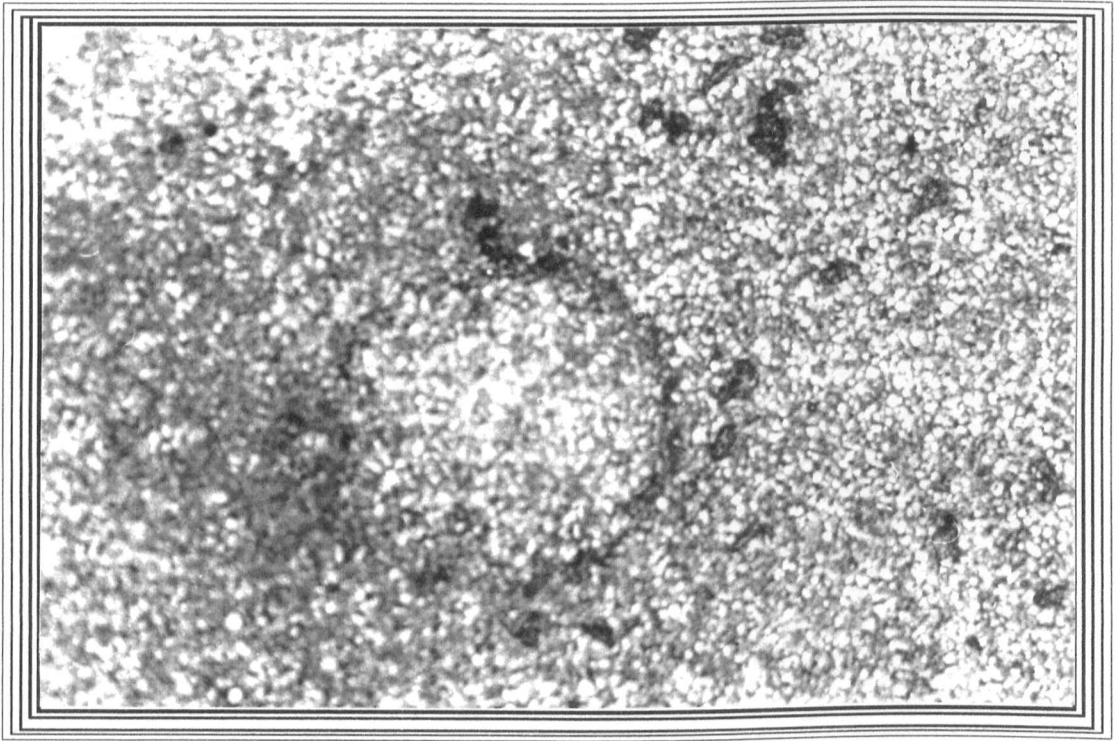
◆ **Cubic boron nitride (Amorite)**

The minimum contact mean pressure for plastic deformation of cubic boron nitride (Amorite) was evaluated using a TiB₂ impressor. The same procedure was followed as with the Syndax experiments. Figure 3.16 shows a series of impressions in cBN made by a TiB₂ impressor on Amorite at 800°C (mean contact pressure decrease from left to right). Figure 3.17 and Figure 3.18 are high magnifications of the last two impressions shown in Figure 3.16. By using the optical microscope to focus on the original surface and then on the centre of the contact area, it was established that the impression in Figure 3.17 was shallow whilst there was no significant depth to that shown in Figure 3.18. Therefore, the mean pressure to cause the former impression was taken as representing the appropriate minimum contact mean pressure- as summarised in Table 3.4 and plotted in Figure 3.19.



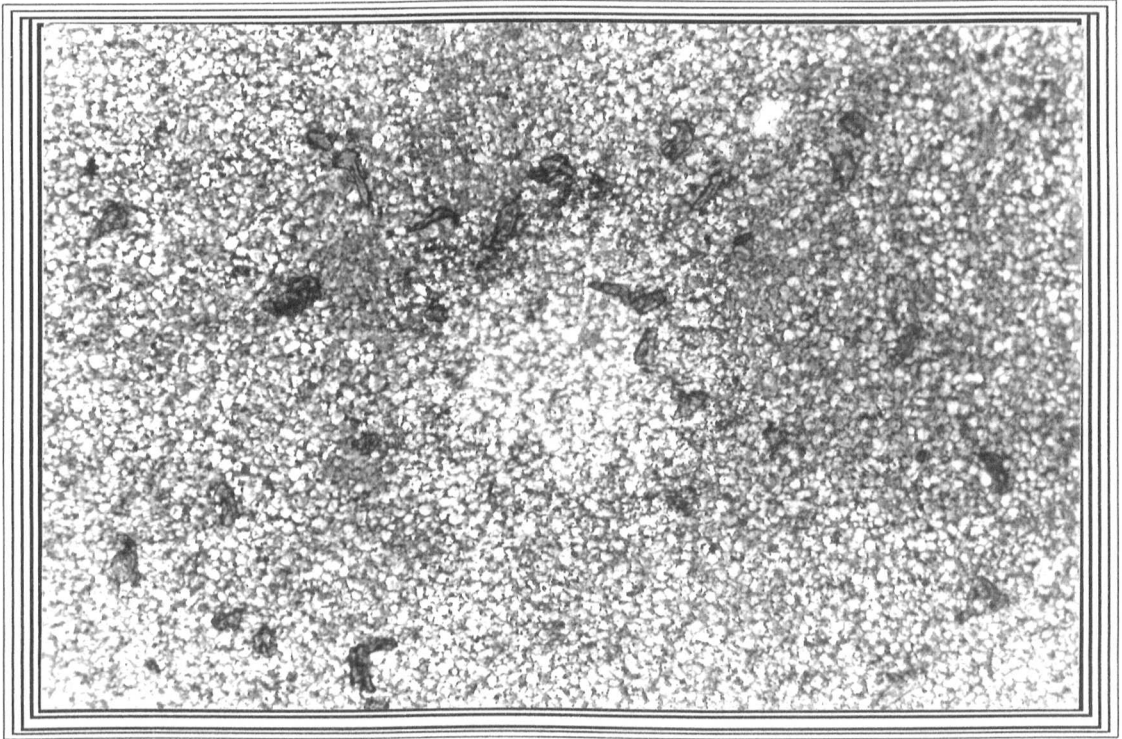
340 μ m

Figure 3.16 Shows a series of impressions (taken left to right)
made by TiB₂ impressor on Amborite at 800°C



← 89μm →

Figure 3.17 Showing high magnification of the penultimate impression (in figure 3.16)



85 μ m

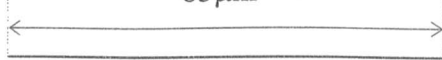


Figure 3.18 Showing high magnification of the the last impression
(in figure 3.16)

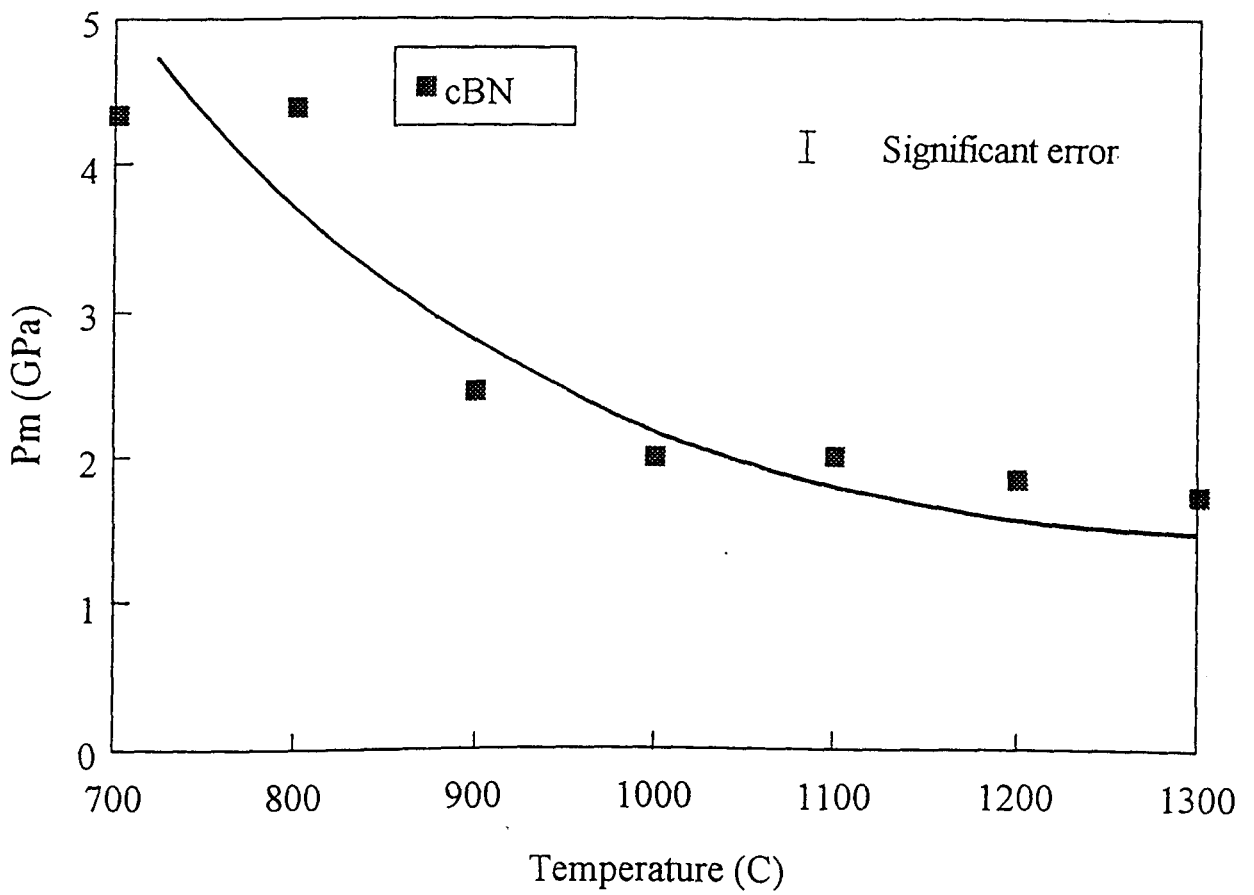


Figure 3.19 The minimum contact mean pressure to produce plastic deformation on cBN vs temperature

Table 3.4 Minimum contact mean pressure (P_m) of TiB_2 on cBN to produce plastic deformation.

Test No.	Temperature ($^{\circ}C$)	P_m (GPa)
1	700	4.35
2	800	4.4
3	900	2.45
4	1000	2
5	1100	2
6	1200	1.85
7	1300	1.74

3.5 Discussion

The replacement of the rigid indenter with a cone made from a softer material has proved to be an effective method for studying the plastic deformation of hard ceramics. Brookes *et al* (1988) used the soft impressor technique to study the plastic deformation of diamond. In subsequent work using that technique, the critical resolved shear stress and the B-D-T temperature of diamond were evaluated. In this technique, as the normal load was applied to a conical shaped impressor, the softer material flows flattening the tip and increasing the blunt contact area (decreasing the mean pressure, P_m). The generated mean pressure continues to deform the hard surface until it reaches a critical or threshold value (i.e. minimum contact mean pressure). Once this value (the minimum contact mean pressure) has been established, the corresponding value of the flow stress

(for polycrystalline materials) can be estimated by the application of a relevant model.

The minimum contact mean pressure required to deform polycrystalline copper has been verified by applying an impressor made from softer material (aluminium). The experimental procedure was based on the work done by Brookes *et al* (1991). A minimum mean pressure of 0.78 GPa which was just enough to show signs of plastic deformation around the contact area of the copper sample (as in Figure 3.8) was used in conjunction with the developed model. This model has shown that the maximum shear on the surface is

$\left(S_{\max} = \frac{P(1-2\nu)}{2\rho^2} \right)$ where $\rho = \frac{r}{a}$. This model was used to predict the maximum

shear stress at any point inside and around the contact area. Poisson's ratio and the minimum contact mean pressure were the two variables which affected the predicted shear stress (S_{\max}). Based on that integral, the maximum value of maximum shear stress (S_{\max}) was found to be at the edge of the contact area, or when $r/a=1$ i.e. $a = r$ (Figure 3.12). With Poisson's ratio equal to 0.3, the predicted value of maximum shear stress by the model was $S_{\max}=0.15$. This value has the same order of magnitude as the value (0.13 GPa) obtained by the conventional tensile test measurement shown in Figure 3.9. Since the model developed for the polycrystalline copper sample gave convincing results, it was decided to apply the technique to ultra-hard materials.

The flow stress of polycrystalline diamond (Syndax) and cubic boron nitride (Amborite) as a function of temperature, have been evaluated and, based on the model, the maximum shear stress was evaluated for both materials, (Table 3.5

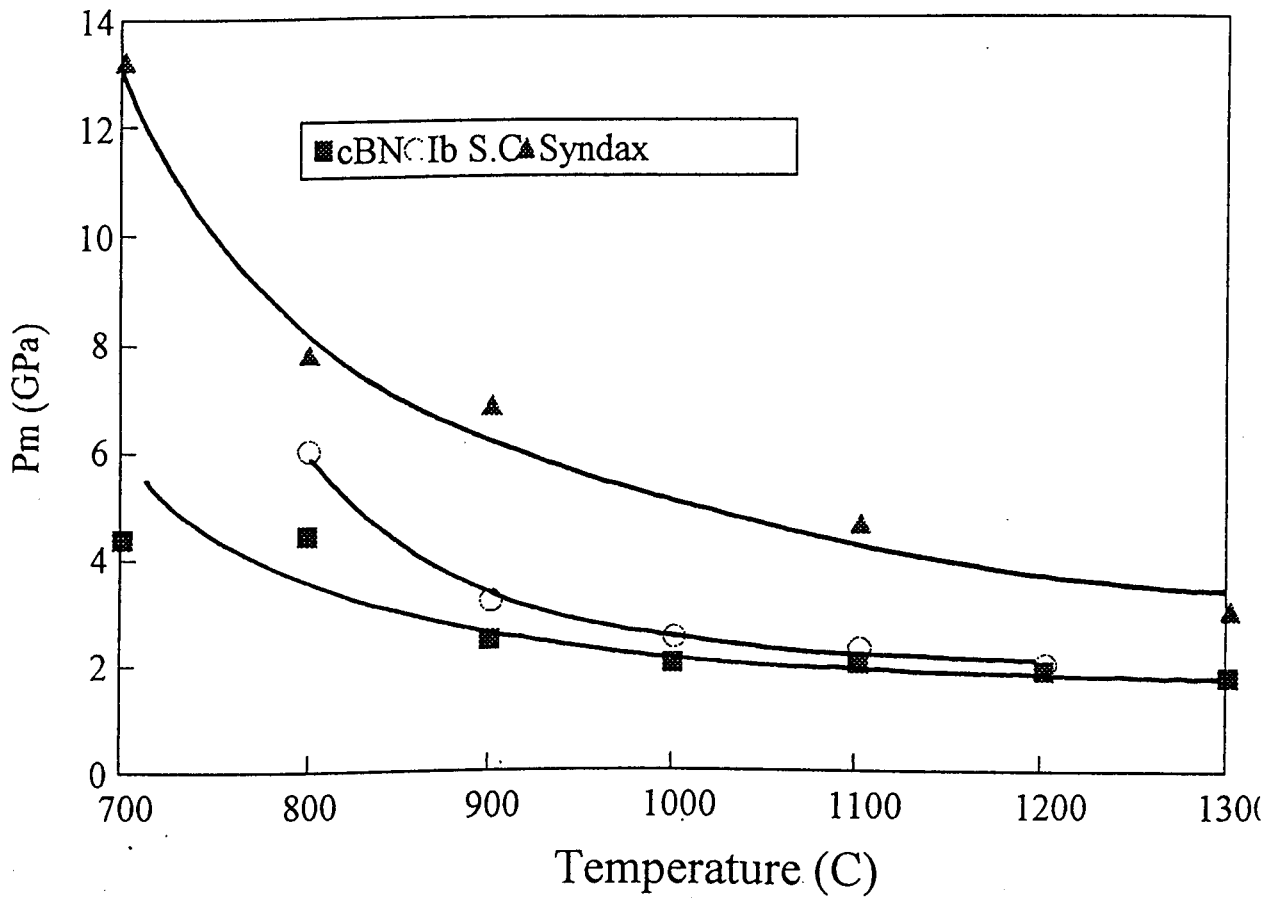


Figure 3.20 The minimum contact mean pressure to produce plastic deformation for cBN, Syndax and Ib diamond

and 3.6). Figure 3.15 and Figure 3.19 show the trend of mean pressure versus temperature and provide the basis for a comparison with the schematic in Figure 3.5. In all cases there is evidence to support the three regimes- (I) elastic regime, (II) plastic regime and (III) temperature insensitive regime. The relevant BDT lies between 700°-800°C for both Syndax and Amborite and regime III begins at about 1100°C. Thus the high temperature flow behaviour of polycrystalline diamond and cubic boron nitride is directly comparable with that of (Ib) synthetic diamond studied previously (Brookes 1992) where the brittle to ductile transition temperature occurs between 700°C and 800°C.

Figure 3.20 shows a direct comparison of minimum mean pressure versus temperature curve for Syndax and Amborite with a similar curve for Ib synthetic diamond single crystal (Brookes 1992). Polycrystalline diamond (Syndax) has a higher flow pressure, and hence a greater resistance to plastic deformation, than single crystal synthetic diamond over the whole range of temperature. The measurements were made with the same apparatus and under directly comparable experimental conditions (Chapter 2).

The variation in flow stress of single crystal and polycrystalline material was reported at elevated temperature, by Williams (1964) for titanium carbide single crystals and by Wolfe and Williams (1984) for polycrystalline titanium carbide. Williams evaluated the yield stress in compression for TiC single and polycrystalline specimens at elevated temperature and his data indicated that the polycrystalline titanium carbide had a higher yield stress, across the entire temperature range 900°-1600°C. He attributed this to the strengthening effect of

grain boundaries but it should be noted that the polycrystalline material was single phase - i.e. did not contain a binder or matrix.

In Regime I, room temperature - 750°C, deformation of single crystal diamond and polycrystalline diamond was purely elastic at low mean contact pressure but with fracture delineating the contact area at sufficiently high mean contact pressure. At these pressures, cone cracks were formed on {111} cleavage planes in single crystal diamond (Brookes, 1992). In this work the mean contact pressures appeared to be lower than the fracture stress, in that no significant cracking was apparent, and the transition from elastic to plastic behaviour without fracture was observed.

The elastic:plastic or brittle:ductile transition occurred in the same temperature range for single crystal diamond and for the polycrystalline form and this transition marked the advent of impression creep (continued plastic deformation with increased dwell time of the impressor). Dislocations become mobile in single crystal diamond at relatively low homologous temperatures ($0.3 T_m$) and the critical resolved shear stress for synthetic type Ib diamond has been estimated as 3.5 GPa at 770°C (Brookes, 1992). Under similar experimental conditions, plasticity is also the dominant mechanism in polycrystalline diamond but the mean pressure necessary to induce plasticity is higher and the flow stress is correspondingly greater, at 11 GPa.

In Regime II, the impressions in polycrystalline diamond were fully plastic and both the diamond network and the β -SiC network deformed plastically. The higher flow stress in polycrystalline diamond (Syndax) could be attributed to several mechanisms. An investigation of the deformation of single crystal

diamond using the soft impressor technique (Brookes, 1992) has shown that the critical resolved shear stress is higher for type IIa diamond which contain significant number of dislocations. It has been shown that high levels of strain are introduced during processing of polycrystalline diamond (Syndax), where the high temperature-high pressure conditions are sufficient to initiate both slip and twinning. (Walmsley, 1988). A high strained type Ib diamond network would require higher deformation pressures than strain free type Ib diamond and this would be reflected in an increased flow stress for the polycrystalline form. The role of both the silicon carbide network and possible grain boundary effects needs further investigation.

In Regime III, the flow stress of polycrystalline diamond and the critical resolved shear stress of single crystal diamond both become relatively temperature independent and the rate of impression creep increases. However, at temperatures above 1300°C polycrystalline diamond becomes thermally unstable. The nature of Amborite and Syndax microstructure is different. In Amborite, the contact and welding between the cBN particles exists to a lesser extent compared with that of diamond particles in Syndax (Chapter 1). Therefore, the flow stress of Amborite is lower than Syndax. In other words, Amborite shows higher plastic deformation than Syndax since the most likely mechanism, i.e. grain boundary sliding, is not restricted by the contact of the hard particles. Another reason which can be attributed to the high deformation of Amborite, is the relatively low melting point (1928K) of AlB_2 (the binder phase of Amborite) compared with 3000K for silicon carbide. The experimental temperature regime

for AlB₂ was between 0.5T_m- 0.8T_m whereas for SiC the temperature regime was between 0.3T_m -0.5T_m.

Table 3.5 Minimum mean pressure, maximum shear stress and flow stress (σ_f) of Syndax.

$$\nu=0.086^1$$

$$S_{max} / P = 0.414$$

Test No.	Temperature (°C)	Pm (GPa)	Maximum shear stress (S_{max}) (GPa)	Flow stress(σ_f) (GPa)
1	700	13.25	5.45	10.9
2	800	7.8	3.23	6.46
3	900	6.8	2.815	5.63
4	1100	4.6	1.9	3.8
5	1300	3	1.24	2.48

Table 3.6 Minimum mean pressure, maximum shear stress and flow stress (σ_f) of Amborite.

$$\nu=0.22^2$$

$$S_{max} / P = 0.28$$

Test No.	Temperature (°C)	Pm (GPa)	Maximum shear stress (S_{max}) (GPa)	Flow stress(σ_f) (GPa)
1	700	4.35	1.218	2.436
2	800	4.4	1.232	2.464
3	900	2.45	0.686	1.372
4	1000	2	0.56	1.12
5	1100	2	0.56	1.12
6	1200	1.85	0.518	1.036
7	1300	1.74	0.4872	0.9744

3.6. Conclusions

- 1) A model for measuring the maximum shear strength of polycrystalline materials has been developed and verified with data obtained from tensile measurements on polycrystalline copper.

¹ P.J Heath/ IDR 3/86

² P.J Heath/ IDR 3/86

- 2) The soft impressor technique has been extended and used to study the effect of temperature on the flow stress of polycrystalline diamond (Syndax) and cubic boron nitride (Amorite). These results confirm a brittle to ductile transition temperature between 700°C and 800°C for both materials.

- 3) The plastic deformation of these polycrystalline materials are similar to those of single crystal diamond in that there are three distinct regimes. At room temperature and in the elastic regime I, there is no discernible dislocation movement and fracture occurs at a sufficiently high contact pressure. In the plastic regime II, dislocations movement is observed, time dependent flow stress occurs and the flow stress falls rapidly over this temperature regime but, ultimately, becomes relatively temperature insensitive in the third regime III.

4. Flow stresses for Syndax are greater than those of Ib synthetic diamond indicating the strengthening effect of the grain boundaries and the continuous β -SiC boundary phase. Also, this could be attributed to strain introduced during the sintering process of Syndax.

5. Flow stresses for Amorite are lower than those of Syndax, at a given temperature, and it is suggested that the presence of a continuous grain boundary phase (AlB_2) is primarily responsible for this difference.

Chapter 4 Impression creep

4.1 Introduction

Creep is normally defined as time dependent plastic deformation and becomes increasingly important with increasing temperature above one third of the melting point ($0.33 T_m$) for a given material. At the highest temperature, this form of plastic flow can occur at stresses less than the nominal yield stress. In the rake face of a cutting tool, the temperature may reach about 1000°C and therefore, this cumulative deformation mechanism could play an important part in the machining performance and tool wear. As described more fully later in this chapter, several mechanisms contribute to creep in crystalline materials such as dislocation motion and diffusional flow of atoms. Here, the soft impression technique is used to study time dependent plastic flow in ultra-hard polycrystalline materials above the BDT.

Normally, a creep test consists of applying a load to a specimen and measuring the deformation or strain as a function of time for a given experimental temperature, where the creep rate can then be expressed as $d\epsilon/dt$. Although the experimental methods involved in constant stress testing have been known for many decades, most creep data has been recorded using constant load equipment. If the creep ductility of a material is low, the results obtained with constant load and constant stress test methods are comparable. However, when constant load tensile tests are carried out with materials characterised by high creep ductility, the true stress on the specimen increases as creep continues,

resulting in faster deformation and more rapid failure than is observed with constant stress tests under the same condition.

At high temperature, the creep curves (ϵ vs t) are usually described by reference to different regions of the curves. After the initial instantaneous elastic, and perhaps also plastic strain on loading, the primary creep rate usually decays during 'stage I' until a constant creep rate is reached. This is 'stage II', also called steady state or secondary creep.

For a given material, the steady state creep rate depends only on stress and temperature but not on prior creep strain or time (Evans and Wilshire 1993), i.e.

$$\dot{\epsilon} = f(\sigma, T) \quad (4.1)$$

It is rather observed that the effects of stress and temperature can usually be assumed to be independent, giving:

$$\dot{\epsilon} = \mu(\sigma) \nu(T) \quad (4.2)$$

where the function $\mu(\sigma)$ describes the variation of $\dot{\epsilon}$ with stress and the function $\nu(T)$ describes the dependence of $\dot{\epsilon}$ on temperature.

Thus for a given stress,

$$\dot{\epsilon} \propto \nu(T) \quad (4.3)$$

When creep tests are carried out at the same stress but at different temperatures, it is usually found that a straight line relationship is obtained by plotting $\log \dot{\epsilon}$ against $(1/T)$:

$$\log \dot{\epsilon} \propto -(1/T) \quad (4.4)$$

Function (4.4) shows that the secondary creep rate increases exponentially with temperature, and this temperature dependence is found for many different processes, including diffusion. Therefore creep obeys Arrhenius's law, so that:

$$\dot{\epsilon} \propto \exp. -(Q/RT) \quad (4.5)$$

where Q is the activation energy for creep and R is the universal gas constant ($8.31 \text{ J mol}^{-1} \text{ K}^{-1}$).

On the other hand, with a fixed temperature and different stresses, a straight line relationship is observed for $\log \dot{\epsilon}$ plotted against $\log \sigma$:

$$\dot{\epsilon} \propto \sigma^n \quad (4.6)$$

where n is the gradient of the line.

The relationships in equations (4.5) and (4.6) can be used to rewrite equation (4.2) and the steady state creep rate can be correlated to stress and temperature by:

$$\dot{\epsilon} = A \sigma^n \exp-(Q/RT) \quad (4.7)$$

where A is a constant. This power law relationship provides an excellent description of the steady state creep behaviour of many materials and can be used to evaluate the activation energy and the stress exponent (n) for the tested material.

The measurement of creep rates by uniaxial creep tests are relatively time consuming and require large and easy to machine samples. The hardness test has traditionally been used for materials of which samples are only available in restricted sizes and geometry, as a measure of strength and fracture toughness (Ponton and Rawling 1989). The standard hardness tests usually use a dwell time between 12-30 seconds to avoid the creep effects. However, by increasing the time for which the load is maintained on the indenter (dwell time), the measured hardness will be affected due to indentation creep as the size of the indentation grows with extending dwell time. The use of indentation creep to evaluate the creep behaviour of small size materials is attractive given the problems of size, machinability and brittleness of ceramic materials.

The effect of increasing dwell time was first observed by Hargreaves (1928) through his investigation of the hardness of soft metals and he observed a power law relationship between the indentation diameter and the time at a constant temperature and load as follows:

$$\log P = H - h \log t \quad (4.8)$$

Where P is the hardness for different dwell times, H and h are Hargreaves constants.

Standard uniaxial creep tests create an increase in the strain while the overall volume of the specimen is maintained, whereas in the case of indentation tests the strained volume below the indenter is localised but it enlarges with time. If a hard indenter is pressed into the flat surface of a ceramic material, the initial stresses are high and the magnitude of strain is such that cracking occurs to relieve the strain under the indenter, which then constrains the plastic flow. The soft impressor technique permits the application of a wider range of mean pressures and a facility for controlling the resultant strain such that plastic flow can proceed unconstrained by fracture. Creep resistance can be studied under conditions of varying time and temperature in a regime entirely governed by plastic deformation.

4.2 Review of indentation creep

Following the original work of Hargreaves (1928), a number of valuable attempts have been made to correlate the hardness behaviour of metals and alloys with their known creep characteristics.

Mulhearn and Tabor (1960) carried out a comparative study of the hardness and creep of single crystals of lead and indium. They found a straight line relationship between $\log P$ (indentation mean pressure or hardness) and $\log t$, and they reported that the slope of these lines was independent of the test temperature. However, this work was followed by Atkins, Silverio and Tabor (1966), who showed that the slope increased with increasing temperature. This was confirmed

by many workers, among them Morgan (1976) who studied the behaviour of silicon.

In their study, Mulhearn and Tabor (1960) suggested that in the indentation experiments the creep process could be correlated with a typical tensile creep relation of the form of equation (4.7) and developed a relationship where the activation energy for the flow process could be measured:-

$$\log t_1 - \log t_2 = (Q/R) [(1/T_1)-(1/T_2)] \quad (4.9)$$

Where T_1 and T_2 are two test temperatures.

Atkins *et al* (1966) suggested two major weaknesses in the earlier work of Mulhearn and Tabor. Firstly, their suggestion that the slope of $\log P - \log t$ lines is constant and independent of temperature. Secondly, they used the steady state creep equation which considers that the applied stress remains constant during the creep test. However, this is not the case as the indentation grows under a constant load. Atkins *et al* (1966) used the transient-creep equation developed by Mott (1953):

$$\dot{\epsilon}_t = A \dot{\epsilon}_s^{1/3} t^{-2/3}$$

where A is independent of both stress and temperature and $\dot{\epsilon}_s$ is the steady state strain rate, and combined it with the steady strain rate equation (4.7) to analyse the mechanism of the creep during indentation. From this the following relationship was developed:

$$P^3 - P_0^3 = A \exp(-Q/3RT) \cdot (t^{1/3} - t_0^{1/3}) \quad (4.10)$$

where P is the hardness at time t , and P_0 is the hardness immediately after attaining the full load at t_0 and A is a constant. The authors used their simplified form to analyse their experimental work on tin, aluminium and single crystal magnesium oxide at a number of temperatures above half of the melting point ($0.5T_m$). They plotted $\log (P^{-3} - P_0^{-3})$ against $\log (t^{-1/3} - t_0^{1/3})$ for the data collected from those materials. The plotted lines were approximately straight and parallel and the interval between any two lines gave the value of $Q/3R [(1/T_2) - (1/T_1)]$ where the creep activation energy Q was calculated. In this work a good correlation was found between Q and the activation energy for self-diffusion. They also established that, for all the indenters, the variation in hardness with loading time was independent of the indenter shape for small and large spheres and for cones of apical angles of 105° , 120° , 136° , and 150° .

Roebuk and Almond (1982) showed that the strain rate could be defined according to the following :

$$\dot{\varepsilon} = \frac{d \ln D}{dt} \quad (4.11)$$

where D is the indentation diagonal. The strain rates at various indentation diagonals (i.e. hardness levels) were determined from the slopes of plot of D versus t or $\ln D$ versus time. Since indentation diagonals can be converted to hardness values, strain rates were obtained as a function of hardness. A plot of $\log \dot{\varepsilon}$ versus \log (hardness) should give information on the stress exponent n in the creep equation (4.7). Santhanam *et al* (1986) applied conventional and indentation creep tests methods to two WC-Co systems to evaluate the stress

exponents at 1000°C. They found that both creep tests yielded similar stress exponents.

By employing the constitutive law for creep;

$$\dot{\epsilon} = \dot{\epsilon}_0 \left[\sigma / \sigma_0 \right]^n \quad (4.12)$$

where $\dot{\epsilon}_0 = K \exp (-Q/RT)$, σ is the shear stress and σ_0 is a reference stress at which the strain rate is $\dot{\epsilon}_0$, Sargent and Ashby (1989) derived the following equation by normalising by the shear modulus to remove the dependence of σ_0 on temperature:-

$$\frac{H_{(t)}}{G} = \left[\frac{\sigma_0 / G}{nC \dot{\epsilon}_0 t} \right] \frac{1}{n} \quad (4.13)$$

where $H_{(t)}$ is the hardness after dwell time t , G is the shear modulus at temperature T , σ_0 is the reference stress at a strain rate $\dot{\epsilon}_0$ and C is a geometric constant independent of load and temperature. The creep exponent n can be found from equation (13) and the gradient of a plot of $\log (H/G)$ against $\log t$ at constant temperature, T is $-(1/n)$. The activation energy of creep can be derived from the slope of a $\ln(H/G)$ against T_m/T plot at constant dwell time i.e the gradient is Q/RT_m .

Indentation creep is influenced by a large number of variables such as the plastic deformation properties of the material, diffusional processes, normal load, anisotropy, etc. Most of the previous analyses of this problem were based almost exclusively on power law creep. This approach has created some difficulties in

relating time dependent hardness to a creep equation for uniaxial stress which is based on data obtained under constant stress conditions whereas the stress under the indenter decreases with increasing dwell time.

An important observation of results of indentation hardness creep is that most materials, including ceramics and even diamond, are found to creep at temperatures well below half their melting point e.g. experimental work by Brookes *et al* (1990, 1991) where they showed that multiple intersecting slip was initiated in type I, type II and synthetic diamonds at relatively low homologous temperatures, i.e. $\cong 0.35T_m$. This aspect of low temperature creep led Li *et al* (1991) to develop a creep analysis without assuming the steady state power law creep relationship. They attempted to analyse all the possible mechanisms which may contribute to the indentation creep and to obtain a rate equation for each mechanism.

There are a number of possible mechanisms of plasticity some or all of which may contribute to indentation creep. The mechanisms considered were as follow:

- 1) Plasticity (dislocation glide).
- 2) Power law creep (climb plus glide).
- 3) Power law breakdown (glide plus climb).
- 4) Recovery (dislocation climb).
- 5) Diffusion (volume, grain boundary or dislocation pipe diffusion).

Li *et al* (1991) derived seven rate equations for the different possible mechanisms. All were derived on the assumption that steady state creep is established which needs a certain minimum incubation time. Therefore these rate equations are not suitable for very short time, i.e. they are not applicable to the

indentation hardness experiments because the latter exhibit non-steady state creep at times of up to a few seconds and this initial period is hard to treat theoretically.

4.3 Creep deformation in ceramics and hard materials

Ceramics and ceramic composites are being considered increasingly for industrial applications at elevated temperature. In order to understand the deformation behaviour of these materials at high temperature a large number of experiments have been carried out in the last few decades to investigate their creep behaviour. Ceramics deform plastically at high temperature under most experimental conditions and the dominant deformation mechanism at high stresses is a diffusion controlled dislocation creep process in which the creep rate is independent of grain size (Ruano and Sherby 1994). At low applied stresses and fine grain sizes, other mechanisms have been reported to be rate-controlling. These mechanisms include diffusional creep processes (Nabarro-Herring (N-H) and Coble) and grain boundary sliding.

In this chapter the impression creep behaviour of ultra-hard polycrystalline materials (Syndax and Amborite) will be described on the basis of results obtained by applying the soft impression technique. For the purpose of comparison, the creep behaviour of a selected number of hard ceramics has been reviewed.

Masson *et al* (1992) carried out creep tests in compression on sintered and hot pressed AlN (one of the phases which exist in Amborite) at temperatures from

1500° to 1650°C (0.45-0.59 T_m) and at stresses of 200 MPa in an argon atmosphere. The purpose of this study was to examine the creep behaviour at high temperature and to characterise the deformation mechanisms by TEM, in order to study the dislocation substructures after mechanical testing. The results showed that the creep rate increases with temperature and with reduction in grain size. Another important result was the observation of cavitation on sintered AlN; the cavities of cylindrical shape and localised at grain boundaries and triple points with a random distribution and this material showed a much larger dislocation density in the deformed grains. Some intergranular deformation was also observed. The dislocations were isolated, gathered together in subgrain boundary configurations or in triple nodes formation. Hot pressed AlN showed higher creep rates in the absence of cavitation. The authors have related the higher creep rate in HPAIN to the larger amount of second phase (lanthanum aluminate, $\text{LaAl}_{11}\text{O}_{18}$). Jou and Virkar (1990) studied the creep rate in polycrystalline AlN in four point bending and in particular investigated the influence of grain size, stress and temperature on creep rate. They showed that creep in polycrystalline aluminium nitride predominantly occurs by means of both bulk and boundary diffusion mechanisms.

Wermark *et al* (1984) investigated the tensile creep behaviour of WC-Co alloy at 800°-900°C (0.34-0.37 T_m) with different content of the binder phase. They indicated that the creep strength decreases with increasing cobalt-content which is consistent with the finding of previous investigators such as Suzuki *et al* (1982). Evidence for grain boundary sliding (GBS) has been observed and the magnitude of the offsets at grain boundaries is consistent with grain boundary

sliding making a substantial contribution to the total strain. There was an absence of extensive cavitation, which indicates that this was not a major mechanism of accommodation in the temperature and stress range used in their study. The formation of ordered dislocation networks and subgrains was common in materials which had undergone creep deformation, indicating that the hard particles (WC) had also undergone plastic deformation.

Kossowsky *et al* (1975) studied the tensile creep of hot pressed silicon nitrides. They showed that deformation occurred by the mechanism of grain boundary sliding (GBS) and the creep behaviour was controlled by temperature and impurities such as Ca, which affect the viscous flow of the grain boundary glass phase. Lowering the amount of Ca present to $\leq 100\text{ppm}$, greatly improved the creep strength.

Grain boundary sliding seems to be the major factor in the deformation of multi-phase materials. Chokshi (1990) tried to evaluate the grain boundary sliding contribution to the creep deformation in polycrystalline alumina. Two different polycrystalline alumina samples were chosen: one was a commercially hot pressed alumina doped with 0.25% MgO and the other was made with high purity alumina powder. The creep tests were conducted in four-point bending mode at a temperature of 1400°C . There was considerable microstructural evidence for the occurrence of grain boundary sliding and grain rotation during creep deformation. Experimental measurements revealed that the grain boundary sliding contribution to the total strain during creep deformations was $\cong 76\%$. The extensive grain boundary sliding observed, suggested that polycrystalline alumina exhibits superplastic characteristics. In the light of his study Chokshi concluded

that creep occurs either by an independent grain boundary sliding mechanism or by an interface controlled diffusion mechanism.

In order to understand the creep behaviour of ceramics Wilkinson (1993) classified ceramic materials into single phase and three other classes of composites, according to their microstructure. He started with pure ceramic materials (single phase), i.e. those which do not contain amorphous or extensive second phase regions. Then he considered the systems which contain discrete second phase particles (primarily whiskers), fabricated by mixing two powders and sintering with or without external pressure (class I). An example of this class is alumina reinforced with silicon carbide whiskers. The volume fraction of the hard phase in such systems is usually low (up to about 30 vol%), and the particles are generally only in point contact with one another. Class II consists of materials obtained by infiltration into a powder compact to produce composites with a high volume fraction of the hard phase (of the order of 50 vol%), and in which particles make facet-to-facet contacts, i.e. the hard phase forms a continuous network. The most important example in this class is siliconised silicon carbide. In this material the silicon penetrates the contacts between particles to provide a thin silicon film along each SiC-SiC interface. Finally, class III composite materials in which the hard phase occupies a very large volume fraction (greater than 90%), with the particles bonded together by a soft phase such as silicon nitrides and WC-Co system.

1) Single phase materials

It has been established that the creep rate in alumina is independent of the nature of the load, i.e. tension or compression. The stress exponent for creep varies between 1 and 2, with the higher exponent being more common for fine grained ($\cong 1\mu\text{m}$) materials. This is suggestive of creep controlled by grain boundary sliding processes leading to superplastic behaviour.

2) Class I composites:-

The material considered here was SiC-whisker-reinforced alumina. In common with the matrix, these materials exhibited a well defined steady state regime during creep. Analysis of the data is complicated somewhat by the effect of the whiskers on processing due to the use of different sintering additives and processing conditions for the composites and whisker-free materials and differences in matrix grain size. Some general conclusions can be reached about the creep of these materials. One such conclusion is that the latest results have shown that the stress exponent for creep is between 1 and 2 at low stresses (i.e. similar to that of the matrix), and rises with increasing stress due to the onset of cavitation during creep mechanisms.

3) Class II composites:-

The creep resistance of siliconised silicon carbide systems is characterised by a creep rate at a given stress being much higher in tension than in compression. At high stresses cavitation is important in tension, whilst creep is controlled by deformation within the SiC particles themselves in compression (Wilkinson, 1993).

4) Class III composites:-

Silicon nitride can be thought of as a glass matrix composite containing between 90 and 99 vol% of β -silicon nitride. The creep resistance of these materials is 8-10 orders of magnitude greater than that of the glass itself, which undergoes viscous flow in the absence of reinforcement. The clearest evidence for this process was found in a study of a $Y_2O_3-Al_2O_3$ material in which the creep rate is found to decrease dramatically as the glass was squeezed from between boundaries under compression (Chadwick *et al* 1993).

4.4. High temperature impression creep tests of Syndax and Amborite

4.4.1 Experimental procedure

The impression creep tests were conducted using cubic boron nitride material for the impressors which were ground to an included angle of 120° . The tested materials were Syndax (representing polycrystalline diamond materials) and Amborite (representing polycrystalline cubic boron nitride materials). All of the experiments described here were carried out using the apparatus which was described and illustrated in Chapter 2. Impressions were made for dwell times of 300s, 1000s, 1800s and 3000s for each temperature and an initially sharp impressor was used for each individual measurement. The selected experimental temperatures were 1000° , 1250° and 1450°C for Amborite and 850° , 1000° , 1200° , and 1300°C for Syndax.

Measurement of the diameter of the contact area was made by using a micrometer eyepiece on a Nikon Optiphot light microscope.

In this study, the volumes and depths of the impressions on Amborite and Syndax specimens were obtained and evaluated by using the system developed in this department based on the direct phase detecting interferometer (DPDI) (described in Chapter 2).

The experimental working temperatures were selected to cover the common working temperatures during their use as toolpieces in metal cutting applications. But in the case of Syndax the highest temperature (1350°C) was determined by the onset of material degradation.

4.4.2 Experimental results

◆ Cubic boron nitride (Amborite)

Figure 4.1 shows the impression volume vs time plot for cBN at 1000, 1250 and 1450°C (the homologous temperature range between 0.36 and 0.5 T_m). The volume, mean pressure and the depth of each impression are shown in Table 4.1.

Table 4.1. Creep deformation of Amborite by cBN impressor.

A) Temperature 1000°C.

Time (s)	Volume ($\mu\text{m}^3 \cdot 10^4$)	Mean pressure (GPa)	Depth (μm)
300	4.36	11.49	9.5
1000	4.98	10	13.5
1800	6.37	9.2	13.7
3000	8.29	8.66	14

B) Temperature 1250°C.

Time (s)	Volume ($\mu\text{m}^3 \cdot 10^4$)	Mean pressure (GPa)	Depth (μm)
300	6.6	9.46	11
1000	8.75	8.88	16
1800	10.6	8.4	17.8
3000	7.2	8	16

C) Temperature 1450°C.

Time (s)	Volume ($\mu\text{m}^3 \cdot 10^4$)	Mean pressure (GPa)	Depth (μm)
300	6.78	7.53	17.4
1000	10.7	6.98	20.5
1800	11.2	6.5	21
3000	16	5	25.2

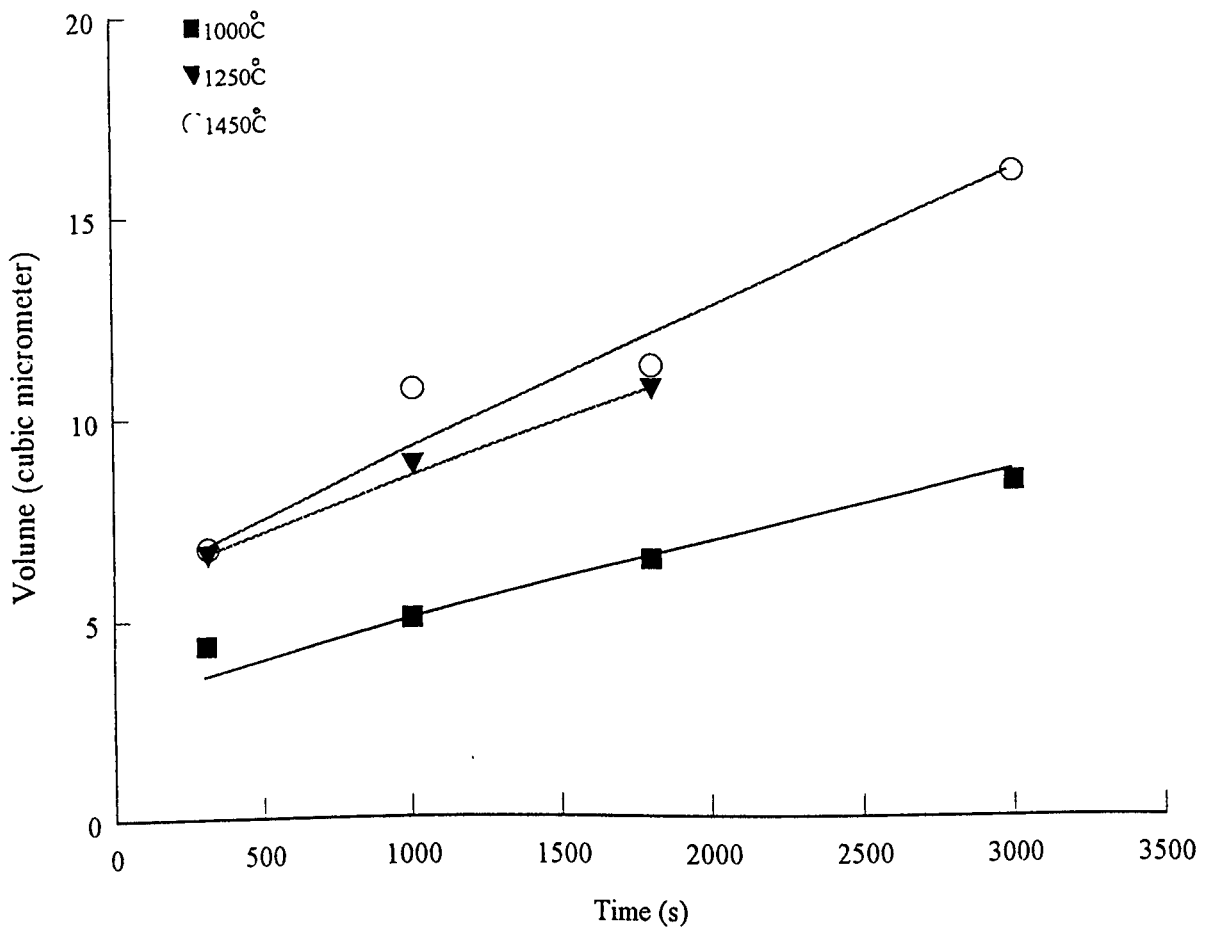


Figure 4.1 Indentation volume vs dwell time for Amborite deformed using a cBN impressor

Similarly, the effect of extended dwell time on the volume of the impressions in Syndax is shown in Table 4.2 for temperatures of 850, 1000, 1200, and 1300°C (the homologous temperature range between 0.3 and 0.4 T_m). Figure 4.2 shows the impression volume V 's time plot for Syndax.

Table 4.2. Creep deformation of Syndax by cBN impressor.

A) Temperature 850°C.

Time (s)	Volume ($\mu\text{m}^3 \cdot 10^4$)	Mean pressure (GPa)	Depth (μm)
300	0.86	16.63	2.2
1000	1.1	12.36	3
1800	1.65	8.85	2.5
3000	2.03	8.6	3.5

B) Temperature 1000°C.

Time (s)	Volume ($\mu\text{m}^3 \cdot 10^4$)	Mean pressure (GPa)	Depth (μm)
300	1.12	15.7	≈ 3
1000	1.6	10.15	4
1800	2.44	8.42	5
3000	2.8	8.14	5

C) Temperature 1200°C.

Time (s)	Volume ($\mu\text{m}^3 \cdot 10^4$)	Mean pressure (GPa)	Depth (μm)
300	3.2	12.7	5.9
1000	4.1	8.84	6.5
1800	4.5	7.53	6.4
3000	3.8	6.98	6.6

D) Temperature 1300°C.

Time (s)	Volume ($\mu\text{m}^3 \cdot 10^4$)	Mean pressure (GPa)	Depth (μm)
300	3.89	8	4.7
1000	4.273	6	5.3
1800	5.96	5.7	5.37
3000	6.57	5.5	6.1

◆ **Syndite**

The same technique was applied using cBN impressors on Syndite. The experimental temperatures were restricted between 700°-900°C to avoid the

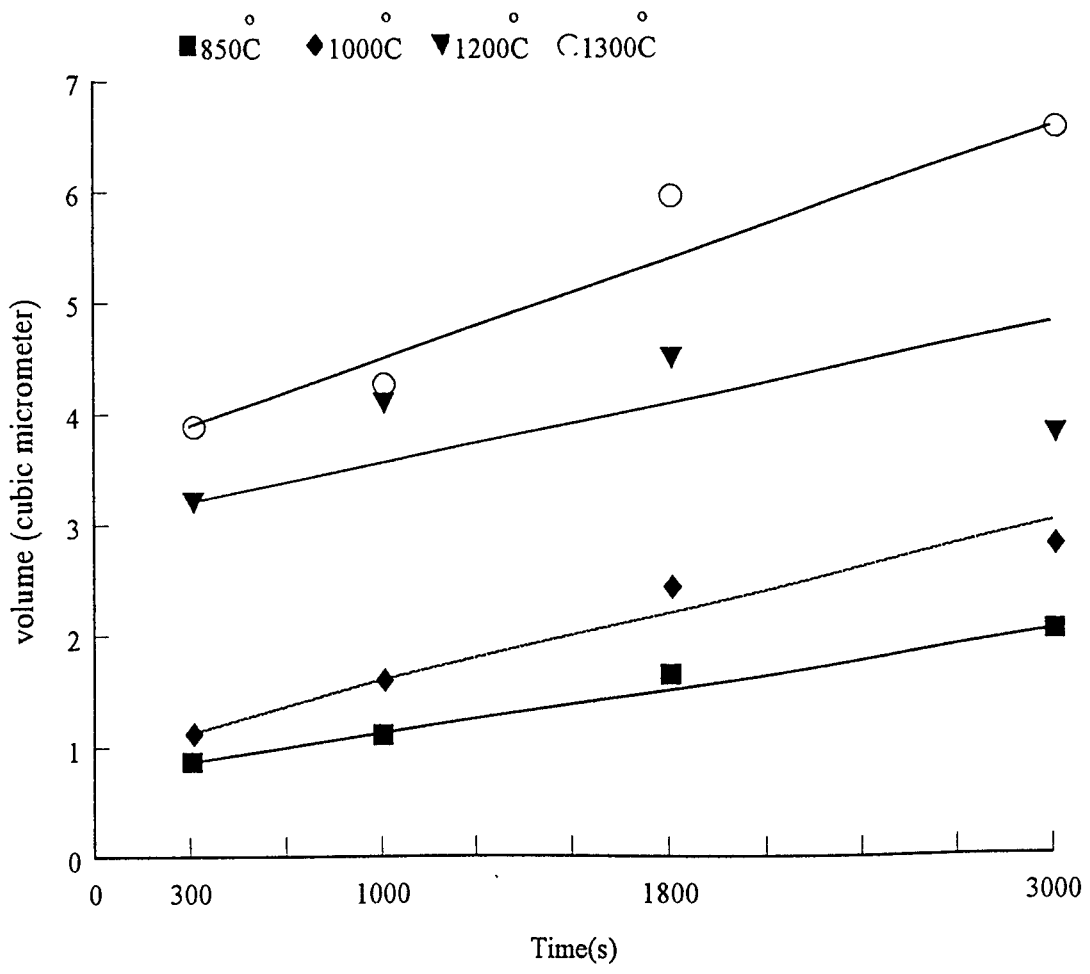


Figure 4.2 Indentation volume vs dwell time for Syndax deformed using a cBN impressor

thermal degradation of the diamond layer. However, no plastic deformation was observed within this temperature range.

◆ **Activation energies**

The rate of change of volume for a given experimental temperature was evaluated and the results are summarised in Tables 4.3 and 4.4 and plotted as volume rate change against the reciprocal of temperature in Figure 4.3. The gradient of the lines shown in those figures give activation energies Q of 0.33 eV (32 kJmol⁻¹; 1.0 RT_m) for Syndax and 0.32eV (31 kJmol⁻¹; 1.3RT_m) for Amborite.

Table 4.3. The rate of change of volume for a given experimental temperature.

A) Syndax:

Temperature(°C)	10 ⁴ /T, K	Volume rate (v)	ln (v)
850	8.9	3.98	1.38
1000	7.8	7.14	1.96
1200	6.7	9.63	2.2
1300	6.3	10	2.3

Table 4.4. The rate of change of volume for a given experimental temperature.

B) Amborite

Temperature(°C)	10 ⁴ /T, K	Volume rate (v)	ln (v)
1000	7.8	17.7	2.8
1250	6.5	27.7	3.3
1450	5.8	34.7	3.55

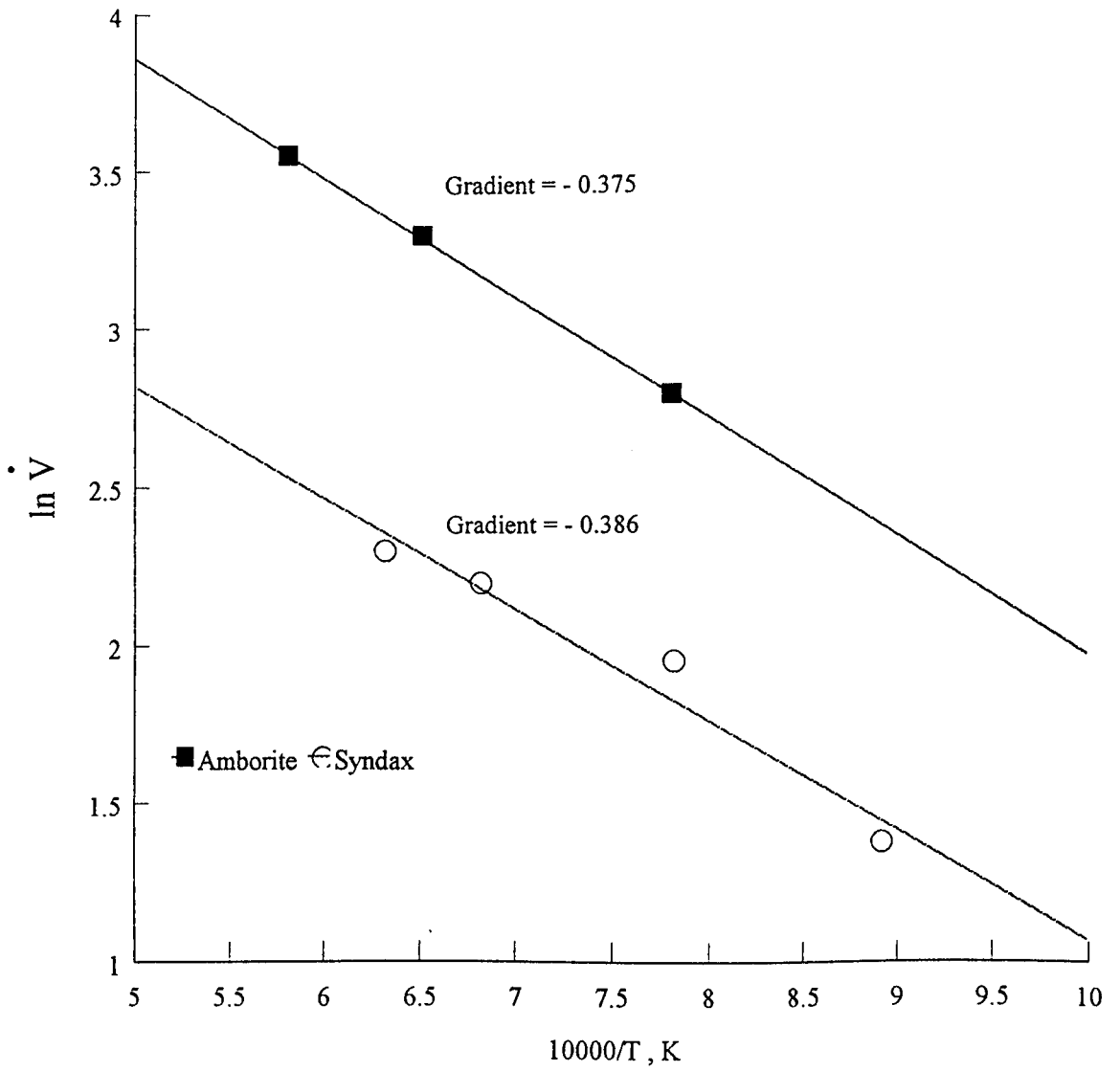


Figure 4.3 Arrhenius plot of volume rate change vs reciprocal of temperature for Amborite and Syndax

4.4.3. Discussion

The activation energies calculated from this experimental work were 0.33 eV (32 kJmol⁻¹) for Syndax and 0.32eV (31 kJmol⁻¹) for Amborite. These values are corresponding to 1.0 RT_m and 1.3 RT_m respectively.

By applying the same experimental technique Brookes (1992) evaluated the activation energies for type Ib synthetic single crystal diamond as 2.92 eV (8.48 RT_m). This value is much higher than the activation energy of Syndax evaluated in this study. This comparison indicates that deformation of the hard particles (diamond crystals) in Syndax have not controlled the creep rate of Syndax under these experimental conditions and suggests that grain boundary mechanisms are more significant. This explanation was supported by the test made on Syndite where no plastic deformation was observed in the temperature range 700°-900°C. Syndite has a very different microstructure than Syndax due to the secondary intergrowth between the diamond particles. This growth has increased the strength of the diamond layer and hence its resistance to plastic deformation. In Syndax, there is no intergrowth between particles, which allows the grain boundary movement to accommodate the stresses generated by the impressor.

Sargent and Ashby (1989) used the data published by Brookes (1984) to calculate an activation energy for single crystals of cubic boron nitride. The value of 2-3 RT_m is comparable with the value determined here for polycrystalline cubic boron nitride. Also, the activation energy for Amborite is comparable with

that evaluated for the same material and reported by Parry (1992) when he used a rigid indenter (i.e. Knoop indenter) to investigate the indentation creep behaviour of Amborite at 1400K and 1600K. To evaluate the activation energy, Parry applied the model developed by Atkins *et al* (1966) (section 4.2 equation 4.10). These observations suggest that the hard particles (cBN crystals) participated in the creep process in addition to AlN and AlB₂ at the grain boundaries. In this respect, it should be noted that Masson *et al* (1992) showed that AlN particles become highly dislocated and cavitation occurred at temperatures of (0.54-0.59T_m) (Section 4.3).

The activation energies measured in this work were obtained in the homologous temperature range 0.3-0.4T_m for Syndax and 0.36-0.5T_m for Amborite. In his review Murgis (1980) indicated certain values of activation energies for some of the mechanisms of creep. For temperatures greater than 0.78T_m the value of Q was given as 19 RT_m, and as 13-14 RT_m for 0.54<T/T_m<0.78. By using the data presented by Atkins *et al* (1966) Murgis plotted two master curves with activation energies of 19 RT_m for temperature greater than 0.78 T_m and 13-14 RT_m for 0.54<T/T_m<0.78. According to these values Murgis suggested that creep by dislocation pipe diffusion is followed at higher temperatures by creep by lattice diffusion. The values of activation energies evaluated in this study are well below the 13-14 RT_m stated by Murgis.

Frost and Ashby (1982) have shown that above (0.3T_m) in metals and (0.4T_m) in ceramic materials, plastic deformation and creep under conditions of uniaxial stress are controlled by the movement of dislocations through the crystal lattice. The rate controlling factor is the energy required for dislocations to move

around obstacles such as inclusion or precipitates etc. Above 0.5-0.6 T_m the glide around obstacles is assisted by dislocation climb and this becomes the deformation rate controlling mechanism. Li *et al* (1991) concluded that for the range of temperature 0.25-0.5 T_m , dislocation glide dominated creep in all the materials they investigated. Whilst there is ample evidence to show that dislocation mobility is sufficient to enable such mechanisms to operate in diamond single crystals at these temperature, the measured activation energies are surprisingly low. More research is required to clarify this aspect of impression creep.

Other aspects of impression creep which need further investigation include the deformation response of cBN impressor on the two materials. In Tables 4.1 and 4.2 the volume, mean pressure and the depths of impressions made by the cBN impressor on Syndax and Amborite have been shown and appear to be quite different. Taking the deformation of both materials at 1000°C as examples, the cBN impressor has shown rapid deformation on Syndax compared with cBN on Amborite. This observation can be monitored from the change in the mean pressure (P_m) and the penetration ability of the impressor on the hard surface (depth). In Syndax P_m dropped from 15.7 GPa at 300s to 8.14 GPa at 3000s. However, in Amborite the change was between 11.49 GPa and 8.66 GPa for the same period of time. Furthermore, the depth of impressions in Syndax was between 3 μ m for 300s and 5 μ m for 3000s. These could be considered as shallow impressions compared with those of the Amborite (i.e. between 9.5 μ m and 14 μ m for the same temperature). Both of the above observations can be related to the impressed surface and the impressor. The mean contact mean pressure

transmitted to the hard surface is directly related to the flow stress of the softer impressor. Thus since Syndax has much higher resistance to plastic deformation than Amborite (i.e. a higher flow stress), the cBN impressor will undergo a greater amount of deformation resulting in a larger change in the mean pressure, and the depth of the impression, between 300s and 3000s.

4.4.4 Summary and Conclusions

The results obtained here show the effect of extended dwell time on the impression of ultra-hard materials at high temperatures, and the following conclusions can be drawn:

1. The impression volume for both materials has increased with the increase in dwell time. This increase has enhanced the possibility of using the soft impression technique as an alternative to conventional testing methods (standard uniaxial techniques) in investigating the high temperature creep properties of advanced ceramic materials.
2. In both materials investigated in this work, the overall creep (volume change) appears to be accommodated by the matrix materials (the second phase) rather than the hard particles. The same experimental technique was applied on Syndite which has a totally different microstructure (complete intergrowth between particles) at temperatures between 700°-900°C, resulting in no signs of material displacement or volume change. This suggests that the contribution of the hard particles, diamond and cBN to the overall creep is minimal. However, the signs of plastic deformation within the hard particles

under the impressor cannot be ruled out since the applied mean pressure is comparable to that of the sintering process.

3. Wang (1994) reported that the activation energy of SiC (second phase in Syndax) is between 1.51-3.12 eV in a similar temperature regime (1000°-1200°C), using bending and compression measurements. This suggests that the calculated activation energy from the data presented in this chapter is low and does not provide any indication of which mechanism controls the time dependent increase in the volume of impressions.

4. Whilst further work is required to identify the mechanisms which control impression creep, it has been shown consistently that this phenomenon is observed whenever the temperature is above the BDT and the mean contact pressure is in excess of that required to produce dislocation movement and plastic flow in cBN and Syndax.

Chapter 5 The friction and wear due to softer sliders on cBN, PCD and diamond

5.1 Introduction

Polycrystalline diamond and polycrystalline cBN are mainly produced as tool materials for the shaping of hard metals and composites. Thus, their sliding friction and wear resistance are amongst the most important properties relevant to those applications. Similar to other mechanical properties, the frictional properties of polycrystalline ultra-hard materials will differ according to the type of composite as well as the experimental (or the application) conditions. The friction and wear properties of these polycrystalline materials are strongly influenced by the binder phase, e.g. it may adhere to the other contacting surface. Therefore, a direct comparison between the frictional behaviour of single crystals and their polycrystalline composites may not be entirely valid.

In this work, the actual conditions of metal cutting processes have been simulated in order to evaluate and compare the performance of polycrystalline diamond and cubic boron nitride. The behaviour of a selection of diamond and cubic boron nitride based materials, representing two polycrystalline diamond composites (Syndite and Syndax), a CVD-coated product (CVDite) and polycrystalline cubic boron nitride (Amorite) when subjected to cumulative frictional deformation beneath softer sliders is compared and contrasted. All of these hard materials have significant present and/or future applications as tool

materials in metal forming operations. The softer slider cones were made from a range of metals representative of those commonly shaped with diamond tools.

5.2 Friction and wear of polycrystalline ultra-hard materials

During cutting by PCD and cBN the wear mechanism is mostly influenced by the chemical affinity between the tool material and the workpiece. For example, diamond based materials are not recommended for machining ferrous materials because carbon is highly soluble in iron. This leads to the graphitisation of diamond and hence a high rate of diffusion wear, due to carbon solution in iron, is observed (Brookes and Lambert, 1982).

Similarly, Hooper *et al* (1988) described the wear of cubic boron nitride tools as being due to chemical wear caused by the interaction between the insert and its environment - i.e. this includes the workpiece and the atmosphere. In that work, it was shown that atmospheric oxidation, combined with the development of a high density of dislocations, resulted in etching wear of the compact cBN tool. Another feature observed was the formation of a protective layer on the rake face of the cutting tool and this was shown to be a major factor in limiting tool wear. At lower speeds and temperatures, the layer became less stable and hence was removed by the chip, taking away with it small fragments of the tool and exposing the tool surface to further chemical and attrition wear. These conditions resulted in an unsatisfactory performance of the cutting tool materials. König and Neise (1993) tested the diffusional wear of PCD (with cobalt binder) with Ti-Al6-V4 as the workpiece at 700°C. They reported two kinds of

thermally induced damage. First, the formation of cracks seemed to be caused by thermally induced stresses. These stresses were thought to be created by the mismatch of the thermal expansion coefficients of cobalt and diamond, which also had been reported earlier by H. Takayema *et al* (1984). Secondly, degradation occurred due to the graphitisation of the diamond particles with the help of cobalt (as catalyst) at temperatures above 700°C. König and Neise concluded that the amount of wear was dependent on the percentage of the binder content - a low percentage minimised the graphitisation process and hence improved the performance. The wear process was also dependent on the grain size of the diamond particles, i.e. the larger the diamond particles, the higher the thermal stability of the cutting tool.

In another test, these authors repeated the same experiment with PcBN (85-90% cBN content) with a bearing steel (100Cr6) as the workpiece at 950°C and concluded that the thermally induced recrystallisation of the binder phase component was the dominant wear mechanism of the PcBN.

Feng and Haywood (1988) studied the behaviour of various metallic styli sliding on Syndite specimens. The styli of tungsten carbide, cobalt, copper and other materials were in the form of cones with a 90° included angle. The experimental conditions involved a sliding speed of 100 mm/s and a load of 0.5 N. They observed that the lowest coefficient of friction, i.e. 0.3, resulted from the cobalt sliding on Syndite, compared with 0.71 for copper sliding on Syndite. They also showed that the coefficient of friction between cobalt sliding on cobalt was, surprisingly, lower than cobalt on Syndite. They explained this observation by suggesting that the low value of the coefficient of friction was due to the

formation of a protective oxide layer, reducing the adhesion, whereas the hard asperities of Syndite prevented the formation of a complete layer. If the above experiment (metallic styli on Syndite) had been performed at high temperature, the graphitisation of diamond would dominate the wear process by creating extensive cracks on the tool face.

Freeman and Field (1989) investigated the frictional behaviour of diamond, Syndite and Amborite styli (in the form of a Knoop indenter) against annealed D3A steel (containing 2.25% C, 12%Cr). The coefficient of friction for diamond, after 20 cycles, was the lowest - i.e. 0.1 compared with 0.19 and 0.39 for Syndite and Amborite respectively. The relatively high friction of polycrystalline diamond was mainly due to the transfer of steel to the slider, whereas the transfer onto the diamond single crystal was negligible. Also, they repeated this set of experiments with hardened D3 steel (D3H) which was three times harder than D3A. After 20 cycles the coefficient of friction dropped to ≈ 0.05 for diamond and was unchanged for Amborite and Syndite. The decrease in friction in the case of diamond was related to the decrease in the ploughing component of the total friction force. The Amborite, Syndite and diamond styli showed no wear.

Mehan and Hayden (1981) observed the friction of PCD materials sliding on steel and reported the coefficient of friction of 0.15 for the ground surface of PCD. This value is comparable with 0.19 reported by Freeman and Field (1989). However, it is not expected that the level of wear and the frictional behaviour of hard materials, such as a PCD slider sliding on a relatively soft material, such as steel, would be similar to friction of steel sliding on PCD. This is due to the

difference in hardness which has a significant effect on the nature of contact and subsequent mechanism of deformation- i.e. a hard slider ploughs into a softer surface resulting in a high coefficient of friction due to the extensive deformation and penetration of the surface; whilst a soft slider adheres to a hard surface resulting in a high coefficient of friction (μ) due to the adhesion forces (Wilks and Wilks 1991).

The frictional behaviour of diamond coating is affected by its mechanical and chemical properties; microstructure; and the experimental temperature. The influence of surface microtopography, grain boundaries and the coating-substrate adhesion also has significant impact on the coating behaviour. For example, the coating-substrate system must be considered as a whole unless it can otherwise be established that the friction in a particular case is independent of the substrate material. This includes substrate effects on the growth morphology (Chapter 1) and the stress state of the coating (due to the mismatch in contraction resulting from the difference in thermal properties of the coating and the substrate). Therefore, comparison between the frictional behaviour of various diamond coatings is very difficult since all of the above factors are not usually standardised.

Okada and Namba (1989) found that the coefficient of friction was 0.2 in vacuum and 0.15 in air for pure copper sliding on plasma vapour deposition (PVD) diamond coatings. They used normal loads which varied between 0.3 and 2.94N on a pin-on-disk apparatus at sliding speed of 30 mm/s. Miyoshi *et al* (1993) reported friction experiments in humid air, dry nitrogen and in vacuum of microwave-plasma-deposited diamond coatings on silicon substrates, in contact

with a natural diamond pin. A range of experiments was conducted to study the influence of the surface roughness (ranging from 15-160 nm) on sliding contact behaviour. Experiments were made with sliding velocity of 1.43 mm/s, a track length of 3 mm load of 1N and the experiment was conducted for 17.4 h. They found that the initial and equilibrium coefficient of friction were independent of the initial surface roughness of the diamond coatings. The equilibrium coefficients of friction (μ) were 0.02-0.04 in humid air and in dry nitrogen, but 1.5-1.8 in vacuum. The high friction in vacuum was considered to be due to the removal of the contaminant surface layer by repeatedly sliding the pin over the same track in vacuum, with a consequent increase in adhesion - as in the work of Bowden and Hanwell (1966).

In this thesis the frictional behaviour of cBN (Amorite) and PCD materials (Syndite, Syndax and CVDite) have been studied when subjected to the sliding of softer sliders (metallic and ceramic). For reasons of comparison, the same technique has been applied to investigate the frictional behaviour of type I diamond single crystal on the (001) face.

5.3 Experimental procedure

Amorite, Syndax, Syndite, CVDite and diamond specimens were investigated under the action of reciprocating sliding. A group of metallic and ceramic materials was selected to be used as sliders (initially cones shaped with an included angle of 120°). These materials were selected to provide a range of hardness from Hk_{200} 1.1 GPa (aluminium) to $Hk_{200} = 3.2$ GPa (titanium alloy).

The ceramic sliders were TiB₂ and cBN with Knoop hardness (Hk₅₀₀) of 13 and 38 GPa respectively.

The tests were carried out in air and also in vacuum. The normal load used for the sliding friction and wear tests was 100N, the sliding speed was 0.1mm/s and the length of each track was about 3mm. To remove the surface contaminants, the specimen and the slider were cleaned ultrasonically in acetone for 15 minutes. The adsorbed surface layers on diamond, Syndax, CVDite and Amborite specimens were removed by heating the specimens in vacuum for 30 minutes at 1000°C. However, a temperature of 700°C for 45 minutes was used for the Syndite specimen because of its thermal instability at higher temperatures. After the out-gassing of the specimen surface, the experiment was started by applying the load onto the cone to blunt its tip before sliding. The cone was then moved to another position and the friction force was measured over the first reciprocating traversal. When the coefficient of friction was low and there was no significant transfer of the slider material, further traversals were carried out. In those cases, continuous friction measurements were made for tracks of 10, 100, 1000 and 3500 traversals. The resultant tracks were examined using optical and scanning electron microscopy and their dimensions were determined using a Taylor-Hobson Talysurf Series 50.

◆ Effective and apparent mean pressure

When a slider was first loaded against a harder specimen surface, the tip was blunted by plastic flow and the resultant circular area of contact increased until it was sufficient to support the applied load elastically. By dividing the applied load by this contact area an *effective* mean pressure (P_m), which is directly related to

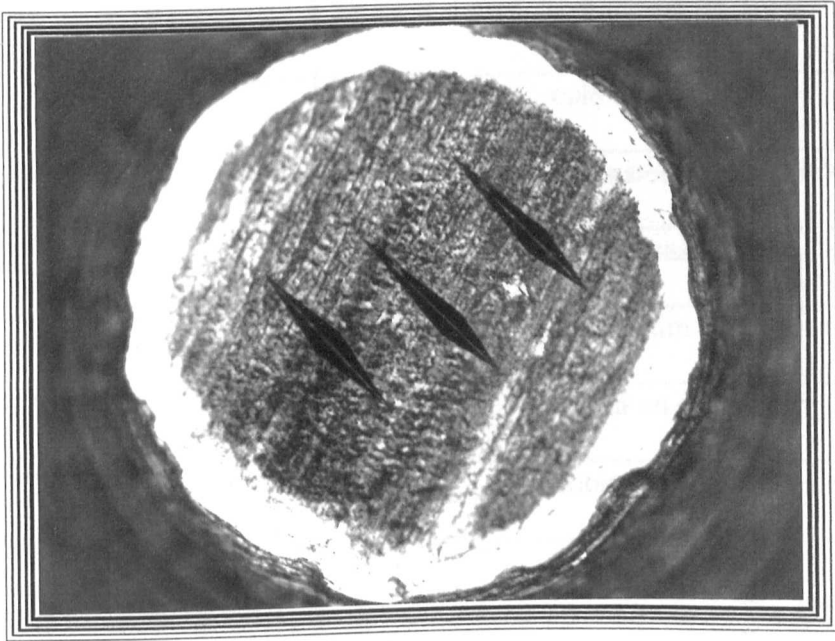
the indentation hardness of the material from which the cone is made, was determined and is shown for a variety of materials in Table 5.1.

Table 5.1 The effective mean pressure produced by softer sliders and the original and the work-hardened values of the Knoop hardness of the same sliders

	sliders						
	Al	Cu	N [*]	M.S.	TA45	TiB ₂	cBN
P _m (effective) GPa	1.10	0.94	1.90	1.85	2.70	-	-
H _k (original), GPa	1.10	1.10	2.3	2.2	3.2	13	38
H _k (deformed tip), GPa	1.45	1.28	2.55	2.78	3.98	13	38

In addition to the effective mean pressure and the Knoop hardness of the sliders, Table 5.1 contains the hardness of the work-hardened cones (blunted tips) which were measured using a Knoop indenter with 200gf load (Figure 5.1).

The *apparent* mean pressure was evaluated by dividing the applied load by the resulting contact area of the tip after the sliding process. The value of the apparent mean pressure was normally less than the effective mean pressure due to the increase in apparent contact area with sliding. The softer sliders used in this work and the relevant identification symbols are as follows:



100 μ m

Figure 5.1 A flattened tip of a metallic cone with Knoop indentations to monitor the change in hardness

Symbol	Materials
Al	aluminium-magnesium alloy
Cu	pure copper
Brass	brass (70:30 Cu-Zn)
N*	nimonic 75
M.S.	mild steel (0.2%C)
S.S.	stainless steel (austenitic)
C.I.	gray cast iron
TA45	titanium alloy
TiB ₂	titanium diboride
cBN	cubic boron nitride

5.4 Results

5.4.1 Friction of softer sliders - single traversal

(a) Single crystal and CVDite

The coefficient of friction (μ) of the softer sliders on CVDite and diamond measured in vacuum and in air are presented in Table 5.2 and plotted in Figure 5.2. The values of the coefficient of friction between the softer sliders and CVDite in vacuum and in air were relatively similar i.e. change in environment had little effect on the frictional behaviour of these sliders on CVDite. For most metallic sliders on CVDite, μ was in the range of 0.1-0.19 and there was no material transfer involved during the sliding. The exception was the titanium

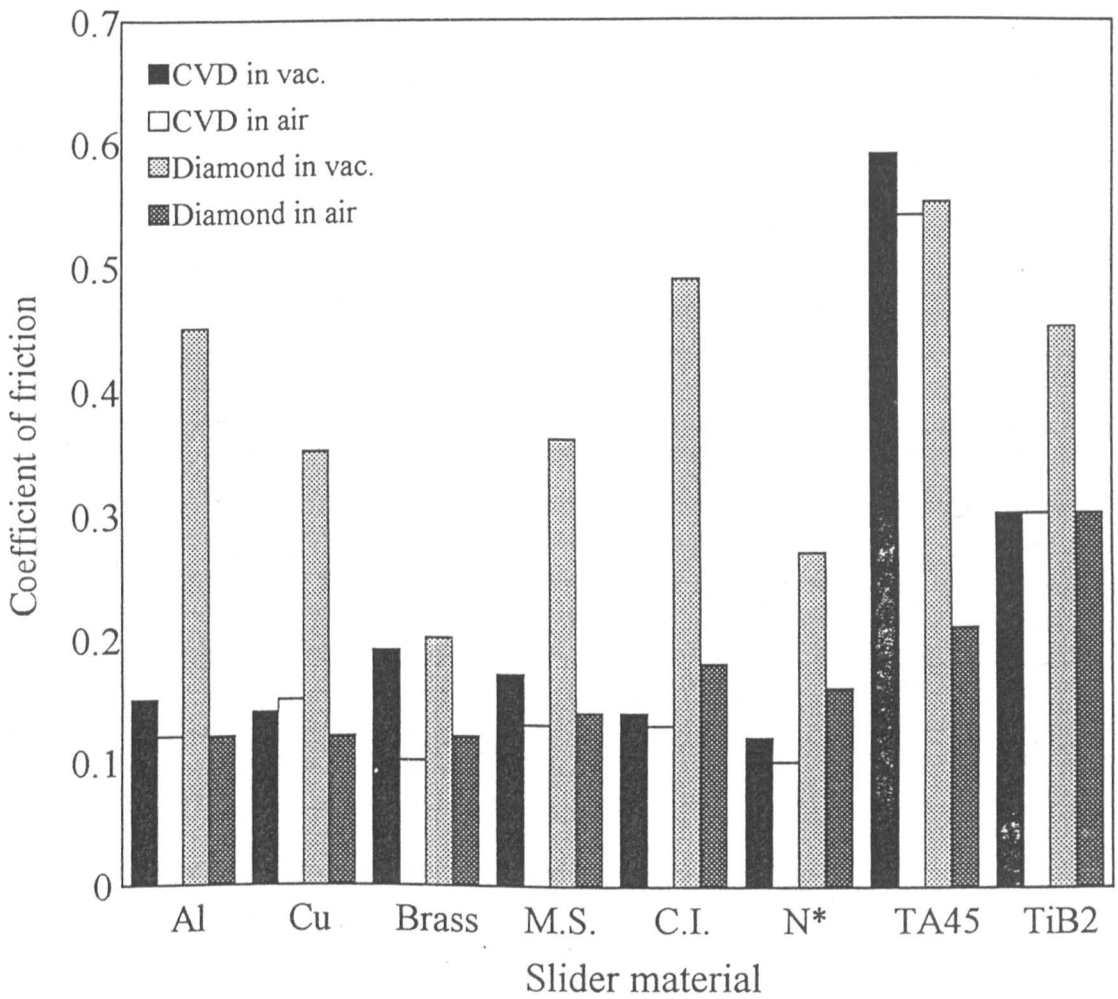


Figure 5.2 The coefficient of friction developed between softer sliders and CVDite and single crystal diamond

alloy (TA45) slider which developed a high coefficient of friction resulting from heavy material transfer on to the diamond surface.

Table 5.2 The friction of softer sliders on CVDite and diamond

	CVDite in air	CVDite in vac.	Diamond in air	Diamond in vac.
Al	0.12	0.15	0.12	0.45
Cu	0.15	0.14	0.12	0.35
Brass	0.1	0.19	0.12	0.2
M.Steel	0.13	0.17	0.14	0.36
C.Iron	0.13	0.14	0.18	0.49
N [*]	0.1	0.12	0.16	0.27
TA45	0.54	0.59	0.21	0.55
TiB ₂	0.3	0.3	0.3	0.45

In air, the coefficient of friction developed by this range of soft sliders on type I_a diamond was similar to that of CVDite, with the exception of TA45. In contrast, generally, the friction increased sharply for all the sliders on single crystal diamond in a vacuum. Again the coefficient of friction measured using the titanium alloy as sliders, was high due to the severe adhesion which occurred between the slider and diamond.

(b) Polycrystalline diamond and CVDite

The coefficient of friction was measured using a selection of sliders on polycrystalline diamond-Syndite and Syndax. Table 5.3 and Figure 5.3 show the coefficient of friction results for Al, mild steel, TA45 and TiB₂ sliders compared with results obtained during sliding on CVDite.

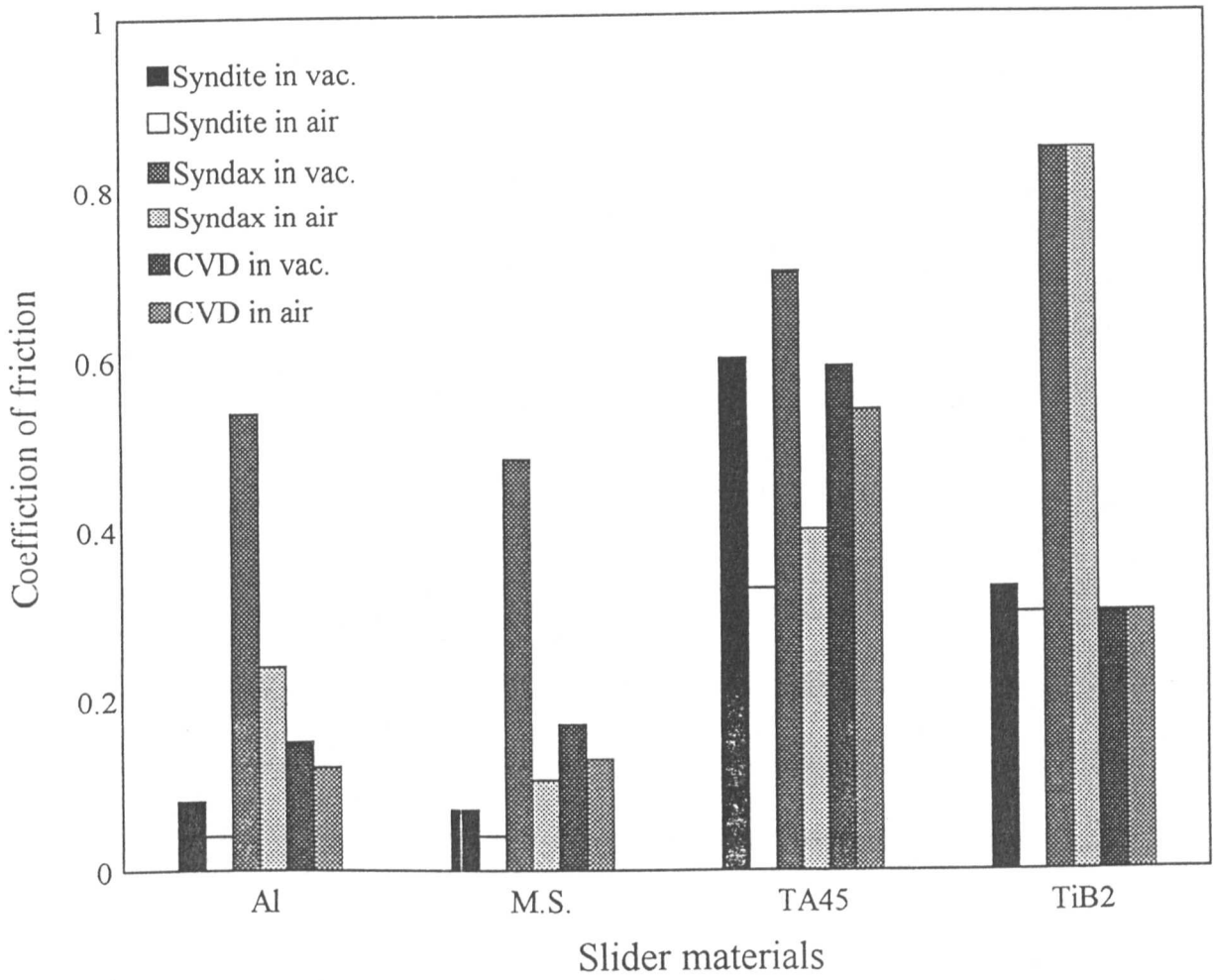


Figure 5.3 The coefficient of friction developed between soft sliders and polycrystalline diamond

Table 5.3 Comparison of the friction results of softer sliders on various types of polycrystalline diamond

	Syndite in vac.	Syndite in air	Syndax in vac.	Syndax in air	CVDite in vac.	CVDite in air
Al	0.08	0.04	0.54	0.24	0.15	0.12
M.Steel	0.07	0.04	0.48	0.105	0.17	0.13
TA45	0.6	0.33	0.7	0.4	0.59	0.54
TiB ₂	0.33	0.3	0.84	0.84	0.3	0.3

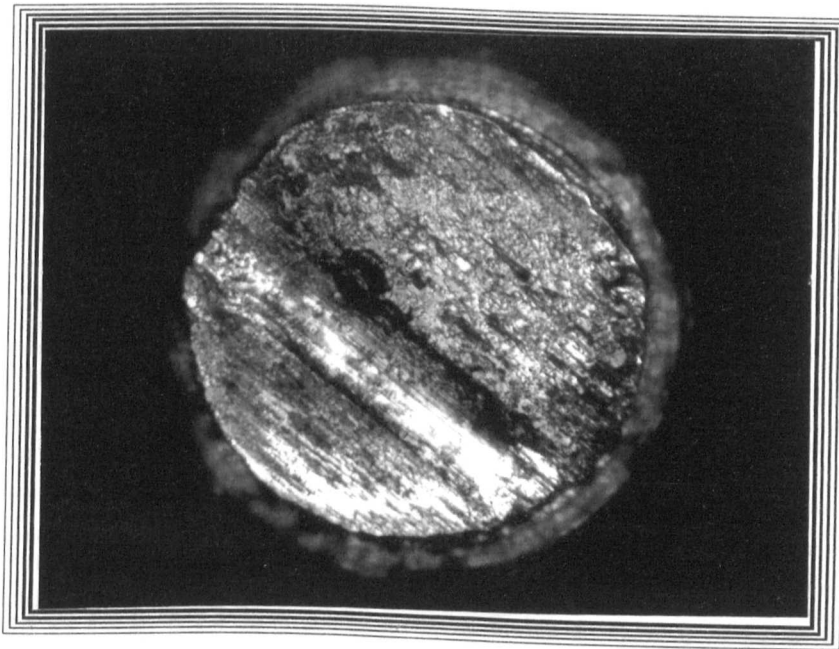
The aluminium and mild steel sliders developed a low coefficient of friction on Syndite in both air and in a vacuum, with no sign of adhesion. However, different behaviour was observed between those sliders and Syndax, where considerable transfer of metal to the Syndax surface occurred from both materials (see Figure 5.4 (a) and (b)) which resulted in a high value of the coefficient of friction. Furthermore, the coefficient of friction using a titanium diboride (TiB₂) slider on diamond materials is higher than the coefficient of friction developed using metallic sliders.

(c) Cubic boron nitride (cBN)

The coefficient of friction of softer sliders on cBN was much higher in a vacuum compared with those in air. The values of μ are given in Table 5.4 and plotted in Figure 5.5. The values of the coefficients of friction are high for all metallic sliders on cubic boron nitride in vacuum compared with air. Severe adhesion was observed between Al and TA45 sliders and the cBN. However the other metallic sliders developed adhesion after multiple passing of the slider and so cumulative deformation measurements were not made.



Figure 5.4 (a) Adherent aluminium on polycrystalline diamond (Syndax)



100µm

Figure 5.4 (b) Sheared tip of the aluminium cone used above

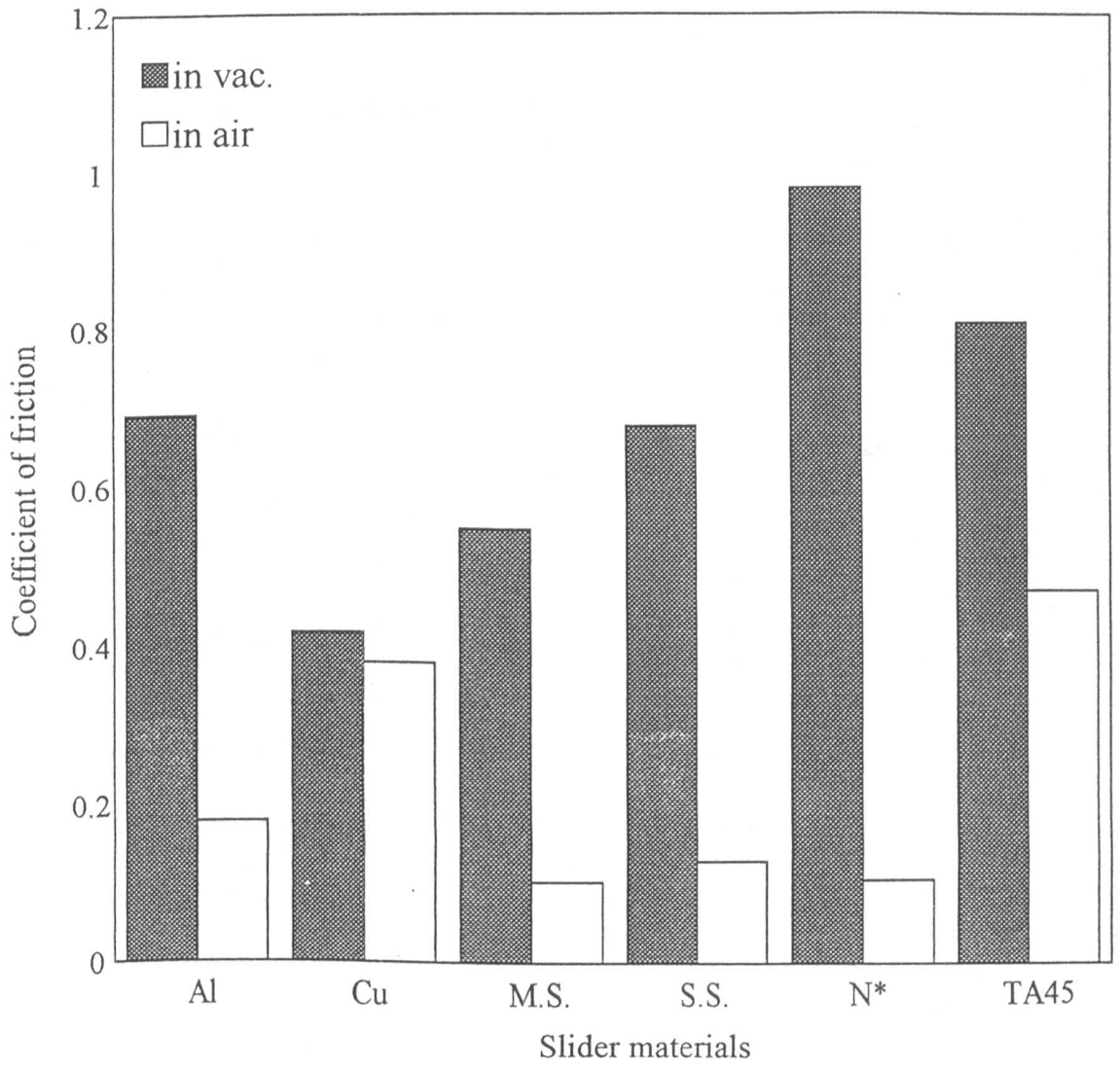


Figure 5.5 The coefficient of friction developed between soft sliders and cBN

Table 5.4 The friction results of softer sliders on cBN

	In vac.	In air
Al	0.69	0.18
Cu	0.42	0.38
M. steel	0.55	0.105
S. steel	0.68	0.13
Ni75	0.98	0.107
TA45	0.806	0.47

5.4.2 Friction and wear of PCD due to multiple traversals

(a) Friction and wear of CVDite

The results obtained for two metal sliders and TiB₂ on CVDite in a vacuum using multiple traversals, to produce cumulative damage, are presented in Table 5.5. This table shows that the coefficient of friction increased with increasing number of traversals for the aluminium and mild steel sliders. Multiple traversals were possible due to the lack of adhesion between aluminium and mild steel sliders and CVDite. After 100 traversals a trace (a line in the middle of the track with no depth) was detected. When the number of traversals was increased to 1000, a groove with measurable depth was developed. This depth was then increased with increasing traversal numbers.

Table 5.5 Friction and wear of CVDite

sliders	traversal	μ	wear/depth (μm)
Al	1	0.15	polished track
	10	0.17	polished track
	100	0.19	trace
	1000	0.3	groove with 0.3 μm depth
	3500	0.26	groove with 0.8 μm depth
M.S.	1	0.15	polished track
	10	0.17	polished track
	100	0.18	trace
	1000	0.39	groove with 0.3 μm depth
	3500	0.48	groove with 1.5 μm depth
TiB₂	1	0.45	polished track
	10	0.35	trace
	100	0.27	groove with 0.1 μm depth
	1000	0.35	groove with 0.3 μm depth
	3500	0.23	groove with 0.6 μm depth

However, for TiB₂ the coefficient of friction decreased whilst observable wear was obtained after only 100 traversals. This compares with the wear caused by the metallic sliders where 1000 traversals were required to develop observable wear. After 100 traversals, a groove of 0.1 μm was developed by the TiB₂ slider which subsequently increased with increasing numbers of traversals. However, after 3500 traversals, the depth of the track developed by the ceramic slider (TiB₂) was 0.6 μm which is shallower than that developed by the metal sliders (1.5 μm in the case of mild steel). Figure 5.6 (a) shows a typical wear track made by TiB₂ on CVDite, after 3500 traversals and details of the structure inside the groove are shown in Figure 5.6 (b). Similarly, Figure 5.7 shows a groove in CVDite made by the mild steel slider after 3500 traversals.



Figure 5.6 (a) Wear track produced by TiB₂ slider on CVDite after 3500 traversals

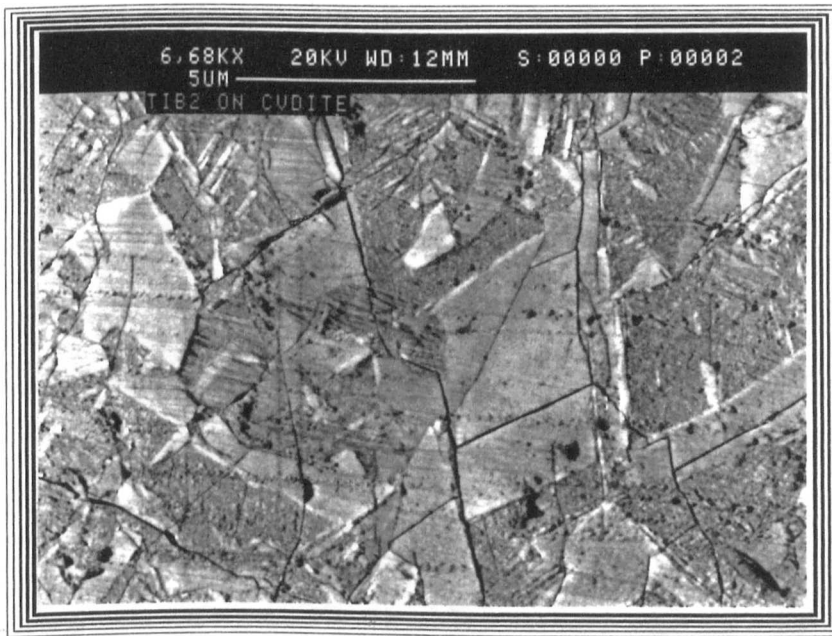


Figure 5.6 (b) High magnification of the above track showing the formation of cracks

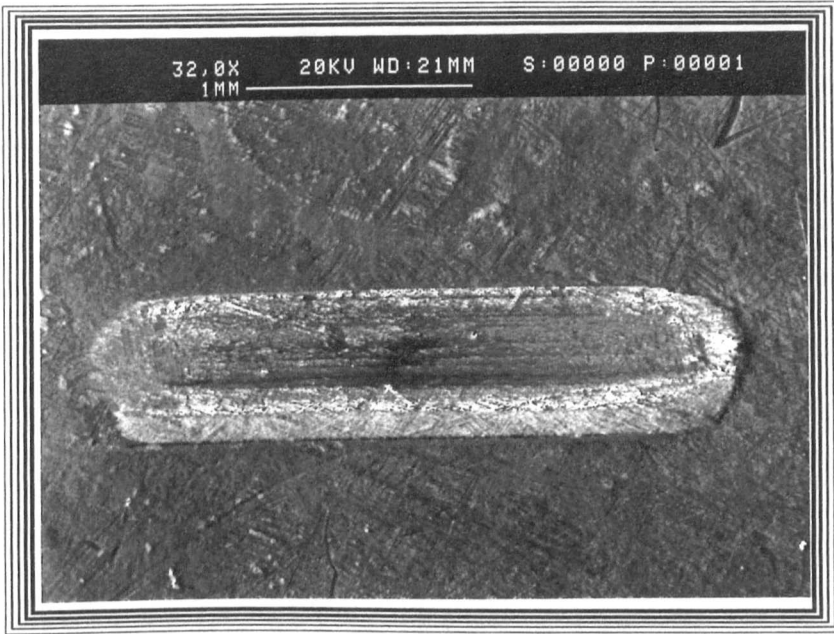


Figure 5.7 (a) Wear track produced by mild steel slider on CVDite after 3500 traversals

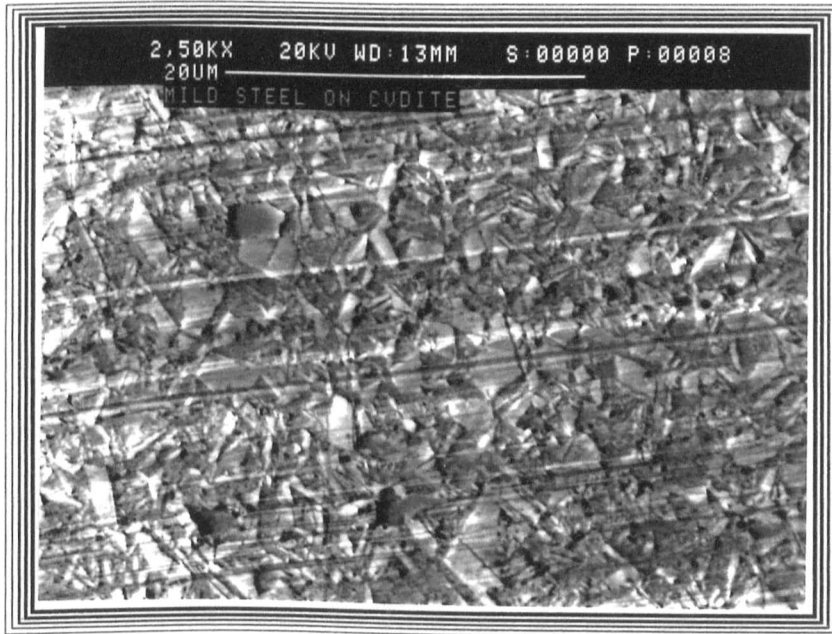


Figure 5.7 (b) High magnification of the above track showing the formation of cracks in the diamond particles

(b) Syndax

Table 5.6 summarises the full set of friction results obtained for metallic and ceramic sliders on Syndax under the same cumulative damage conditions of multiple traversals.

Table 5.6 Friction and wear of Syndax

sliders	traversals	μ	P_m (GPa)	Wear
Al	10	0.54	0.35	Very strong adhesion which resisted ultrasonic cleaning with acetone
M.Steel	10	0.48	0.6	Very strong adhesion which resisted ultrasonic cleaning with acetone
TiB ₂	1	0.84	1.17	no wear
	10	0.657	1.07	no wear
	100	0.60	0.93	trace of wear
	1000	0.090	0.9	0.3 μ m depth track
	3500	0.075	0.63	0.5 μ m depth track
cBN	1	0.63	4	trace of wear
	10	0.76	2.3	trace of wear
	100	0.78	2.04	trace of wear
	1000	0.855	1.3	plucking of the diamond particle - strong adhesion

As mentioned earlier, aluminium and mild steel sliding on Syndax resulted in large-scale transfer of metal to the Syndax surface. The transferred metal, which resisted ultrasonic cleaning with acetone, appears to have protected the hard surface from cumulative deformation. Therefore, no further wear experiments were conducted with these particular metals.

Generally, in the case of the TiB₂ slider, the apparent mean pressure and the coefficient of friction decreased with increasing traversals. Evidence of wear was first observed after 1000 traversals, when a groove 0.3 μ m in depth was developed. Increasing the number of traversals resulted in more deformation and

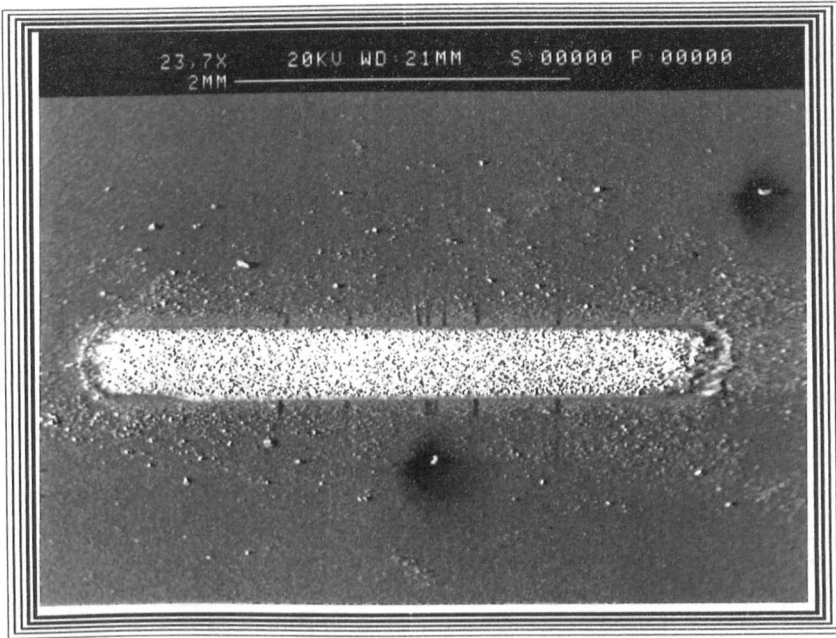


Figure 5.8 (a) Wear track produced by TiB_2 slider on Syndax after 3500 traversals



Figure 5.8 (b) High magnification of the above track showing the formation of cracks in the diamond particles

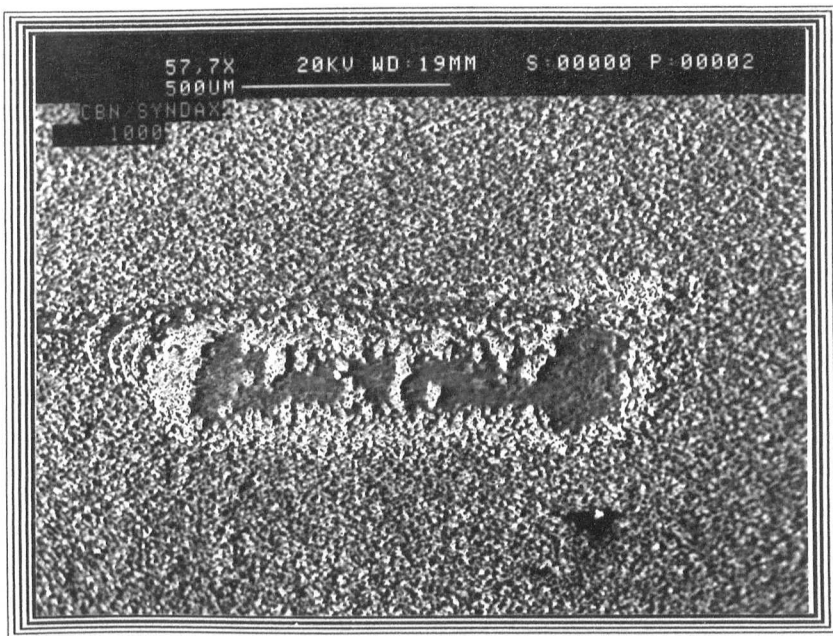


Figure 5.9 (a) Wear track produced by cBN slider on Syndax after 1000 traversals, large scale transfer was observed

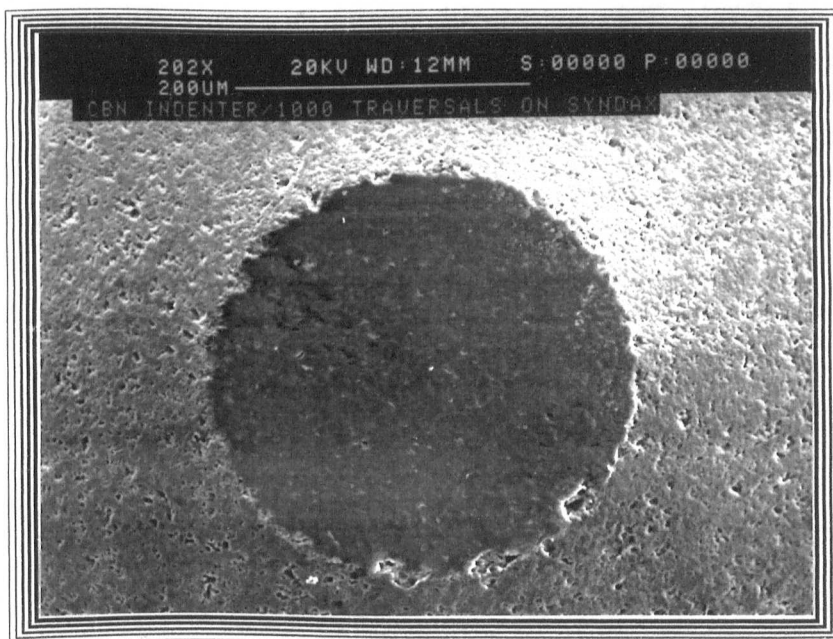


Figure 5.9 (b) The flattened tip of the cBN slider

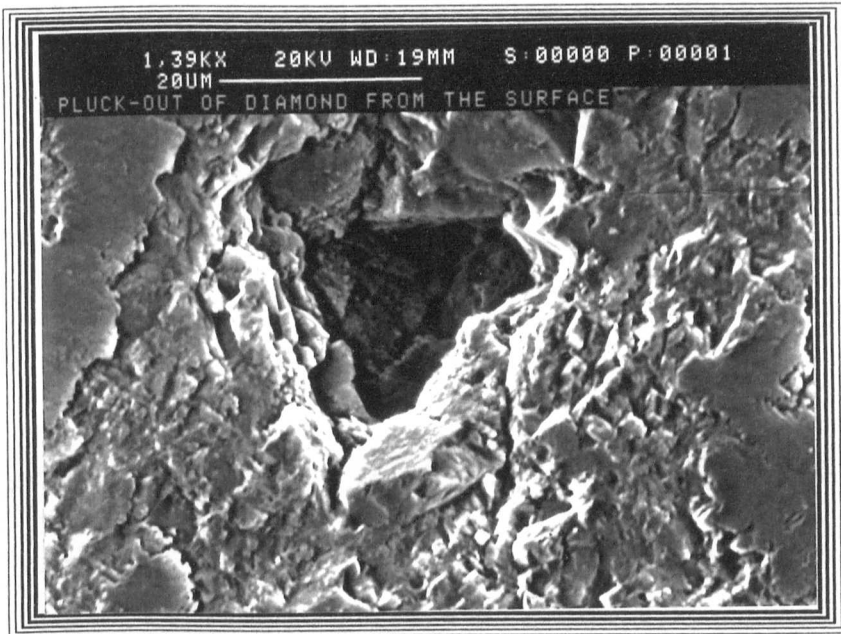


Figure 5.10 High magnification of the cBN track on Syndax showing the pluck-out of the diamond particles from the surface

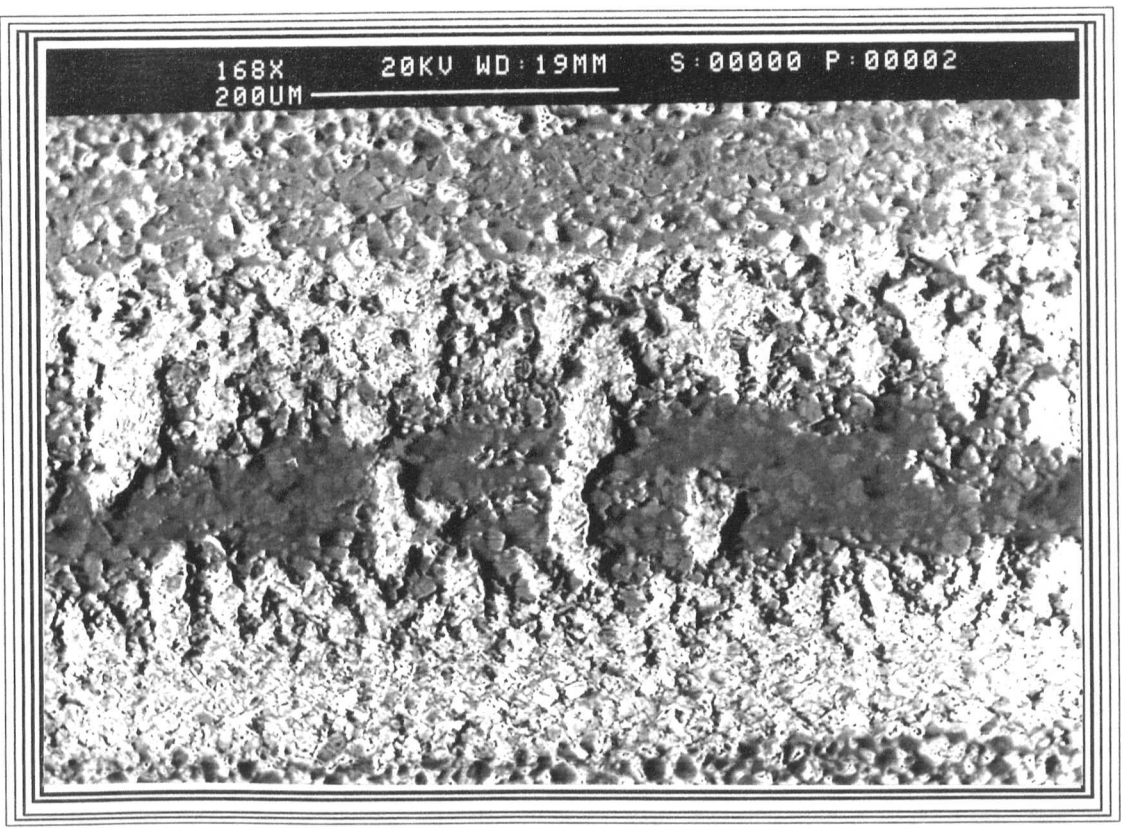


Figure 5.11 (a) Section of the cBN track on Syndax

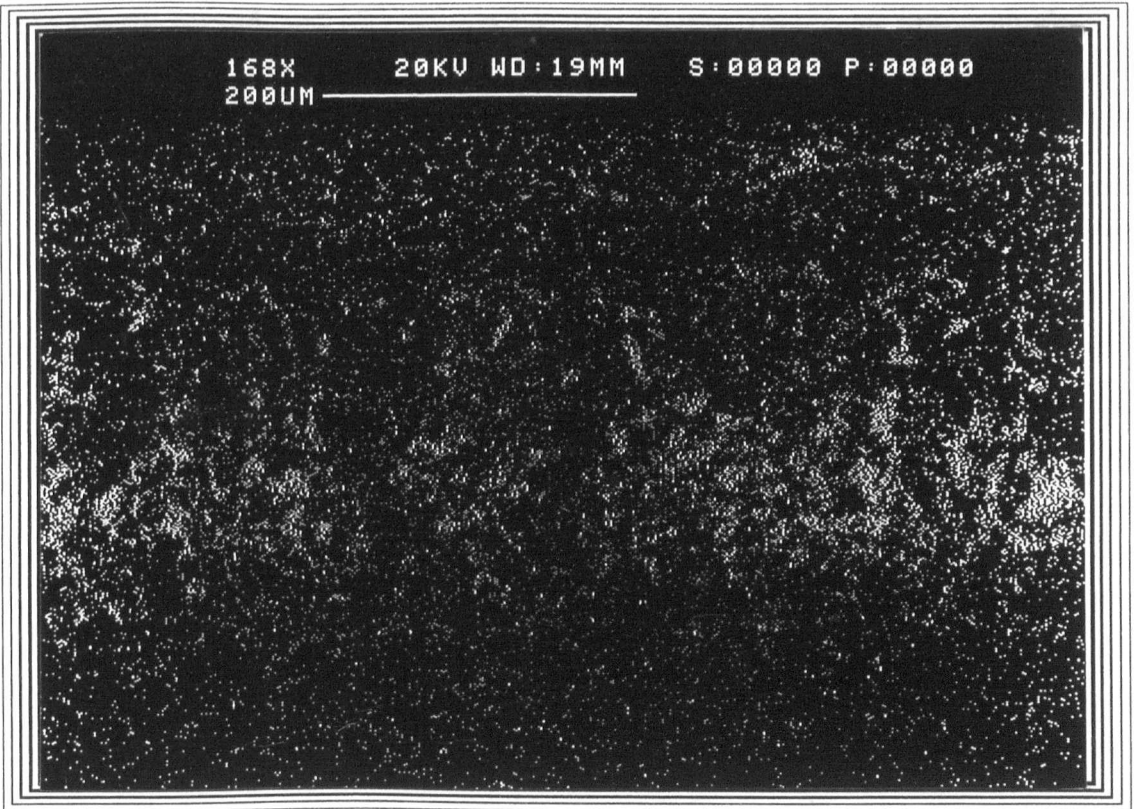


Figure 5.11 (b) The aluminium dot map of the track shown above

an increased depth of track to $0.5\mu\text{m}$, with no evidence of adhesion. Figure 5.8 shows the groove developed after 3500 traversals of the TiB_2 slider on Syndax. Note the intersection of the transparticle crack network within each particle. Figure 5.9 (a) shows a track in Syndax made by cBN after 1000 traversals. Note the smooth and round tip of the cBN slider shown in Figure 5.9 (b). When the cBN slider was used against Syndax, diamond particles were plucked out (Figure 5.10) and adhesion between cBN and Syndax occurred after 100 traversals. Figure 5.11 (a) shows a section of the track made by a cBN slider - the dark area in the middle of the track is the adhered cBN materials which were verified by the aluminium dot map in Figure 5.11 (b) (the aluminium signal is associated with cBN). In this case, the coefficient of friction increases and the mean pressure decreases. After 1000 traversals the cubic boron nitride slider was fractured due to the strong adhesion.

(c) Syndite

As with CVDite, the behaviour of the metallic sliders on Syndite (where there was no transfer of material to the diamond surface) gave the opportunity to investigate the cumulative frictional deformation caused by aluminium and mild steel sliders after multiple traversals. Table 5.7 summarises the full set of frictional results obtained for those sliders in addition to TiB_2 and cBN on Syndite specimens under these conditions.

Table 5.7 Friction and wear of Syndite

sliders	traversal	μ	P_m (GPa)	Wear/depth
Al	1	0.11	0.6	-
	10	0.045	0.596	polished track, no depth
	100	0.045	0.55	polished track, no depth
	1000	0.045	0.53	polished track, no depth
	3500	0.06	0.49	polished track, debris on the tip of the slider
	6500	0.06	0.476	polished track, debris on the tip of the slider
M.S.	1	0.13	1	polished track, no depth
	10	0.045	0.92	polished track, no depth
	100	0.045	0.86	polished track, no depth
	1000	0.045	0.67	polished track, no depth
	3500	0.03	0.54	polished track, no depth
TiB ₂	1	0.33	3.5	polished track, no depth
	10	0.21	2.04	polished track, no depth
	100	0.09	1.4	polished track, no depth
	1000	0.09	0.88	trace
	3500	0.09	0.63	1 μ m groove
cBN	1	0.42	4.4	trace
	10	0.2	2.9	trace
	100	0.3	2.2	0.3 μ m groove
	1000	0.63	1.3	0.6 μ m groove

The friction between aluminium and mild steel sliders and Syndite was lower than that on CVDite. Increasing the number of traversals from 1 to 10 resulted in a sharp decrease in the coefficient of friction from 0.11 to 0.045. Then the coefficient of friction and the mean pressure were monitored for 100, 1000, 3500 (and 6500 in the case of the aluminium slider) traversals. There was no change in the value of μ or mean pressure for these experimental conditions - with the exception of a slight increase in the coefficient of friction after 3500 traversals with aluminium sliders. The multiple sliding of aluminium and mild steel sliders on Syndite caused only superficial polishing of the harder surface. However, there was evidence of an accumulation of a layer of wear debris on the tip of the



Figure 5.12 Debris layer formed on the blunted tip of an aluminium slider after 6500 traversals on Syndite

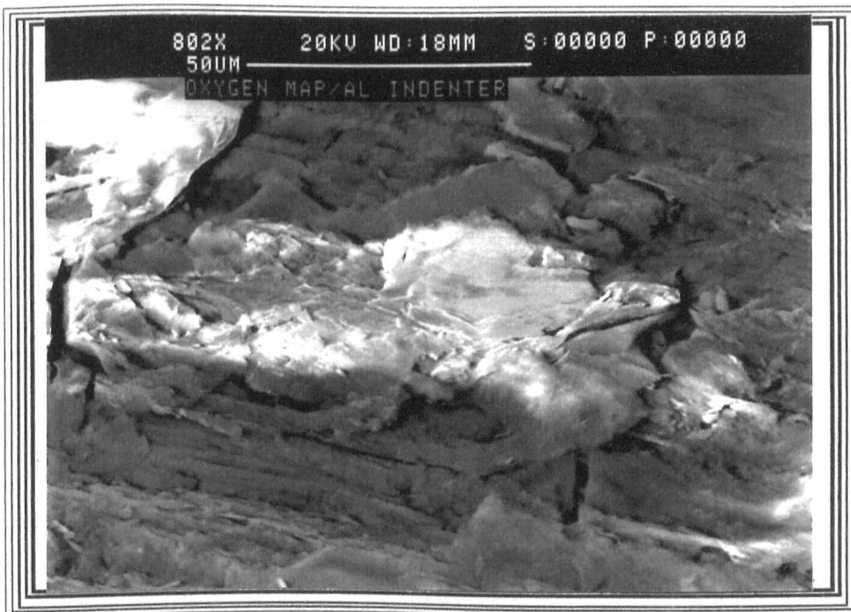
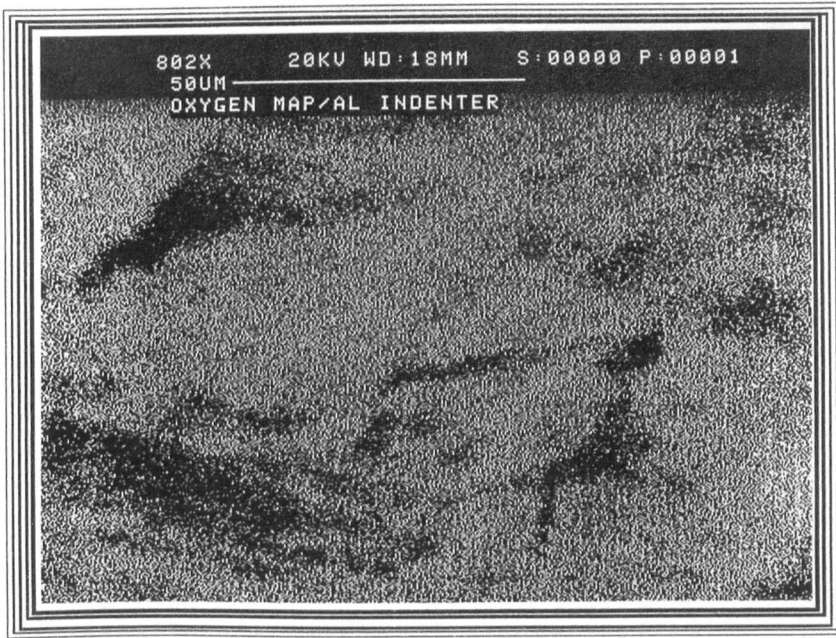


Figure 5.13 High magnification of the layer formed on the blunted tip of the aluminium slider after 6500 traversals on Syndite

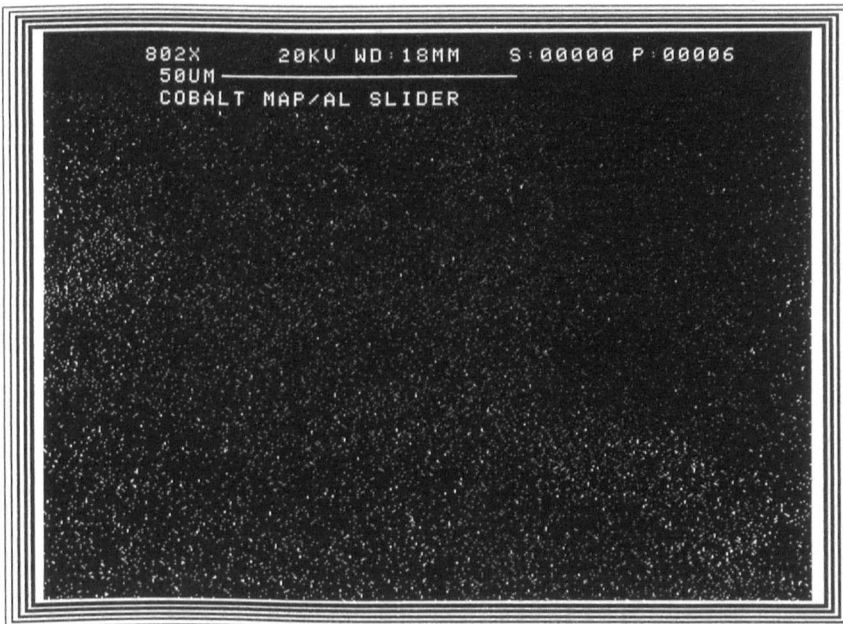
aluminium slider (Figure 5.12). Although mild steel showed the same behaviour as aluminium in terms of the coefficient of friction, this layer was detected only with aluminium sliders. Figure 5.13 is a high magnification micrograph of the layer formed on the aluminium slider. Analysis of this layer, using an electron dispersive analysis attachment for the scanning electron microscope, showed that oxygen (Figure 5.14 a) and cobalt (Figure 5.14 (b)) were present. Also, a very low level of carbon was detected. Figure 5.15 (a) shows the micrograph of one end of the track formed by the aluminium slider on Syndite after 500 traversals. The analysis of the accumulated debris shows that aluminium was present at a high level (Figure 5.15 b). Unlike CVDite, there was no evidence of groove formation even after 6500 traversals, when aluminium and mild steel sliders were used.

The value of the coefficient of friction of the TiB_2 slider on Syndite ($25\mu\text{m}$ particle size) was lower than that measured on CVDite. However, wear was first observed after 1000 traversals when a track with undetectable depth appeared (observed by optical microscope as a line in the middle of the track). This track developed into a groove, $1\mu\text{m}$ in depth, after 3500 traversals. Figure 5.16 shows a typical groove formed after 3500 traversals of the TiB_2 slider on Syndite. High magnification of the track confirms the extensive damage of the individual diamond particles within the structure as in Figure 5.17. The coefficient of friction decreased as the number of traversals increased.

A similar experiment was performed on Syndite, with an average diamond particle size of $2\mu\text{m}$, and the behaviour was comparable to that for the $25\mu\text{m}$ Syndite. Figure 5.18 shows a groove made in this material by TiB_2 after 3500

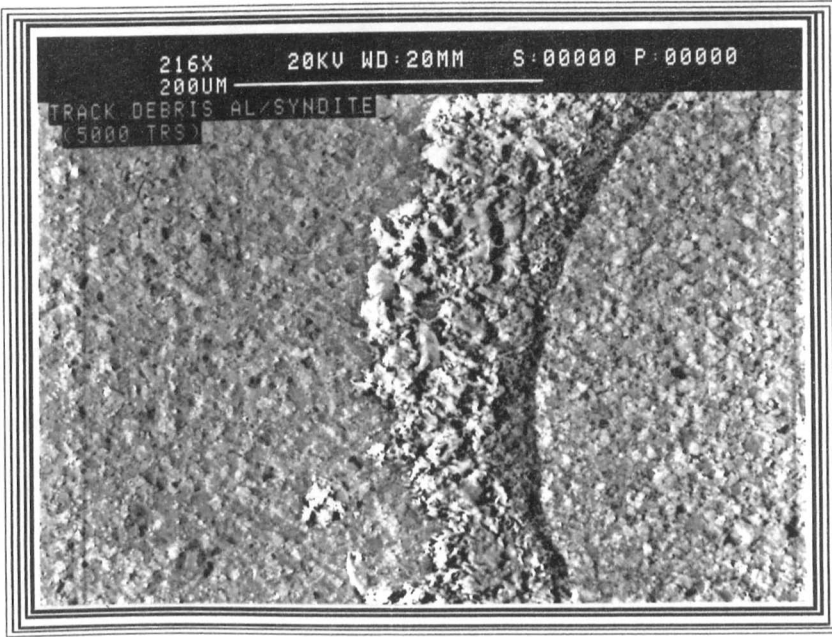


(a)

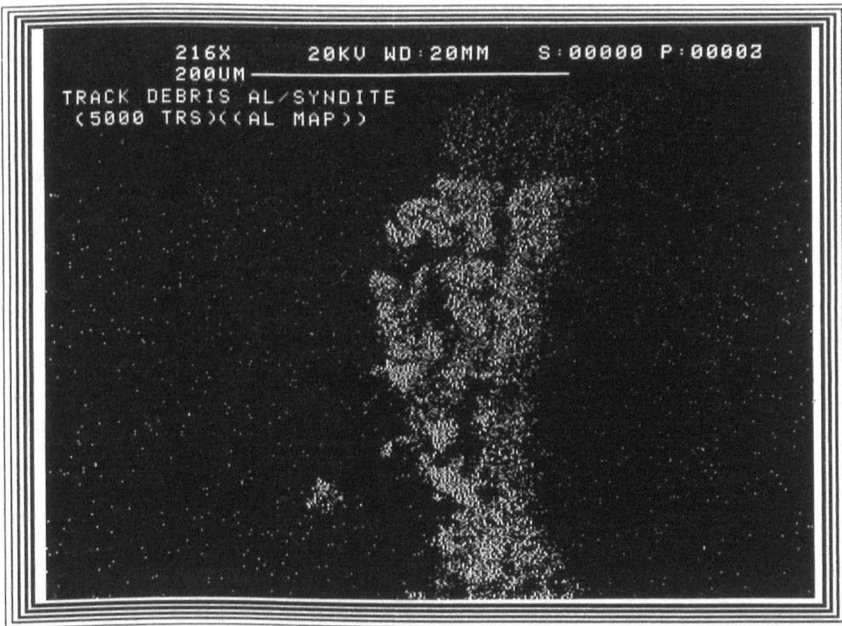


(b)

Figure 5.14 Dot maps of the layer formed on the tip of the aluminium slider on Syndite after 6500 traversals
(a) Oxygen
(b) Cobalt



(a)



(b)

Figure 5.15 (a) The accumulated track debris after 5000 traversals of an aluminium slider on Syndite
(b) Aluminium dot map of the debris

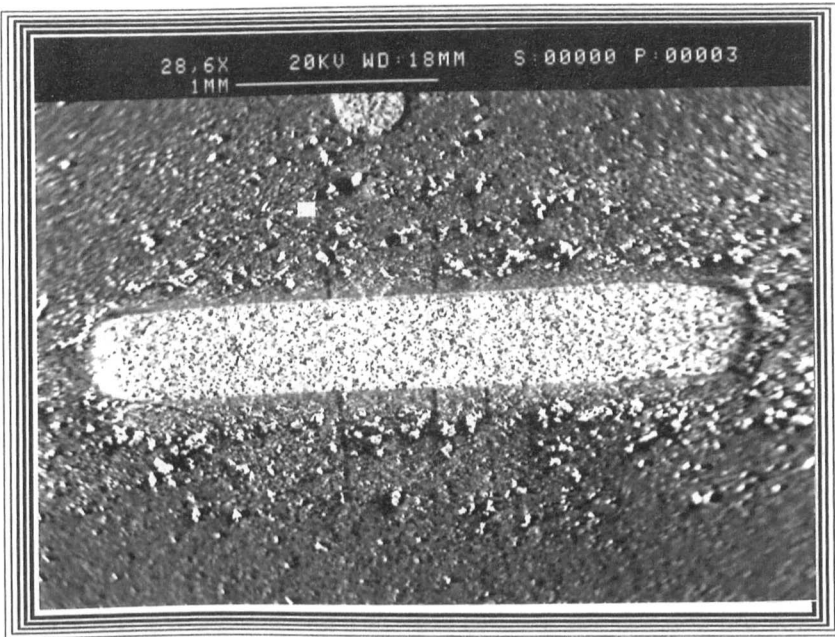


Figure 5.16 Wear groove developed by 3500 traversals of TiB₂ slider on Syndite with 25 μ m particle size

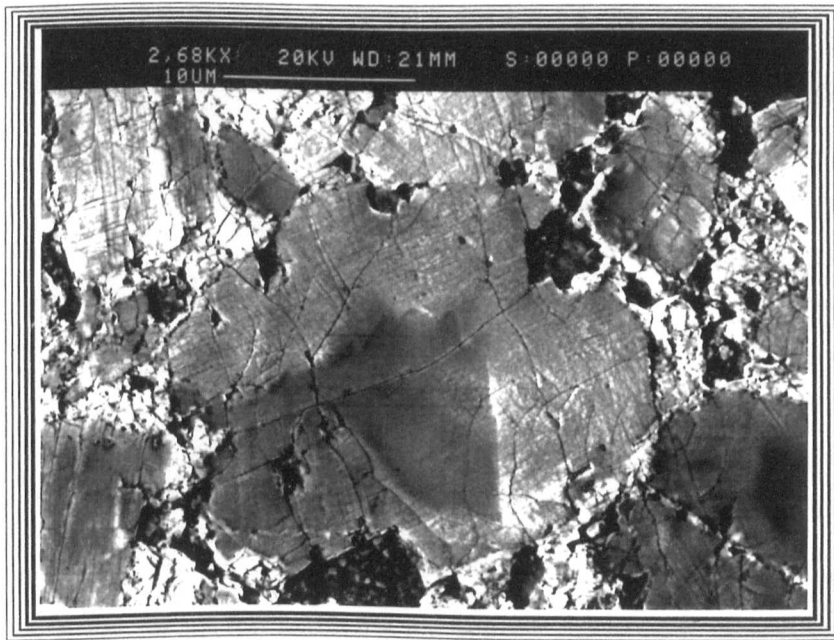


Figure 5.17 Showing the propagation of the cracks within the individual grains

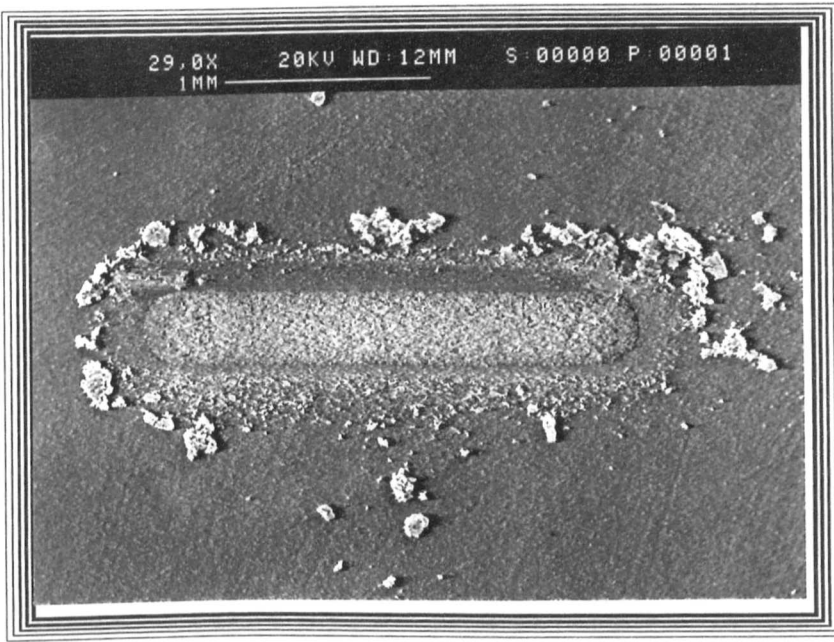


Figure 5.18 Wear groove developed by 3500 traversals of TiB₂ slider on Syndite with 2 μ m particle size

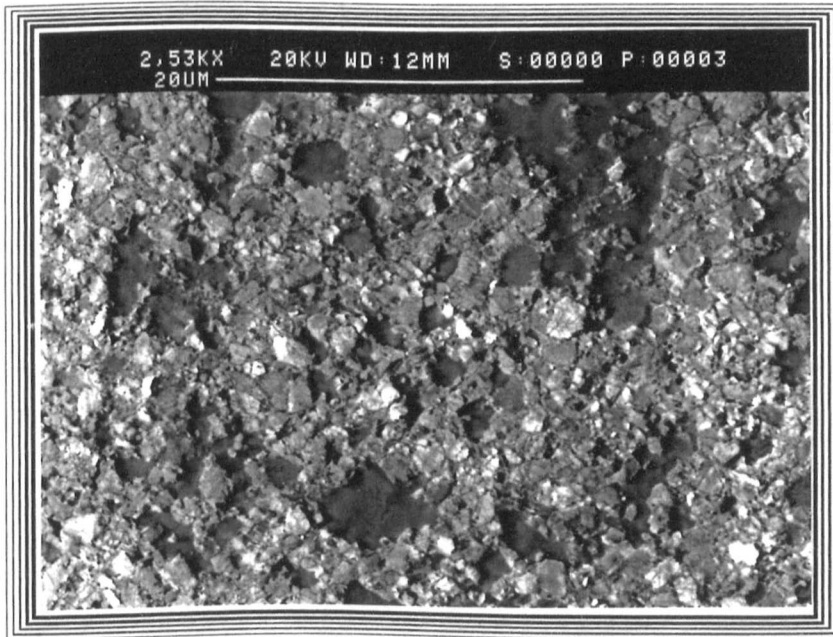
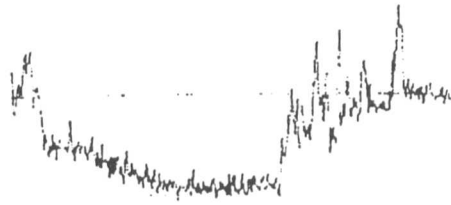


Figure 5.19 Intergranular cracking in Syndite after 3500 traversals with TiB₂ slider



(a) TiB_2 slider on Syndite



(b) TiB_2 slider on Syndax



(c) TiB_2 slider on CVDite



(d) Al slider on CVDite

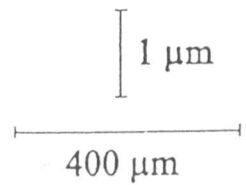


Figure 5.20 (a) - (d) Talysurf profiles of wear tracks after 3500 traversals on various polycrystalline diamond surfaces.

traversals and the transparticle nature of the cracks was again confirmed (Figure 5.19). The high friction developed using a cBN slider resulted in a wear groove 0.3 μm in depth after only 100 traversals. This groove was increased to 0.6 μm after 1000 traversals. A slight increase in the coefficient of friction was detected after the formation of the groove.

Typical Talysurf profiles of the grooves produced by smoothly blunted cone tips of titanium diboride in all the diamond specimens and that developed by the aluminium alloy slider on CVDite, are shown in Figure 5.20. It is notable that, after the same number of traversals on the same specimen of CVDite, the aluminium slider has developed a deeper groove than the titanium diboride slider.

5.5 Discussion

It is well established that changing the experimental atmosphere from air to vacuum increases the coefficient of friction of diamond sliding on diamond from $\mu=0.05$ to $\mu=0.5$ (Bowden and Young 1951). This finding has been confirmed by the results obtained for diamond in this work. For all soft sliders (metallic and ceramic) the coefficient of friction in air was less than that in a vacuum. Bowden and Hanwell (1966) reported that the absorption of gas molecules from air on the diamond surface reduced the coefficient of friction from $\mu=1$ to $\mu=0.1$. This suggests that the adsorbed films formed by reaction with the atmosphere act as a lubricant and that these films are removed, in vacuum, either by heating the diamond or by multiple passes on the same track.

The resultant low coefficient of friction for most of the metallic sliders used in air (Table 5.2 and Figure 5.2) are comparable with those previously obtained by Freeman and Field (1989). Table 5.2 shows that the frictional behaviour of diamond coating (CVDite) in air was similar to that of the natural diamond. However, in a vacuum, the coefficient of friction was much lower. In contrast with single crystal diamond, heating the CVDite surface in a vacuum (outgassing) has no major impact on its frictional behaviour. Taking the explanation given by Bowden and Hanwell (1966), the similarity in the frictional behaviour of CVDite in both air and vacuum might be assumed to be due to the high stability of the chemisorbed gases on its surface and this unusual characteristic may be due to the growth conditions.

Since there was no transfer of material to the diamond coating in CVDite, all metallic sliders showed low and relatively similar coefficients of friction - with the exception of the titanium alloy sliders. The coefficient of friction for this alloy was remarkably increased for all the diamond surfaces in a vacuum. This phenomenon was first reported by Buckley (1972) when he observed the coefficient of friction of titanium was the highest among the metallic sliders on Al_2O_3 . The large scale transfer of titanium to the diamond was also reported by Miyoshi and Buckley (1980) during their study of the friction of diamond sliding on a series of transition metals. This characteristic of titanium alloys could be related to the fact that titanium is a very strong carbide forming element i.e. it has a very strong affinity for carbon. This high chemical affinity resulted in high adhesive forces developing with a very strong interface where shear failure within the slider resulted in large-scale transfer of metal to the diamond surfaces.

Again, the coefficient of friction between metallic and ceramic sliders and polycrystalline diamond (Syndite and Syndax) was studied. Aluminium and mild steel sliders against Syndite resulted in a remarkably low coefficient of friction. However, strong adhesion occurred between the titanium alloy and Syndite surfaces resulting in a high coefficient of friction. Unlike CVDite, the coefficient of friction on Syndite almost doubled in vacuum compared with that in air. This difference between the two polycrystalline diamonds (CVDite and Syndite) may be related to their methods of production. To explain this difference further investigation is required, however, it could be that hydrogen, which plays an important role in the growth of diamond coatings, may be responsible for the stability of the chemisorbed surfaces on the coating.

Polycrystalline diamond (Syndax) and cubic boron nitride (Amorite) have shown similar behaviour with metallic sliders. As shown in Figure 5.4, large-scale transfer of metal to the hard surfaces has resulted in a high coefficient of friction. Effectively, this transferred metal protected the hard solid from the effects of cumulative frictional deformation.

The coefficient of friction for titanium diboride sliding on the diamond specimens was higher than that for the metallic sliders. These results are typical of those for a range of other ceramic sliders, including diamond on diamond (Xing 1996).

Unlike Syndax and cBN, the non-adhesion of aluminium and mild steel sliders on the diamond film in CVDite has exposed it to cumulative frictional deformation and wear. Surprisingly, increasing the number of traversals has resulted in significant wear of the diamond coating of CVDite by softer metallic sliders (aluminium and mild steel). Although the frictional forces generated by those

sliders were quite low, fracture and disintegration of the diamond coating was observed. This could be due to the high level of residual stresses in the diamond layer (with thickness greater than $\approx 12\mu\text{m}$). As mentioned in Chapter 1, Sato and Kamo (1992) related the peak shift of the Raman effect, observed with the polycrystalline coatings, to the internal stresses. These stresses resulted from the difference in the thermal expansion coefficients of the coatings and their substrates. In other words, during the cooling process of the deposited coating the mis-match between the substrate and the diamond coating, due to the difference in thermal contraction, resulted in significant residual stresses. Burton *et al* (1995) reported a tensile strain of 0.3% on the surface of the diamond coating and hence the tensile stress on the upper side of the coating will be equivalent to about 3.0 GPa. This value is comparable to the theoretical cleavage strength of diamond reported by Field (1992) (i.e. ≈ 3.0 GPa). Any addition to this tensile stress, due to the sliding friction, might result in spontaneous cleavage of individual diamond crystals. The resultant wear debris then becoming embedded in the metallic slider leads to increased rates of wear.

Another reason for the deformation of CVDite by softer sliders could be the tensile stresses generated by repeated sliding. Since the texture of the film in CVDite is columnar and the strength between grain boundaries may be low, the tensile stresses generated by the slider could initiate cracks in the grain boundaries. As the number of traversals increased, the crack system would have increased and the intersection of the transparticle cracks of the film result in fragmentation of the diamond particles to give highly abrasive wear debris. Figure 5.6 and 5.7 show detail of the wear track produced by different sliders.

SEM analysis confirmed that there were diamond particles embedded in the tip of the metallic sliders and the scratch lines in the wear track in Figure 5.7 are consistent with this suggestion. The embedded diamond particles in the tip of the slider may then account for the increase in the coefficient of friction of metallic sliders and the increased degree of wear.

As shown in Table 5.5, the formation of a groove by the titanium diboride slider was observed after only 100 traversals, rather than the 1000 required by metallic sliders. However, the overall wear depth after 3500 traversals was shallower and the coefficient of friction decreased with increasing number of traversals. These observations suggest that the wear mechanism developed by the titanium diboride slider was different from that for the metallic sliders. Indeed, the high apparent mean pressure of 13 GPa, combined with the frictional forces associated with a coefficient of friction of 0.45 was sufficient to initiate cracks and deform the diamond coating. The shallower track, compared with the cases of aluminium and mild steel sliders, could be related to the fact that it is unlikely that diamond particles became embedded in the slider's tip because of the lack of ductility of titanium diboride.

In the case of Syndax, metallic sliders did not deform the hard surface due to the large scale transfer of metal. However, deformation and wear was caused by the ceramic sliders (titanium diboride and cubic boron nitride). After 100 traversals the deformation of the hard surface by the titanium diboride was observed as a track with no depth. This track developed into a groove, of 0.3 μ m depth, after about 1000 traversals. The combination of high coefficient of friction and the relatively high mean pressure of 13GPa has initiated cracks within the diamond

particles. These cracks developed and intersected with repeated traversals. Figure 5.3b shows the propagation of the cracks through the individual grains and some of the grains fractured into small fragments. Once these fragments were detached, and pushed outside the track by the titanium sliders (Figure 5.8a), groove formation continued. This groove was then increased to $0.5\mu\text{m}$ after 3500 traversals. Using titanium diboride sliders, the coefficient of friction decreased because there was no adhesion i.e. the titanium diboride debris was pushed outside the track and did not accumulate on the slider.

The high frictional force and apparent mean contact pressure gave rise to a completely different wear mechanism when cubic boron nitride sliders are used on Syndax. The pluck-out of diamond particles was observed after 1000 traversals (Figure 5.10), and the removal of the diamond particles created a crater. This crater then served as a trap for the cubic boron nitride debris. Further sliding traversals increased the amount of debris, which accumulated in the open craters, leading to a strong self adhesion of the cubic boron nitride slider with the cBN debris in the crater. The sharp increase in the coefficient of friction associated with the strong adhesion, led to the fracture of the sliders after 1000 traversals.

In the event of significant transfer of material, increasing the number of traversals of metallic sliders to 3500 (and more) on Syndite resulted in a superficial polishing of the harder surface - i.e. no wear was observed. This could be related to the fact that the coefficient of friction generated between the metallic sliders and Syndite surface was low (lower than that of CVDite) and hence the associated tensile stresses were low. In addition to this, the Syndite compact tool

was apparently relatively free of residual stresses and hence the required frictional forces to fracture the hard surface had to be higher. However, the residual stresses cannot be ruled out from the entire system (substrate and diamond layer) of Syndite. There is a basic difference between CVD coating and Syndite - the latter is brazed on to its substrate with a much thicker interface layer having been made by sintering techniques. These intermediate materials between the diamond and its substrate will accommodate any internal stresses resulting from the brazing processes.

Multiple traversals of the aluminium slider on the Syndite specimen has resulted in an accumulation of a layer of wear debris on the tip of the sliders as shown in Figure 5.12. Analysis of this layer in the scanning electron microscope, confirmed that oxygen (see Figure 5.14a) was present in the brighter regions shown in this micrograph. Some of this material was also found on the surface of the diamond specimen but there was no evidence of the formation of a groove, even after 6500 traversals. This debris was detected only with aluminium sliders after 3500 traversals and its formation was considered to be the reason for the increase in the coefficient of friction to 0.06. Increasing the number of traversals after 3500 had no effect on the coefficient of friction. In the case of the mild steel slider, because no debris was formed, the friction decreased with increased number of traversals.

Although the initial coefficient of friction of titanium diboride on Syndite was lower than that on Syndax, the dominant wear mechanisms were similar. Crack propagation and intersection through individual particles, or grains, of the hard diamond phase (Figure 5.18) dominated the deformation process. In the case of

Syndite with 2 μ m particle size, some of the particles were completely fragmented and pushed outside the track leaving craters in the track.

The random orientation of the diamond particles in both Syndite and Syndax resulted in a different crack mechanism compared with CVDite. In Syndite and Syndax the crack propagation occurred within individual particles and fragmentation resulted from the intersection of the transparticle crack network. It is interesting to compare and contrast the propagation of cracks in these two polycrystalline diamond materials with that in CVDite. In the former case, the cracks are contained within the particles- i.e. they do not continue through the adjoining matrix phase. This effect leads to an increase in the toughness of such materials. In the later case, the crack is not deflected or stopped by the boundary between adjacent growth sectors or crystallites.

Cubic boron nitride sliders on Syndite produced a groove, with 0.6 μ m depth, after 1000 traversals. The wear mechanism was similar to that caused by the titanium diboride slider i.e. fragmentation of individual particles. Unlike cubic boron nitride on Syndax, 'pluck-out' of diamond particles was not observed. This is due to the higher strength of the diamond particles in Syndite resulting from secondary intergrowth between them; whereas this type of intergrowth does not occur between diamond particles in Syndax (Walmsley and Lang 1988). Finally, the Talysurf measurements of the wear track on CVDite, Syndite and Syndax did not show any sort of 'pile-up' adjacent to the sides of the grooves. Thus it may be concluded that there is no significant plastic deformation associated with the wear process under these conditions.

5.6 Conclusions

As a result of this investigation into the room temperature friction and wear of diamond materials by softer metallic and ceramic sliders, the following conclusions can be made:

1. In general, the coefficient of friction of metallic sliders on diamond materials in air was lower than that of ceramic sliders. The exception was the titanium alloy where large-scale transfer and adhesion of the titanium alloy to the diamond surface occurred.
2. The coefficient of friction of metallic sliders increased in vacuum significantly for all the diamond surfaces, with the notable exception of CVDite, and cBN.
3. Multiple traversals of aluminium and mild steel sliders resulted in cumulative deformation and wear of the diamond coating on CVDite. This deformation occurred under low mean pressures (less than 1 GPa) and coefficients of friction ($\mu=0.15-0.3$)
4. The cumulative deformation and wear of CVDite by softer metallic sliders was due to the high level of residual stresses in the coating and the abrasive nature of the embedded diamond wear debris on the tip of the sliders.

5. Unlike CVDite, and although there was no material transfer, aluminium and mild steel sliders were unable to wear Syndite where an interfacial layer was formed on the tip of the aluminium slider. On Syndax and cBN it was observed that metallic transfer to the flat surface occurred, pre-empting the possibility of cumulative deformation of the hard material with repeated traversals.
6. The wear mechanism developed by ceramic sliders on polycrystalline diamond was due to the initiation and intersection of cracks leading to fragmentation of the individual diamond particles.
7. In Syndax and Syndite, the cracks were contained within the particles- i.e. they did not continue through the adjoining matrix phase. This effect increases the toughness of such materials. However, in CVDite the cracks were not deflected or stopped by the boundary between adjacent growth sections or crystallites.
8. Unlike cubic boron nitride on Syndax, 'pluck-out' of diamond particles was not observed in Syndite. This is due to the higher strength of the diamond particles in Syndite resulting from secondary intergrowth between them; whereas this type of intergrowth does not occur between diamond particles in Syndax.

9. Crack initiation and propagation predominantly controlled the wear mechanisms, where observed, in these ultra-hard materials. There was no evidence to indicate that plastic deformation had a significant role.

Chapter 6 Summary, conclusions and suggestions for further research

6.1 Summary

The main theme of this research work has been the mechanical wear and deformation of ultra-hard materials by softer solids - i.e. as in the wear of cutting tools during shaping and machining of metal workpieces. Thus the main objective was to see how the soft impressor/slider technique might be extended to measure the flow stress; creep; friction and wear properties of the ultra-hard polycrystalline materials. As a result of this investigation the following conclusions could be drawn:

6.1.1 Flow stress

The soft impressor technique has been extended and used to study the effect of temperature on the flow stress of polycrystalline diamond (Syndax) and cubic boron nitride (Amborite). The findings are summarised as follow:

- ◆ A model based on Love's work for measuring the maximum shear strength of polycrystalline materials has been developed, and verified with data obtained from tensile measurements on polycrystalline copper.
- ◆ The results identify the brittle to ductile transition temperature between 700°C and 800°C for both materials. This transition followed a manner similar to that reported for diamond single crystals (Brookes 1992).

- ◆ Flow stresses for polycrystalline diamond (Syndax) are greater than those of Ib synthetic diamond in the temperature range 800°-133°C indicating the strengthening effect of the grain boundaries and the continuous β -SiC boundary phase. Also, the increased strength could be attributed to strain introduced during the sintering process of Syndax.
- ◆ The flow stresses for Amborite are lower than those of Syndax, reflecting microstructural differences between these two materials - i.e. in the former case, each cBN particle is covered by a “skin” of AlN and there is a continuous matrix phase of AlB₂. In contrast, Syndax consist of a continuous matrix phase (β -SiC) but this is reinforced by the continuos diamond network.

6.1.2 Impression creep

The soft impressor technique was used to examine the effect of extending the dwell time of the impressor on both Syndax and Amborite, over the temperatures range 800-1450°C. The following conclusions have been drawn:

- ◆ The impression volume for Syndax and Amborite has increased with increase in dwell time. This increase has enhanced the possibility of using the soft impression technique as an alternative to conventional testing methods (standard uniaxial techniques) in investigating the high temperature properties of advanced ceramic materials.
- ◆ In both materials, the overall creep (volume change) appears to be accommodated by the matrix materials(the second phase) rather than the hard particles. The same experimental technique was applied to Syndite, which has a different microstructure (complete intergrowth between particles) at

temperatures between 700°-900°C, resulting in no material displacement (volume change). This suggests that the contribution of the hard particles, diamond and cBN to the overall creep is minimal. However, plastic deformation within the hard particles under the impressor cannot be ruled out since the applied mean pressure is comparable to that of the sintering process.

6.1.3 Frictional deformation

As a result of this investigation into the room temperature friction and wear of diamond materials and cBN by softer metallic and ceramic sliders, the following conclusions can be drawn:

- ◆ The coefficient of friction of metallic sliders sliding in air on diamond materials was lower than that of ceramic sliders. The exception was titanium alloy and this was due to the large-scale transfer of the titanium alloy to the diamond surface. In vacuum, the coefficient of friction of metallic sliders increased significantly for all the diamond surfaces and cBN, except CVDite (coated diamond).
- ◆ Multiple traversals of aluminium and mild steel sliders resulted in deformation and wear of the diamond film of CVDite. This deformation occurred under low mean pressure (less than 1 GPa) and coefficient of friction ($\mu=0.15-0.3$). The abrasive nature of the embedded diamond debris on the tip of the sliders was considered to be responsible for the relatively high wear rate.
- ◆ Although there was no material transfer, aluminium and mild steel slider did not deform Syndite. On Syndax and cBN it was observed that metallic

transfer occurred, pre-empting the possibility of cumulative deformation of the hard surface with repeated individual traversals.

- ◆ The wear mechanism developed by ceramic sliders on polycrystalline diamond was due to the initiation and intersection of cracks, leading to the fragmentation of the diamond particles.
- ◆ The secondary interparticular growth of Syndite increased the strength of the diamond composite and prevented pluck-out of diamond particles.

6.2 Suggestions for further research

Towards a better understanding of the mechanical properties and the applications of polycrystalline diamond and cubic boron nitride, further research might include:

- ◆ Further investigations in order to understand the creep mechanisms operating at the critical temperature regime between 800°C and 1400°C. Ultimately, this might require Transition Electron Microscopy in order to resolve details of dislocation behaviour.
- ◆ Extending the research to study the friction and wear of polycrystalline diamond and polycrystalline cubic boron nitride from room temperature up to and just beyond the BDT temperature could improve our understanding of the mechanism of wear taking place during the metal cutting operation

- ◆ It is well established that Syndite has better performance in resisting plastic deformation than Syndax. However, this superiority is hindered by its instability at relatively low temperature. On the other hand, Syndax outperforms Syndite because of its thermal stability up to 1400°C. In the light of information obtained in this project, a comparison of their metal cutting performance may enhance better understanding of this application of polycrystalline diamond.

REFERENCES

- Agrawala, B.K., Singh, B.P. and Singhal, S.K.; (1986) *Mater. Sci.*, **21**, 1765-1768.
- Anthony, T.R., Banholzer, W.F., and Fleischer, J.F.; (1990) *Physical Review B*, **42**, 1104-1111.
- Atkins, A.G., Silverio, A. and Tabor, D., (1966) *J. Inst. Metals*, **94**, 369-378.
- Bex, P.A. and Shafto, A.R. (Ultra-hard Materials Application Technology), Vol. 3, ed. Daniel, P. (1984) 22-33 (Ascot, DeBeers Industrial Diamond Division).
- Bex, P.A. and Wilson, W.I.; (1977) *Industrial Diamond Review*, **37**, 10-17.
- Bowden, F.P. and Hanwell, A.E.; (1966) (The Friction of Clean Crystal Surfaces) *Proc. Roy. Soc.* A295, 233-243.
- Bowden, F.P. and Tabor, D.; (1964) 'Friction and Lubrication of Solids', Part II, Clarendon Press, Oxford.
- Bowden, F.P. and Tabor, D.; (1965) (Physical Properties of Diamond) Clarendon Press, Oxford.
- Bowden, F.P. and Young, J.E.; (1951) *Proc. Roy. Soc. London*, **A295**, 233-243
- Britun, B.F. and Pilyankevich; A.N.; (1989) *Poroshkovaya Metallurgiya*, **10**, 40-43.
- Brookes, C.A. Brookes, E.J. and Howes, V.R, (1990) (Science and Technology of New Diamond), eds. Saito, S., Fukunaga, O. and Yoshikawa, M, pp. 261-272, KTK Scientific Publishers.
- Brookes, C.A. Brookes, E.J. and Xing, G, (1991) *Proc. Mechanics of Creep-Brittle Materials*, Leicester.
- Brookes, C.A. Brookes, E.J. Howes, V.R. Roberts, S.G. and Waddington, C.P; (1990) *J. Hard Mater.*, **1**, 1, 3-24.
- Brookes, C.A. Shaw, M.P. and Tanner, P.E.; (1987) *Proc. Roy. Soc. London*, **A409**, 73-88.

- Brookes, C.A., (1970) *Nature*, **228**, 660-661.
- Brookes, C.A., (1986) *Proceedings of the International Conference on the Science of Hard Materials*, pp. 207-220, eds. Almond, E.A., Brookes, C.A. and Warren, R., Rhodes, Adam Hilger Ltd, Bristol and Boston.
- Brookes, C.A., and Brookes, E.J.; (1991) *Diamond Relat. Mater.*, **1**, 13-17.
- Brookes, C.A., and Green, P., (1973) *Nature*, **246** (115), 119-221.
- Brookes, C.A., and Lambert, W.A. (*Ultra-hard Materials Application Technology*), Vol. 1, ed. Daniel, P. (1982) 128-136 (Ascot, DeBeers Industrial Diamond Division).
- Brookes, C.A., O'Neil J.B. and Redfern, B.A., (1971) *Proc. Roy. Soc. London.*, **A322**, 73-88.
- Brookes, E.J.; (1992) Ph.D. Thesis, Hull University.
- Buckley D H; (1972) *Ceramic Bulletin*, Vol. **51**, No. 12, 884-891.
- Bundy, F.P. and Wentorf, R.H., Jr.; (1963) *J. Chem. Phys.*, **38**, 1144-1149.
- Burton, N.C., Butler, J.E., Lang, A.R. and Steeds, J. W. (1995) *Proc. R. Soc. Lond. A* (**449**), 555-566.
- Casey, M. and Wilks, J.;(1973) *J. Phys. D. Appl Phys.* **6**, 1772-1781.
- Chadwick, M.M., Jupp, R. and Wilkinson, D., (1993) *J. Amer. Ceram. Soc.*, **76**, 376-387.
- Chokshi, A., (1990) *J. Mater. Sci.*, **25**, 3221-3233.
- Courtney, T.H., (1990) 'Mechanical Behaviour of Materials' McGraw Hill, Singapore.
- De Vries, R.C., Wentorf, R.H., Jr. and Bundy, F.P.; (1980) *Science*, **208**, 873-880.
- De Vries, R.C.; (1972) G.E.C. Report No. 72CRD178, Schenectady, New York.
- Deryagin, B.V., Spitsyn, B.V., Builov, L.L., Klochkov, A.A., Gorodetski, A.E., and Smolyaninov, A.V.; (1976), *Dokl. Akad. Nauk SSSR*, 231, 333.
- Eisenstadt, M.M., (1971) 'Mechanical Properties of Materials' Macmillan Company, New York.
- Enomoto, Y. and Tabor, D. (1981). *Proc. R. Soc. London* **A373**, 405-417.

- Evans, R. and Wilshire, B., (1993) 'Introduction to Creep', The Institute of Materials, England.
- Evans, T., and Wild, R.K.; (1965) *Phil. Mag.*, **12**, 479-486.
- Feng, Z. and Field, J.E.; (1991) *J. Surf. Coating Technol.* **47**, 631-645.
- Feng, Z. and Hayward, I. (1988) In *Ultrahard Materials Application Technology*, Vol. 4, (ed. Barrett, C.), De Beers Industrial Diamond Division, London, pp. 36-46.
- Field, J.E. (1983) *Diamond: Properties and Definitions*, Cavendish Laboratory, Cambridge.
- Field, J.E. (1992), *The Properties of Natural and Synthetic Diamond*, edited by J.E. Field Academic Press LTD, London.
- Field, J.E. and Freeman.; (1981) *Phil. Mag.*, **A43**, 595-618.
- Freeman, C.J. and Field, J.E. (1989) *J. Mat. Sci.*, **24**, 1069-1072.
- Frost, H. J. and Ashby, M.F. (1982) 'Deformation Mechanism Maps', Pergman Press, Oxford.
- Gigl, P.D. (1979) In *High Pressure Science and Technology*, Vol. 1 (eds. Timmerhaus, K.D. and Barber, M.S.), Plenum, New York, pp.914-922.
- Grillo,S; (1996) Ph.D. Thesis, Cambridge University.
- Groves, C.W. and Kelly, A., (1963) *Proc. Roy. Soc., London* **A275**, 233-244.
- Guillou, M.O., Henshall, J.L. and Hooper, R.M.; (1990) *J. Hard Mater.*, Vol. **1**, 4, 289-296.
- Hall, H. T. (1961) In *Proceeding of an International Symposium on High Temperature Technology*, McGraw-Hill, New York, pp. 145-156.
- Hall, H.T.; (1960) *Rev. Sci. Inst.*, **31**, 125-131.
- Hall, H.T.; (1970) *Science*, **169**, 868-869.
- Hargreaves, F., (1928) *J. Inst. of Metals*, **39**, 301.
- Heath, P.J.; (1986) *Industrial Diamond Review*, **3**, 120-127.
- Hertz, H. (1981), (On the Contact of Elastic Solids), *Miscellaneous Papers*, Vol. **1**, 146 Jones D.E. and Schott, G.H (trans), Macmillan and Co. Ltd., London.
- Hibbs, L.E. and Wentorf, R.H., Jr.; (1974) *High Temperature-High Pressure*, **6**, 409-413.

- Hill, R., (1950) 'The Mathematical Theory of Plasticity', Clarendon Press, Oxford.
- Hirsch, P.B., Pirouz, P., Roberts, S.G. and Warren, P.D., (1985) *Phil. Mag. B*, **52** (3), 759-770.
- Hooper, R.M. Guillou, M.O. and Henshall, J.I.; (1991) *J. Hard Mater.*, Vol. **2**, 3- 4, 223-231.
- Hooper, R.M. Shakib, J.I. and Brookes, C.A. (1988) *Materials Science and Engineering*, **A105/106**, 429-433.
- Howes, V. R. and Tolansky, S. (1955), *Proc. Soc. London.*, **A 230**. 287-293, *ibid.* 294-300.
- Johnson, K.L., (1970) *J. Mech. Phys. Solids*, **18**, 115.
- Jou, Z.C. and Virkar, A.V., (1990) *J. Amer. Ceram. Soc.*, **73**, 1928.
- Kamo, M., Sato, Y., Matsumoto, S. and Setaka, N.; (1983). *Cryst. Growth* **62**, 642-644.
- Katzman, H. and Libby, W.F.; (1971) *Science*, **172**, 1132-1133.
- Kitahama, K., Hirata, K., Nakamatsu, H., Kawai, S., Fujumori, N., Imai, T., Yoshino, H., and Doi, A. (1986), *Appl. Phys. Lett.* **49**, 634-646.
- Konig, W. and Neises, A. (1993) *Wear*, **12**, 162-164.
- Kossowsky, R., Miller, D. and Diaz, S. (1975) *J. Mater. Sci.*, **10**, 983-996.
- Lammer, A.; (1988) *Mater. Sci. and Tech.*, **4**, 949-955.
- Laurence, V., Demazeau, G and Etourneau, J.; (1991) *Mater. Sci. Eng.*, **B10**, 149-164.
- Lee, M., DeVries, R.C. and Koch, E., *Proceedings of the International Conference on the Science of Hard Materials*, (1984), pp. 221-232, eds. Almond, E.A., Brookes, C.A. and Warren, R., Rhodes, Adam Hilger Ltd, Bristol and Boston.
- Lee, M., DeVries, R.C. and Koch, E.F.; (1984) G.E.C. Report No. 84CRD241.
- Li, W.B., Henshall, J.L., Hooper, R.M. and Easterling, K.E., (1991) *Acta Metall. Mater.*, **39** (21), 3099-3110.
- Love, A.E.H., (929) *Proc. Roy. Soc. (London)*, **A228**, 377.
- Marsh, D.M., (1964) *Proc. Roy. Soc.*, **A279**, 420.

- Masson, I. and Feiereisen, J.P., (1992) *Br. Ceram. Trans. J.*, **91**, 177-189.
- Matsumoto, S. (1985), *Mater. Sci. Lett.* **4**, 600.
- Matsumoto, S., Sato, Y., Kamo, M., and Setaka, N. (1982), *Mater. Sci.* **17**, 3106-3120.
- Maugis, D., (1980) *Wear*, **62**, 349-269.
- Mehan, R.L. and Hayden, S.C. (1981) *Wear*, **47**, 195-212.
- Miyoshi, K. and Buckley, D.H.; (1980) *Appl. Surf. Sci.*, **6**, 161-172.
- Miyoshi, K., Wu, R. and Jackson, H., (1993) *J. Appl. Phys.* **74** (7), 4446-4454.
- Morgan, J.E., (1976) Ph.D Thesis, University of Exeter.
- Mott, N., (1953) *Phil. Mag.* **44**, 742.
- Mulhearn, T.O. and Tabor, D., (1960) *J. Inst. Met.*, **89**, 7.
- Okada, K. and Namba (1989) *J. Vac. Sci and Tech.*, **A7** (2), 132.
- Parry, A. (1992) Ph.D. Thesis, University of Exeter.
- Ponton, C.B. and Rawlings, R.D., (1989) *Mat. Sci. Tech.*, **5**, 961.
- Pullum, O.J., and Lewis, M.H.; (1990) *Mater. Lett.*, **9**, 83-86.
- Roberts, D.C.; (1979) *Ind. Diamond Rev.*, **39**, 237-241.
- Roberts, S.G., Warren, P.D. and Hirsch, P.B., (1986) *J. Mats. Res.*, **1**, 162-178.
- Roberts, S.G., Warren, P.D. and Hirsch, P.B., (1988) *Mat. Sci. Eng.*, **A105/106**, 19.
- Roebuck, B. and Almond, E.A., (1982) *J. Mat. Sci. Lett.*, **1**, 519.
- Ruano, O.A. and Sherby, O.D., (1994) *Proceeding of an International Engineering Foundation Conference on the Plastic Deformation of Ceramics (Utah, USA)*, eds. Bradt, R. and Brookes, A.C. and Routbort, J., Plenum Press, New York.
- Rudder, R. A., Posthill, J.B., Hudson, G.C., Malta, D.P., Thomas, R.E., Markunas, R.J., Humphreys, T.P., and Nemanich, R.J. (1992), in *Wide Band Gap Semiconductors*, edited by T. D. Moustakas, J.I. Pankove, and T. Hamakawa. *Materials Research Society Proceedings*, Vol. **242**, pp. 23-30.
- Saito, Y., Matsuda, S., and Nogita, S. (1986), *Mater. Sci. Lett.* **5**, 565.

- Samuels, L. E. and Mulhearn, T. O., (1956). *Journal of the Mechanics and Physics of Solids*, **5**, 125-134.
- Santhanam, K., Sadu, Y. and Fuji, S., (1986) *J. Mat. Sci. Letters* **6**, 900-903.
- Sargent, P.M. and Ashby, M.F., (1989) *CUED/ C Mats./ TR.145*.
- Sato, Y., and Kamo, M., (1992), in *The Properties of Natural and Synthetic Diamond*, edited by J.E. Field. Academic Press LTD, London.
- Sawabe, A., and Inzuka, T. (1985), *Appl. Phys. Lett.* **46**, 146.
- Sawaoka, A. and Akashi, T.; (1984) *Mate. Res. Soc. Symp. Proc.*, Vol. **24**, Elsevier, New York, p. 365.
- Seal, M (1958). *Proc. R. Soc. London* **A248**, 379-393.
- Shaw, M.P. and Brookes, C.A., (1989) *J. Mater. Sci.*, **24**, 2727-2734.
- Spitsyn, B.V., Bouilov, L.L and Deryaguin, B.V.; (1981) *Cryst. Growth*, **52**, 219-226.
- Suzuki, H., Hayashi, K. and Taniguchi, Y. (1982) *Trans. JIM*, **23**, 77.
- Tabor, D.; (1951) (*The Hardness of Metals*), Clarion Press, Oxford.
- Tabor, D.; (1970) *Rev. Phys. Tech.*, **1**, 145.
- Tabor, D.; (1979) in '*The Properties of Diamond*', ed. Field, J.E., Academic Press, London.
- Takayema, H., Iijema, M. and Kashiwase, N., (1984) *J. Jpn. Soc. Prec. Eng.*, **50**, 1110-1116.
- Tolansky, S. (1955) (*The Microstructure of Diamond Surfaces*) NAG Press, London.
- Tolkowsky; (1920) PhD Thesis, University of London.
- Tomlinson, P.N. and Wedlake, R.J. (1983) proceeding of the international conference on recent development in hard materials (Pretoria), eds. Comins, N.R. and Clarks, J.B. (Pergamon, Oxford)p.173.
- Tomlinson, P.N. Pipkin, N.J. Lammer. A. and Burnand, R.P.; (1985) *Industrial Diamond Review*, **6**, 299-304.
- Trent, E.M.; *Metal Cutting*, Butterworths, London, 1977.
- Wakatsuki, M., Ichinose, K. and Aoki, T., (1972) *Mater. Res. Bull.*, **7**, 999.
- Walmsley, J.C. and Lang, A.R.; (1983) *Mater. Sci. Lett.* **2**, 785-788.

- Walmsley, J.C. and Lang, A.R.; (1987) *Mater. Sci.*, **22**, 4093-4102.
- Walmsley, J.C. and Lang, A.R.; (1988) *Mater. Sci.*, **23**, 1829-1834.
- Wang, J., (1994) *J. Mater. Sci.*, **29**, 6139-6141.
- Wentorf, R.H., Jr. and Rocco, W.A., (1973) U.S. Patent 3745623.
- Wentorf, R.H., Jr.; (1957) *J. Chem. Phys.*, **26**, 956.
- Wentorf, R.H., Jr.; (1961) *J. Chem. Phys.*, **34**, 809-812.
- Wentorf, R.H., Jr.; (1966) *Ber. Bunsenges. Fur Phys. Chem.*, **70**, 975.
- Wermark, G., Chatfield, C. and Dunlop, G.L., *Proceedings of the International Conference on the Science of Hard Materials*, (1984), pp. 207-220, eds. Almond, E.A., Brookes, C.A. and Warren, R., Rhodes, Adam Hilger Ltd, Bristol and Boston.
- Wiederhorn, S. and Long, G. (1994) *Proceedings of the Conference on the High temperature Properties of Si₃N₄ Ceramics (1994)*, eds. Hoffmann, M. and Petzow, G., Academic Publishers, Netherlands.
- Wild, R.K., Evans, T. and Lang, A.R.,;(1967) *Phil. Mag.*, **15**, 267.
- Wilkinson, D.S., (1994) *Proceeding of an International Engineering Foundation Conference on the Plastic Deformation of Ceramics (Utah, USA)*, eds. Bradt, R. and Brookes, A.C. and Routbort, J., Plenum Press, New York.
- Wilks, E.M. and Wilks, J.; (1972) *J. Phys. D. Appl. Phys.*, **6**, 1272-1281.
- Wilks, J. and Wilks, E.M. (1991) 'Properties and Applications of Diamond', Butterworth-Heinemann, U.K.
- Williams, W.S. (1964) *J. Appl. Phys.* **35**, 1329-1338.
- Wolfe, C.F. and Williams, W., *Proceedings of the International Conference on the Science of Hard Materials*, (1984), pp. 207-220, eds. Almond, E.A., Brookes, C.A. and Warren, R., Rhodes, Adam Hilger Ltd, Bristol and Boston.
- Wong, M.S., Meilunas, T. and Chang, R., (1989) *Mater. Res. Soc.* **140**, 483.
- Yazu, S., Nisikawa, T., Nakai, T. and Doi, Y. (1982) *Proceedings of the international conference on recent development in hard materials (Pretoria)*, eds. Comins, N.R. and Clarks, J.B. (Pergamon, Oxford)p.449-456.